



UNIVERSIDADE ESTADUAL DE
CAMPINAS

Instituto de Matemática, Estatística e
Computação Científica

SAMUEL FRANCISCO

**An Irregularity Measure Based on Wasserstein
Metric for Multivariate Mathematical
Morphology**

**Uma Medida de Irregularidade Baseada na
Métrica de Wasserstein para Morfologia
Matemática Multivariada**

Campinas

2023

Samuel Francisco

An Irregularity Measure Based on Wasserstein Metric for Multivariate Mathematical Morphology

Uma Medida de Irregularidade Baseada na Métrica de Wasserstein para Morfologia Matemática Multivariada

Tese apresentada ao Instituto de Matemática, Estatística e Computação Científica da Universidade Estadual de Campinas como parte dos requisitos exigidos para a obtenção do título de Doutor em Matemática Aplicada.

Thesis presented to the Institute of Mathematics, Statistics and Scientific Computing of the University of Campinas in partial fulfillment of the requirements for the degree of Doctor in Applied Mathematics.

Supervisor: Marcos Eduardo Ribeiro do Valle Mesquita

Este trabalho corresponde à versão final da Tese defendida pelo aluno Samuel Francisco e orientada pelo Prof. Dr. Marcos Eduardo Ribeiro do Valle Mesquita.

Campinas

2023

Ficha catalográfica
Universidade Estadual de Campinas
Biblioteca do Instituto de Matemática, Estatística e Computação Científica
Ana Regina Machado - CRB 8/5467

F847i Francisco, Samuel, 1986-
An irregularity measure based on Wasserstein metric for multivariate mathematical morphology / Samuel Francisco. – Campinas, SP : [s.n.], 2023.

Orientador: Marcos Eduardo Ribeiro do Valle Mesquita.
Tese (doutorado) – Universidade Estadual de Campinas, Instituto de Matemática, Estatística e Computação Científica.

1. Morfologia matemática multivariada. 2. Inteligência computacional. 3. Processamento de imagens. 4. Transporte ótimo. 5. Medidas de irregularidade (Matemática). I. Mesquita, Marcos Eduardo Ribeiro do Valle, 1979-. II. Universidade Estadual de Campinas. Instituto de Matemática, Estatística e Computação Científica. III. Título.

Informações Complementares

Título em outro idioma: Uma medida de irregularidade baseada na métrica de Wasserstein para morfologia matemática multivariada

Palavras-chave em inglês:

Multivariate mathematical morphology

Computational intelligence

Image processing

Optimal transportation

Irregularity measures (Mathematics)

Área de concentração: Matemática Aplicada

Títuloção: Doutor em Matemática Aplicada

Banca examinadora:

Marcos Eduardo Ribeiro do Valle Mesquita [Orientador]

Peter Sussner

João Batista Florindo

Franklin César Flores

Tsang Ing Ren

Data de defesa: 10-07-2023

Programa de Pós-Graduação: Matemática Aplicada

Identificação e informações acadêmicas do(a) aluno(a)

- ORCID do autor: <https://orcid.org/0000-0001-5236-2300>

- Currículo Lattes do autor: <http://lattes.cnpq.br/9017894022082983>

**Tese de Doutorado defendida em 10 de julho de 2023 e aprovada
pela banca examinadora composta pelos Profs. Drs.**

Prof(a). Dr(a). MARCOS EDUARDO RIBEIRO DO VALLE MESQUITA

Prof(a). Dr(a). PETER SUSSNER

Prof(a). Dr(a). JOÃO BATISTA FLORINDO

Prof(a). Dr(a). FRANKLIN CÉSAR FLORES

Prof(a). Dr(a). TSANG ING REN

A Ata da Defesa, assinada pelos membros da Comissão Examinadora, consta no SIGA/Sistema de Fluxo de Dissertação/Tese e na Secretaria de Pós-Graduação do Instituto de Matemática, Estatística e Computação Científica.

For Liam and Maitê, my children, my joy, my everything. This thesis is an infinitesimal tribute to the infinite love I have for you.

Acknowledgements

Thank you very much professor Marcos Eduardo Valle. My advisor, Marcos, was an excellent mentor. I can not express enough how much I learned from him. He has not only provided me with knowledge and guidance throughout my research, but also taught me how to think critically and independently. A researcher can only become truly great by learning from other great researchers, and Marcos was instrumental in helping me achieve that. He is a top-notch researcher. I am deeply grateful for his guidance and support and I hold him in the highest regard.

I am grateful for the invaluable insights and suggestions provided by professors Peter Sussner and João Batista Florindo, who have volunteered their time for my qualifying exam. Furthermore, I would like to extend my deepest appreciation to the esteemed members Peter Sussner, João Batista Florindo, Franklin César Flores, and Tsang Ing Ren of the thesis committee for their time and effort in evaluating my work. Their expertise and invaluable feedback have been essential in helping me improve and refine my research.

I want to thank the professors at IMECC, in particular, the professors Estevão, Joni, Marcia, Sandra, and Peter who gave me doctoral courses. Also, I would like to thank all my friends at IMECC. It was years of much study and companionship. In particular, I would like to thank my classmates Acacio (chapecó), Diego (the man), Eduardo (Dudu), Fabiano (matrix's magician), Gesivaldo (meniniu, the man who made the shift disappear), José Ivelton (Jackie Chan), Luiz (Luizão), Maycon (the priest), Ronaldo (the partner), Tacildo (the monster), Tiago (the purist), and Walter (vascaíno, eternal sufferer).

I would like to thank professors Rodney Carlos Bassanezi, Ana Carolina Boero, and Igor Leite Freire who had written letters of recommendation for admission to the doctoral program at IMECC. I also thank the Federal Institute of Education, Science and Technology of São Paulo (IFSP), the institution where I currently work, which provided me with the conditions to complete the course.

Thanks to Marco Aurélio Granero and Santiago Velasco-Forero, who together with me and my supervisor Marcos Valle, have developed a congress article that became a book chapter and an article in the Journal of Mathematical Imaging and Vision of Springer. I also thank my friends Amari Goulart, Carlos Eduardo Toffoli, Fidelis Zanetti de Castro, Ligia Corrêa de Souza, Roberto Seidi Imafuku, and William Vieira who were key people in starting the doctoral course and who always rooted for me.

Last but not least, I would like to thank my entire family, especially my mother Encarnação Francisco and my wife Caroline Francisco who have supported me through all the difficult times I have gone through over the years.

Resumo

A morfologia matemática é uma teoria não linear para análise e processamento de imagens baseada em conceitos topológicos e geométricos que pode ser desenvolvida utilizando a teoria de reticulados. A estrutura de reticulados completos é conveniente para estudos teóricos e práticos na morfologia matemática. A morfologia matemática é aplicada a imagens binárias, tons de cinza e imagens multivariadas. Imagens obtidas por operadores morfológicos em imagens coloridas em que o espaço de cores possui uma ordem parcial podem conter cores falsas. As imagens obtidas por operadores morfológicos em imagens coloridas em que o espaço de cores possui uma ordem total, não apresentam cores falsas. Entretanto, apresentam imperfeições que se assemelham a um serrilhado. Essas imperfeições nas imagens aparecem em operadores morfológicos multivariados baseados em uma ordem total e é chamada de irregularidade. Essa tese propõe construir uma medida de irregularidade para morfologia matemática multivariada. Para este propósito define-se o índice de irregularidade global utilizando-se a métrica de Wasserstein e a soma generalizada da distância entre duas imagens pixel a pixel. Além disso, define-se um índice de irregularidade local devido a impossibilidade computacional de medir a irregularidade para imagens multivariadas reais devido ao alto custo do problema de otimização para obtenção da métrica de Wasserstein. Prova-se que o índice de irregularidade local é um limitante inferior para o índice de irregularidade global e mostram-se resultados computacionais em imagens naturais. Utiliza-se também um método de entropia regularizada como forma de aproximação para a métrica de Wasserstein com o intuito de calcular o índice de irregularidade local com baixa complexidade computacional. Ainda, observações entre as medidas de irregularidade de acordo com o tamanho do elemento estruturante e das janelas locais que são utilizadas para o cálculo do índice de irregularidade local são realizadas. A partir desses resultados, é possível concluir que os índices de irregularidade global e local são medidas satisfatórias para irregularidades provenientes de operadores morfológicos multivariados. Por fim, utilizam-se abordagens morfológicas como a solução do problema do caixeiro viajante e os mapas auto-organizáveis de Kohonen para justificar a dificuldade de se obter uma ordem total que minimize a irregularidade.

Palavras-chave: Morfologia matemática multivariada, inteligência computacional, processamento de imagens, transporte ótimo, medidas de irregularidade (Matemática).

Abstract

Mathematical morphology is a nonlinear theory for analyzing and processing images based on topological and geometric concepts that can be developed using lattice theory. The complete lattice theory is suitable for theoretical and practical studies in mathematical morphology. Mathematical morphology is applied to binary, grayscale, and multivariate images. Images obtained by morphological operators in color images where the color space is endowed with a partial order may contain false colors. The images obtained by morphological operators in color images in which the color space is endowed with a total order do not present false colors. However, they present aliases that resemble jaggies. The aliasing on images appears in multivariate morphological operators based on a total order and is called irregularity. This thesis proposes to build an irregularity measure for multivariate mathematical morphology. For this purpose, the global irregularity index is defined using the Wasserstein metric and the generalized sum of pixel-wise distances of the two images. Furthermore, a local irregularity index was defined because of the computational impossibility of measuring the irregularity for natural multivariate images due to the high cost of the optimization problem to obtain the Wasserstein metric. We prove that the local irregularity index is a lower bound for the global irregularity index and show computational results with natural images. Also, the entropic regularized method is used as an approximation for the Wasserstein metric in order to calculate the local irregularity index with low computational complexity. Additionally, remarks between the irregularity measures according to the size of the structuring element and the local windows used to calculate the local irregularity index are given. From these results, it is possible to conclude that the global and local irregularity indices are satisfactory measures for irregularities from multivariate morphological operators. Finally, morphological approaches based on the solution of the traveling salesman problem and Kohonen's self-organizing maps are used to justify the hardness of obtaining a total order that minimizes the irregularity.

Keywords: Multivariate mathematical morphology, computational intelligence, image processing, optimal transportation, irregularity measures (Mathematics).

List of Figures

Figure 1.1 – Color image and the result of applying an opening operation.	17
Figure 2.1 – Illustrative example of a color image $\mathbf{I} : D \rightarrow \mathcal{C}_{RGB}$	28
Figure 2.2 – Illustrative example of images obtained by morphological operators. Figure a) shows the color image \mathbf{I} . Figure b) shows the dilated image using the h -lexicographical order and Figure c) shows the eroded image using the h -lexicographical order.	30
Figure 2.3 – Illustrative example of images obtained by h -ordering based on SVM. Figure a) shows the color image \mathbf{I} given in Figure 2.1. Figure b) shows the dilated image using (2.24) and Figure c) shows the eroded image using (2.24).	37
Figure 2.4 – Color palette used in the SVM approach.	37
Figure 2.5 – Illustrative example of images obtained by h -ordering based on the projection depth function. Figure a) shows the color image \mathbf{I} given in Figure 2.1. Figure b) shows the dilated image using (2.27) and Figure c) shows the eroded image using (2.27).	39
Figure 2.6 – Bicone for the m -HCL color space. Source: Burgeth & Kleefeld (2013).	41
Figure 2.7 – Illustrative example of morphological operators using the Loewner approach. Figure a) shows the color image \mathbf{I} given in figure 2.1. Figure b) shows the dilated image δ_S^W and Figure c) shows the eroded image ε_S^W	42
Figure 2.8 – Illustrative example of false colors. Figure a) shows image \mathbf{I}_1 , size 9×9 (81 pixels), with the colors blue, red and green. Figure b) shows the false color black on the dilated image $\delta_S^M(\mathbf{I}_1)$. Figure c) shows the false colors magenta and cyan on the eroded image $\varepsilon_S^M(\mathbf{I}_1)$. Figure d) shows the color image \mathbf{I} . Figure e) shows the dilated image $\delta_S^M(\mathbf{I})$, and Figure f) shows the eroded image $\varepsilon_S^M(\mathbf{I})$	44
Figure 2.9 – Figure a) shows image \mathbf{I} consisting of three colors: pure black, black and pure blue. Figure b) shows the dilated image \mathbf{J}_L using lexicographic order. Figure c) shows the dilated image \mathbf{J}_M using marginal order.	46
Figure 3.1 – Figure a) shows image \mathbf{I} with size 6×5 consisting of two colors: black and orange. Figure b) depicts the image \mathbf{J} , acquired through a permutation of color values in \mathbf{I} at positions $(2, 2)$ and $(4, 5)$	53
Figure 3.2 – Top: Global irregularity index calculated by the likelihood of substituting $\mathbf{u} = (0, 0, 0)$ with $\mathbf{w} = (0.005, 0, 0)$. Bottom: Images that have undergone dilation using values of π ranging from 0.0 to 1.0, incrementing by 0.25 each time, respectively.	55
Figure 3.3 – The global irregularity index Φ_1^g that were computed for small color images using dilation, erosion, opening, and closing operators.	56

Figure 3.4 – Presentation of the global irregularity index distribution of 100 small color images for 5 morphological approaches.	58
Figure 4.1 – Presentation of the local irregularity index distribution of 100 color images for 5 morphological approaches.	63
Figure 4.2 – Dilated image and local irregularity index using 5 approaches.	64
Figure 4.3 – Eroded image and local irregularity index using 5 approaches.	65
Figure 4.4 – Opened image and local irregularity index using 5 approaches.	66
Figure 4.5 – Closed image and local irregularity index using 5 approaches.	67
Figure 4.6 – Relation of local irregularity measure by the two methods.	70
Figure 4.7 – Plot of the local irregularity measure based on the structuring element size. The shaded area represents the first and third quartiles.	72
Figure 5.1 – Illustrative example of the dilated images obtained by the SPO and TSP orderings with a cross structuring element. In TSP 1, the Hamiltonian path of the optimal TSP solution is used. In TSP 2, the same path of TSP 1 is used with a translation to address the cyclic problem.	79
Figure 5.2 – Color spectra obtained of the TSO, TSP 1, and TSP 2 images.	79
Figure 5.3 – The Hamiltonian paths constructed on graph \mathcal{G} of the toy image.	79
Figure 5.4 – Image I_a and their morphological openings by stochastic permutation ordering, TSP ordering, and lexicographical ordering, respectively.	80
Figure 5.5 – Distribution of the input data obtained by the I_a , and the respective Hamiltonian paths based on the SPO, TSP, and lexicographic orderings.	81
Figure 5.6 – Neural network diagram.	83
Figure 5.7 – Image I_a and the opening J_a^{SOM}	86
Figure 5.8 – Distribution of the input data obtained by I_a , initial weights, and the condition of the neurons at the end of the learning phase.	87
Figure 5.9 – Global irregularity measure Φ_1^g of the TSP and SOM approaches.	88
Figure 5.10–Images I_{14} , I_{22} , and their dilations by SOM, TSP, and lexicographical approaches.	89

List of Tables

Table 2.1 – Gaussian radial basis function (RBF) kernel with $k \in \mathbb{R}$, sigmoidal kernel with $\alpha, b \in \mathbb{R}$, polynomial kernel with $n \in \mathbb{N}, b \in \mathbb{R}$, and inverse multiquadric kernel with $k \in \mathbb{R}_+$ (Müller <i>et al.</i> , 2001).	35
Table 4.1 – Runtime results for calculate the local irregularity index by analytical Wasserstein metric and stabilized Sinkhorn method.	73

List of symbols

\mathbb{R}	Set of real numbers
\mathbb{R}^d	d -dimensional real space
$\overline{\mathbb{R}}$	Extended real number line
$\bigwedge X$	infimum of X
$\bigvee X$	supremum of X
\mathbb{L}	Complete lattice
\mathbb{V}	Complete lattice equipped with a metric d
S	Structuring element
\mathbf{I}	Image \mathbf{I} is a mapping from a nonempty set D to a value set \mathbb{V}
$\mathcal{V} = \mathbb{V}^D$	Set of all images from a domain D to \mathbb{V}
\mathcal{C}_{RGB}	RGB space
\mathcal{C}_{HSL}	HSL space
\mathcal{C}_{m-HSL}	m -HSL space
$V(\mathbf{I})$	Set of values of \mathbf{I}
δ_S^h	h -dilation operator
ε_S^h	h -erosion operator
γ_S^h	h -opening operator
ϕ_S^h	h -closing operator
ψ	Morphological image operator
$\psi_S^M(\mathbf{I})$	Morphological image obtained by applying a morphological operator with structuring element S and marginal order
$\psi_S^W(\mathbf{I})$	Morphological image obtained by applying a morphological operator with structuring element S and Loewner order
$\psi_S^L(\mathbf{I})$	Morphological image obtained by applying a morphological operator with structuring element S and lexicographic order

$\psi_S^S(\mathbf{I})$	Morphological image obtained by applying a morphological operator with structuring element S and the SVM-based approach
$\psi_S^P(\mathbf{I})$	Morphological image obtained by applying a morphological operator with structuring element S and the projection depth approach
$\psi_S^{SPO}(\mathbf{I})$	Morphological image obtained by applying a morphological operator with structuring element S and the stochastic permutation construction order
$\psi_S^{TSP}(\mathbf{I})$	Morphological image obtained by applying a morphological operator with structuring element S and the traveling salesman problem order
$\psi_S^{SOM}(\mathbf{I})$	Morphological image obtained by applying a morphological operator with structuring element S and the self-organizing maps approach
$\arg \min f(x)$	Argument of the minimum of $f(x)$
$\mathcal{D}_p(\mathbf{I}, \mathbf{J})$	Generalized sum of pixel-wise distances between images \mathbf{I} and \mathbf{J}
$\mathcal{W}_p(\mathbf{I}, \mathbf{J})$	Wasserstein metric between images \mathbf{I} and \mathbf{J}
$\mathcal{W}_p(\mathbf{I}, \mathbf{J} W_\ell)$	Wasserstein metric computed restricting the images \mathbf{I} and \mathbf{J} to the local window W_ℓ
$\mathcal{W}_p^r(\mathbf{I}, \mathbf{J})$	Approximation of the Wasserstein metric between images \mathbf{I} and \mathbf{J} via a regularization term of entropic
$\Phi_p^g(\mathbf{I}, \mathbf{J})$	Global irregularity index between images \mathbf{I} and \mathbf{J}
$\Phi_p^l(\mathbf{I}, \mathbf{J})$	Local irregularity index between images \mathbf{I} and \mathbf{J}

Contents

1	Introduction	15
1.1	Outline of the Thesis	16
1.1.1	Problem Statement	17
1.1.2	Research Objective	18
1.1.3	Hypothesis and Methodology	18
1.1.4	Key Contributions	19
1.1.5	Thesis Organization	20
2	Fundamental Definitions	21
2.1	Partially and Totally Ordered Sets	21
2.2	Mathematical Morphology on Complete Lattices	25
2.3	Multivariate Mathematical Morphology	27
2.3.1	Supervised Morphological Approach Based on Support Vector Machine	30
2.3.2	Unsupervised Morphological Approach Based on Statistical Projection Depth	37
2.3.3	Loewner Order and its Corresponding Morphological Approach	40
2.4	The Challenges of False Colors and the Irregularity Issue	43
3	Measuring the Irregularity	47
3.1	Irregularity Measure based on the Wasserstein Metric: The Global Irregularity Index	48
3.2	Computational Analysis of Tiny Color Images	54
4	Calculating the Irregularity Measure	59
4.1	The Local Irregularity Measure for Natural Images	60
4.2	Computational Analysis of Natural Color Images	62
4.3	Computing the Wasserstein Metric with Entropic Regularization	65
4.4	Effect of Structuring Element and Window Size on the Irregularity Measure	71
4.5	Remarks of Execution Time	73
5	The Difficulty of Obtaining a Total Order that Minimizes Irregularity	74
5.1	The Permutation Ordering	75
5.2	Self-Organizing Maps Approach	83
5.3	Simulations of the TSP and SOM Morphological Approaches	88
	Conclusions	91
	Bibliography	93

INTRODUCTION

In this thesis, we present an irregularity measure for multivariate mathematical morphology. Mathematical morphology is a powerful nonlinear theory in the field of mathematics and computation that deals with the analysis and processing of digital images. Specifically, the word “morphology” comes from the aim of analyzing the shape and forms of objects, and the word “mathematical” comes in the sense that the analysis is based on set theory, integral geometry, and lattice theory. Mathematical morphology holds a significant position within the realm of image analysis and processing, serving as a fundamental instrument across various applications. Its extensive scope and adaptable nature render it indispensable for tackling intricate issues within the domain of computer vision and image processing.

Illustrative instances underscore the significance of mathematical morphology in the domains of edge detection and image segmentation. In the context of edge detection, morphological operators enable the amplification of contour attributes, facilitating the discernment of substantial intensity transitions within images. This proves particularly invaluable in scenarios like medical diagnostics, industrial quality assessment, and pattern identification. As for image segmentation, mathematical morphology occupies a pivotal role in partitioning images into regions or objects of interest, thereby being applied within the medical sectors and industry (Serra, 1982; Soille *et al.*, 2003).

Multivariate mathematical morphology refers to the extension of the basic principles of mathematical morphology to multivariate data, allowing for the analysis and processing of digital images that contain multiple channels. Multivariate mathematical morphology has a wide range of applications such as segmentation, remote sensing, image decomposition, medical imaging, automatic image reconstruction, edge detection, and pattern recognition (Braga-Neto & Goutsias, 2004; González-Hidalgo *et al.*, 2015; Rittner *et al.*, 2013; Serra, 2006; Soille, 1999; Najman & Talbot, 2013).

The origins of mathematical morphology can be traced back to its utilization as a method for examining random sets, primarily within the context of the mining industry. However, as time progressed, the technique was expanded to encompass the analysis of multidimensional images within a deterministic framework. This progression began with the examination of binary images, and subsequently extended to include grayscale, color, and multivariate images

(Matheron, 1975; Serra, 1986).

Two basic operations of mathematical morphology, which are called dilation and erosion, were introduced by Matheron and Serra. These operations were initially defined as Minkowski addition and subtraction on subsets of the Euclidean space. Subsequently, Serra and Matheron generalized the morphological operations of dilation and erosion by using complete lattices. A complete lattice is a poset in which all subsets have both an infimum and a supremum. The adoption of complete lattices to generalize set theory in mathematical morphology has demonstrated its utility in broadening the scope of the field. Moreover, the utilization of mathematical morphology defined on complete lattice can simplify the application of morphological operators to grayscale images (Heijmans & Ronse, 1990, 1991; Heijmans, 1991, 1994, 1995; Goutsias *et al.*, 1995; Ronse, 1990).

The extension of morphological processing in the field of multivariate images is facilitated by the utilization of a total order. A widely used approach is based on reduced orderings (h -ordering) combined with look-up tables. An h -ordering ranks the multivariate values according to a surjective mapping h . The ranking of images can be performed based on specific criteria, such as intensity, color, texture, among others. These rankings can also be obtained through the implementation of both supervised and unsupervised approaches (Angulo, 2007; Aptoula & Lefèvre, 2007; Lézoray, 2016).

While using a total order can simplify the handling of multivariate morphological processing as discussed in the paragraph above, Chevallier & Angulo (2016) showed that an intricate problem of irregularity arises when considering a total order and morphological operators. This study formalizes the irregularity issue that naturally arises in multivariate images because the total order do not consider the natural topology of the metric space. In other words, the authors showed that situations may occur where we have elements a , b , and c in the metric space such that $a \leq b \leq c$, but we have $d(a, c) < d(a, b)$, where d denotes the metric. The problem of irregularity introduces imperfections like aliasing in the output images, affecting geometric and topological attributes. Chevallier and Angulo called these imperfections by *irregularity issue*.

1.1 Outline of the Thesis

This thesis is mainly concerned with multivariate mathematical morphology. In this section, we explain the focus of this thesis, including the following key elements:

1.1.1 Problem Statement: This subsection defines the problem being addressed in the thesis and provides background information on the subject.

1.1.2 Research Objective: This subsection addresses our main research objective, explaining the goals of the thesis.

1.1.3 Hypothesis and Methodology: This subsection explains our research hypothesis and the methods we use for its design.

1.1.4 Key Contributions: This subsection highlights the major contributions the thesis makes to the field of multivariate mathematical morphology, detailing the new understanding that is gained as a result of the study.

1.1.5 Structure of the thesis: This subsection provides an overview of the organization and layout of the thesis, outlining the main chapters and sections that make up the research.

1.1.1 Problem Statement

A naturally arising issue in multivariate mathematical morphology is the one demonstrated by [Chevallier & Angulo \(2016\)](#), which is referred to as the irregularity issue. The authors have shown that a total order does not contain enough information to accurately depict the topology of the range set of a multivariate image. Specifically, let the value set \mathbb{V} be a totally ordered set as well as metric space, with metric $d : \mathbb{V} \times \mathbb{V} \rightarrow [0, +\infty)$. Chevallier and Angulo showed that there are some elements $a, b, c \in \mathbb{V}$ such that $a \leq b \leq c$ and $d(a, c) < d(a, b)$ under mild conditions with respect to the connectivity of \mathbb{V} . As a consequence, multivariate morphological operators may introduce irregularities and aliasing on images. It is important to note that the term “aliasing” is commonly observed in digital images and refers to visual distortions that can occur in a low-resolution image unable to represent all color details, such as variations in color and texture. In our context, we refer to such aliasings as irregularities in multivariate mathematical morphology or simply as irregularities.

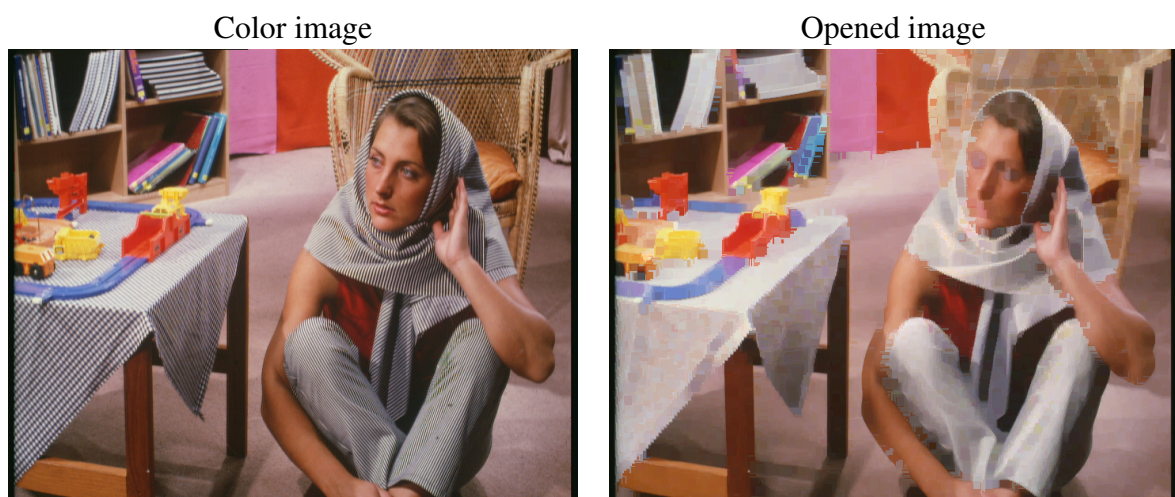


Figure 1.1 – Color image and the result of applying an opening operation.

For example, Figure 1.1 presents a color image and its morphological opening. We can see irregularities in some parts of the opened image, e.g., in the arms of the woman, around the face of the woman, on the chair, on the table, on the red wall, and on the blue book. All irregularities that we can identify are obtained due to the problem of topological inconsistency

with the metric on \mathbb{V} . Therefore, for a total order \leq in \mathbb{V} and a multivariate image $\mathbf{I} : D \rightarrow \mathbb{V}$, the images obtained by morphological operators might present the problem of irregularity.

1.1.2 Research Objective

Let us consider \mathbf{I} as an input image and ψ as a morphological operator. If we apply the operator ψ on the image \mathbf{I} , we obtain the output image $\mathbf{J} = \psi(\mathbf{I})$. It is important to note that if two total orders, denoted as \leq_1 and \leq_2 , are used, the resulting output images, $\mathbf{J}_1 = \psi(\mathbf{I})$ and $\mathbf{J}_2 = \psi(\mathbf{I})$, obtained with orders \leq_1 and \leq_2 , respectively, will differ and will have different irregularities. In this scenario, one may inquire about the degree of irregularity present in images \mathbf{J}_1 and \mathbf{J}_2 when compared to the input image \mathbf{I} . In other words, one may inquire if there exists a measure Φ that quantifies the degree to which image \mathbf{J}_1 presents a greater or lesser degree of irregularity than image \mathbf{J}_2 , both in relation to \mathbf{I} .

Our research objective is to formulate a quantitative measure that evaluates the irregularity in multivariate images produced by a morphological operator. Specifically, given an input multivariate image \mathbf{I} and the output multivariate image $\mathbf{J} = \psi(\mathbf{I})$, with ψ a morphological operator, our aim is to formulate a measure Φ that provides us with a quantitative measure of the irregularity of \mathbf{J} in relation to image \mathbf{I} .

1.1.3 Hypothesis and Methodology

Our goal is to obtain a measure of irregularity Φ that provides us with a percentage of irregularity that makes sense with our visual perception. Specifically, given an image \mathbf{I} and $\mathbf{J} = \psi(\mathbf{I})$, if we visually verify that the image \mathbf{J} has much irregularity, $\Phi(\mathbf{I}, \mathbf{J})$ should give a high value. Conversely, when our visual perception does not indicate much irregularity in \mathbf{J} , $\Phi(\mathbf{I}, \mathbf{J})$ should give a low value.

Additionally, we have the hypothesis that if we calculate the irregularity of an image \mathbf{I} in relation to the image itself, it is natural that $\Phi(\mathbf{I}, \mathbf{I}) = 0$ because we have the same pixels, with the same amount of values and in the same position. This provides an indication that the measure of irregularity needs to take into account the metric d and the values of \mathbf{I} and \mathbf{J} . This realization led us to consider analyzing this problem by solving a transportation problem while considering the minimum cost of transforming image \mathbf{I} into image \mathbf{J} . As a result, we establish an irregularity measure Φ for multivariate mathematical morphology related to the Wasserstein metric.

We analyze the results of the irregularity measure for 100 distinct tiny color images using different orders and morphological operators. For comparison purposes, we use two approaches involving partial orders and three approaches involving total orders.

It is worth noting that unfortunately, it is not possible to calculate the Wasserstein metric on natural images due to computational complexity. However, we develop a measure for

irregularity in natural images, which we refer to in this work as the local irregularity index. In a similar manner, we analyze the results of the local irregularity measure for 100 distinct natural color images. For comparison purposes, we use the same five orders used in the analysis of Φ . In addition, we present a theorem showing that the local irregularity index is a lower bound for the global irregularity index.

Furthermore, we consider the entropic regularized method which adds a penalty to the transportation problem, allowing us to obtain an approximation for the Wasserstein metric with a low computational complexity. In this thesis, we utilize the Sinkhorn algorithm and find that the calculation of irregularity can be performed using the entropic regularization.

Finally, we developed two new approaches to demonstrate the hardness of obtaining a total order that minimizes irregularity. The first approach is based on the traveling salesman problem (TSP). The second approach is based on self-organizing maps (SOMs). Both approaches were tested on a set of tiny color images and the results were compared with the existing methods performed before.

1.1.4 Key Contributions

This thesis makes a contribution to the field of multivariate mathematical morphology by incorporating optimal transport techniques to obtain an irregularity measure for multivariate mathematical morphology.

Furthermore, this research presented innovative in addressing the irregularity issue in a multivariate mathematical morphology using the Wasserstein metric, and has resulted in the publication of two research works.

The first work was presented at the IAPR International Conference on Discrete Geometry and Mathematical Morphology (DGMM 2021), in Sweden, and was published as a book chapter:

Valle, Marcos Eduardo; Francisco, Samuel; Granero, Marco Aurélio and Velasco-Forero, Santiago. *Measuring the Irregularity of Vector-Valued Morphological Operators Using Wasserstein Metric*. In: Lindblad J., Malmberg F., Sladoje N. (eds). Discrete Geometry and Mathematical Morphology. DGMM 2021. Lecture Notes in Computer Science, vol. 12708. Springer, Cham.

The second work was published in the Journal of Mathematical Imaging and Vision in 2022:

Valle, Marcos Eduardo; Francisco, Samuel; Granero, Marco Aurélio and Velasco-Forero, Santiago. *Irregularity Index for Vector-Valued Morphological Operators*. Journal of Mathematical Imaging and Vision, 64 (7), 754–770, 2022.

Additionally, a manuscript is currently being prepared for submission to the scientific community, which explains the hardness of obtaining a total order that minimizes the irregularity.

1.1.5 Thesis Organization

The thesis is organized with the following structure:

In Chapter 2, called [Fundamental Definitions](#), we review the main mathematical concepts related to multivariate mathematical morphology, such as the concepts of complete lattice, adjunction, dilation, erosion, opening, and closing operations. In addition, we discuss some ordering approaches for multivariate images such as the marginal, Loewner, lexicographic, supervised based on SVM, and unsupervised projection depth orderings. Finally, we discuss the challenges in multivariate mathematical morphology that naturally arise when using a partial order or a total order. One of the challenges is what we present as the irregularity issue.

In Chapter 3, called [Measuring the Irregularity](#), we present our theory of the global irregularity index for two images \mathbf{I} and $\mathbf{J} = \psi(\mathbf{I})$. For this purpose, we recall the Wasserstein metric and the generalized sum of pixel-wise distances and then define the global irregularity index. We finish this chapter with illustrative examples in some tiny color images.

In Chapter 4, called [Calculating the Irregularity Measure](#), we present our theory for handling the irregularity index for natural color images. We define the local irregularity index and present the results in natural images. Furthermore, we discuss the entropic regularized methods to approximate the Wasserstein metric and the changes in the local irregularity index with different sizes of the local window or structuring element.

In Chapter 5, called [The Hardness of Obtaining a Total Order that Minimizes the Irregularity](#), we present two new morphological approaches based on total order. The first one is called the Traveling Salesman Problem (TSP) approach and the second is called the self-organizing maps (SOMs) approach. We present the computational results of the irregularity measures obtained from these two approaches.

Finally, we finish this thesis with our [Conclusions](#) and some possible recommendations for future works.

FUNDAMENTAL DEFINITIONS

In this chapter we discuss the fundamental definitions that are important for our work regarding mathematical morphology (MM).

Mathematical morphology (MM) emerged in the mid-1960s by Georges Matheron and Jean Serra at École des Mines in Paris. These researches introduced a set formalism for analyzing binary images. The advancement of research in mathematical morphology by these researchers continued with the extension to complete lattices. Their work was extended by Heijmans (1987) where he devoted a study to the \mathbb{T} -operators on a complete lattice with the assumption that \mathbb{T} is an abelian automorphism group. This approach characterized mathematical morphology as an algebraic structure that proved convenient in expanding the scope of mathematical morphology (Matheron, 1975; Serra, 1982; Heijmans & Ronse, 1990; Ronse, 1990).

In the following, we present a framework for mathematical morphology that utilizes the algebraic structure of complete lattices, which is well-suited for the binary and grayscale images (Heijmans, 1995; Ronse, 1990) and that there are extensive works for multivariate images (Angulo, 2007; Aptoula & Lefèvre, 2007; Velasco-Forero & Angulo, 2014).

2.1 Partially and Totally Ordered Sets

Morphological operators need an ordering relationship between the elements to be processed. Thus, it is fundamental to define binary relations, partial orders, and total orders.

Definition 2.1 (Binary relation). Given two sets X and Y , a binary relation R over X and Y is a subset of $X \times Y = \{(x, y) | x \in X \text{ and } y \in Y\}$.

The statement $(x, y) \in R$ means that the element x of X is related to the element y of Y and we write xRy .

A binary relation R in $P \times P$ is called a relation on P . For example, the graph $G(f) = \{(x, f(x)) | x \in \mathbb{R}\} \subset \mathbb{R} \times \mathbb{R}$ of a function $f : \mathbb{R} \rightarrow \mathbb{R}$ is a relation on $P = \mathbb{R}$.

Definition 2.2 (Partial order). Given a nonempty set P , a relation on P is a partial order, denoted by \leq , if the following properties holds for all $x, y, z \in P$:

1. $x \leq x$. (reflexive)
2. $x \leq y$ and $y \leq x \implies x = y$. (antisymmetric)
3. $x \leq y$ and $y \leq z \implies x \leq z$. (transitive)

Remark 2.1. A binary relation that is reflexive and transitive is called a preorder. All partial orders are preorders, but there exist preorders that are not partial orders because they do not satisfy the antisymmetry property.

Definition 2.3 (Partially ordered set). A set P endowed with a partial order \leq is called a partially ordered set or poset and denoted by the pair (P, \leq) .

The converse of a relation R on P is the relation \check{R} on P such that $x\check{R}y \iff yRx$, for all $x, y \in P$.

Given any poset P we can form a new poset P^∂ (the dual of P) by defining $x \leq y$ to hold in P^∂ if and only if $y \leq x$ holds in P . For each statement about the poset P there corresponds a statement about P^∂ (Birkhoff, 1993; Davey & Priestley, 2002).

Definition 2.4 (Dual of a poset P). The dual of a poset P is the poset P^∂ defined by the converse partial ordering relation on the same elements.

Let us give some examples of posets.

Example 2.1. Let $\mathbb{R}^2 = \mathbb{R} \times \mathbb{R}$ be the Euclidean space and let \leq_M be the partial order relation given by

$$(x_1, y_1) \leq_M (x_2, y_2) \iff x_1 \leq x_2 \text{ and } y_1 \leq y_2.$$

The pair (\mathbb{R}^2, \leq_M) is a poset since the relation is reflexive, antisymmetric, and transitive.

Note in Example 2.1 that if we consider $\mathbf{x} = (2, 3)$, $\mathbf{y} = (5, 2) \in \mathbb{R}^2$, then $(2, 3) \not\leq_M (5, 2)$ and $(5, 2) \not\leq_M (2, 3)$, where $\not\leq_M$ means that $\mathbf{x} \leq_M \mathbf{y}$ is not valid. Thus, in a poset P , two elements $x, y \in P$ does not need to be comparable, i.e., given $x, y \in P$, we do not necessarily have $x \leq y$ or $y \leq x$. As a result, we have the following definition of totally ordered set.

Definition 2.5 (Totally ordered set and total order). A total order is a partial order in which any two elements are comparable. A set endowed with a total order is called a totally ordered set or a chain.

Remark 2.2. Note that a preorder is a more general concept than a partial order, and a partial order is more general than a total order.

Example 2.2. The sets $\mathbb{N}, \mathbb{Z}, \mathbb{Q}, \mathbb{R}, [a, b] = \{x \in \mathbb{R} : a \leq x \leq b \text{ and } a < b\}$ with the usual order \leq are chains.

Example 2.3. This example illustrates the partial order known as the marginal order. Let $P = \mathbb{R}^d = \{(x_1, x_2, \dots, x_d) : x_i \in \mathbb{R}, d > 1\}$ be the d -dimensional space endowed with the order \leq_M defined by

$$\mathbf{x} \leq_M \mathbf{y} \iff x_i \leq y_i \text{ for all } i \in \{1, 2, \dots, d\},$$

where $\mathbf{x} = (x_1, x_2, \dots, x_d)$ and $\mathbf{y} = (y_1, y_2, \dots, y_d)$. The pair (P, \leq_M) is a poset and, like Example 2.1, there are elements of P that are not comparable for all $d > 1$. For instance, let $\mathbf{x} = (1, 2, 255)$, $\mathbf{y} = (5, 10, 4)$ be elements of \mathbb{R}^3 , we have that \mathbf{x} and \mathbf{y} are not comparable.

Example 2.4. This example presents a total order known as the alphabetical order, dictionary order, lexical order, or lexicographical ordering. This order is defined in many mathematical contexts. According to [Aptoula & Lefèvre \(2008\)](#), the lexicographical ordering is defined in a conditional manner based on some marginal components. Consider n posets (X_1, \leq_1) , (X_2, \leq_2) , \dots , (X_n, \leq_n) . We define the lexicographical ordering \leq_L on $X_1 \times \dots \times X_n = \prod_{i=1}^n X_i$, as

$$\mathbf{x} \leq_L \mathbf{y} \iff \begin{cases} x_1 <_1 y_1 & \text{or} \\ x_1 =_1 y_1 \text{ and } x_2 <_2 y_2 & \text{or} \\ x_1 =_1 y_1, x_2 =_2 y_2, \text{ and } x_3 <_3 y_3 & \text{or} \\ \vdots & \\ x_1 =_1 y_1, x_2 =_2 y_2, \dots, x_{n-1} =_{n-1} y_{n-1}, \text{ and } x_n \leq_n y_n, & \end{cases}$$

where $\mathbf{x} = (x_1, x_2, \dots, x_n)$, $\mathbf{y} = (y_1, y_2, \dots, y_n) \in X_1 \times \dots \times X_n$. In a compact way, we can write $(x_1, \dots, x_n) \leq_L (y_1, \dots, y_n)$ if, and only if, there is $i \in \{1, \dots, n-1\}$ such that $x_i <_i y_i$ and for all $j < i$, $x_j =_j y_j$, or $x_n \leq_n y_n$ and for all $j < n$, $x_j =_j y_j$.

If $P = [0, 1] \times [0, 1] \times [0, 1] = [0, 1]^3$ and we consider in $[0, 1]$ the usual order \leq , then (P, \leq_L) is a poset. Observe now that all elements of P are comparable, i.e., given $\mathbf{x}, \mathbf{y} \in P$, we have that $\mathbf{x} \leq_L \mathbf{y}$ or $\mathbf{y} \leq_L \mathbf{x}$ and therefore (P, \leq_L) is a chain.

Remark 2.3. In Examples 2.1 and 2.3, (\mathbb{R}^2, \leq_M) and (\mathbb{R}^d, \leq_M) , with $d > 1$, are posets, but they are not chains. Furthermore, if in Example 2.4 the sets (X_i, \leq_i) are chains, then $\left(\prod_{i=1}^n X_i, \leq_L\right)$ is also a chain.

Moreover, for a poset P , we have the following definitions ([Birkhoff, 1993](#)).

Definition 2.6 (Least and greatest element). Let P be a poset. We say that $l \in P$ is the least element in P if $l \leq x$, for all $x \in P$. An element $u \in P$ is the greatest element in P if $x \leq u$, for all $x \in P$.

A poset P can have at most one least and one greatest element. Indeed, if $l_1, l_2 \in P$ are two least elements in P , then $l_1 \leq l_2$ and $l_2 \leq l_1$. Therefore, $l_1 = l_2$ by the antisymmetric

property. Similarly, if $u_1, u_2 \in P$ are two greatest element in P , then $u_1 \geq u_2$ and $u_2 \geq u_1$ and, in the same way, we have $u_1 = u_2$.

Next, we have the following important definitions.

Definition 2.7 (Lower and upper bound). Let P be a poset and $X \subset P$. A lower bound or minorant of X is an element $a \in P$ such that $a \leq x$, for all $x \in X$. An upper bound or majorant of X is an element $b \in P$ such that $x \leq b$, for all $x \in X$.

Definition 2.8 (Infimum and supremum). Let P be a poset and $X \subset P$ a nonempty set. We denote $\bigwedge X$, called the infimum or meet of X , the greatest lower bound of X . We denote $\bigvee X$, called the supremum or join of X , the least upper bound of X .

Remark 2.4. If l is the least element of X , then $\bigwedge X = l$ and if u is the greatest element of X , then $\bigvee X = u$.

If $X = \{x_i : i \in I\}$, we write $\bigwedge X = \bigwedge_{i \in I} x_i$ and $\bigvee X = \bigvee_{i \in I} x_i$. In particular, if $I = \{1, 2, 3, \dots, n\}$, we denote $\bigwedge X = \bigwedge_{i=1}^n x_i$ and $\bigvee X = \bigvee_{i=1}^n x_i$. Furthermore, if $X = \{x, y\}$, we denote $\bigwedge X = x \wedge y$ and $\bigvee X = x \vee y$.

Example 2.5. Let $P = \mathbb{R}$ be the real numbers set, let $X_1 = [0, 1)$ and $X_2 = \{0, 1, 2, 3, \dots, 255\}$ be subsets of P . Then $\bigwedge X_1 = 0$, $\bigvee X_1 = 1$, $\bigwedge X_2 = \bigwedge_{i=0}^{255} i = 0$, and $\bigvee X_2 = \bigvee_{i=0}^{255} i = 255$.

Remark 2.5. Note that the infimum and supremum of a subset X of a poset P may or may not belong to X .

We shall be interested in a poset P that $x \wedge y$ and $x \vee y$ exist for all elements of P . Thus, we will need the following important definitions (Birkhoff, 1993; Grätzer & others, 2003; Davey & Priestley, 2002).

Definition 2.9 (Lattice). Let \mathbb{L} be a poset. \mathbb{L} is a lattice if for all $x, y \in \mathbb{L}$, the infimum $x \wedge y$ and the supremum $x \vee y$ exist and belong to \mathbb{L} .

Definition 2.10 (Complete lattice). A lattice \mathbb{L} is a complete lattice if for all subset $X \subset \mathbb{L}$, we have $\bigwedge X \in \mathbb{L}$ and $\bigvee X \in \mathbb{L}$.

Definition 2.11 (Bounded lattice). A lattice \mathbb{L} is bounded if $\bigwedge \mathbb{L} \in \mathbb{L}$ and $\bigvee \mathbb{L} \in \mathbb{L}$. In this case, we denote $0_{\mathbb{L}} = \perp = \bigwedge \mathbb{L}$ and $1_{\mathbb{L}} = \top = \bigvee \mathbb{L}$.

Since $\mathbb{L} \subset \mathbb{L}$, it implies that every complete lattice is bounded. Moreover, if a poset P is a chain, then P is a lattice. In fact, given $x, y \in P$, we have $x \leq y$ or $y \leq x$. If $x \leq y$, then $x \wedge y = x$ and $x \vee y = y$. Otherwise, $x \wedge y = y$ and $x \vee y = x$.

To finish this section, we give some examples of lattices.

Example 2.6. Consider $\mathbb{L}_1 = \mathbb{R}$, $\mathbb{L}_2 = [0, 1]$ and $\mathbb{L}_3 = \{0, 1, \dots, 255\}$ with the usual order \leq . All the sets are lattices, \mathbb{L}_2 and \mathbb{L}_3 are complete lattices and as \mathbb{L}_1 is not bounded, then \mathbb{L}_1 is not a complete lattice.

Note that every lattice can be embedded into a bounded lattice by adding a least and a greatest element. For our example, we can add $-\infty$ and $+\infty$ to \mathbb{L}_1 . In this case, we denote $\overline{\mathbb{R}} = \mathbb{R} \cup \{-\infty, +\infty\}$, called the extended real numbers line. The set $(\overline{\mathbb{R}}, \leq)$ is another example of a complete lattice and, therefore, a bounded lattice.

Example 2.7. Let (\mathbb{R}^d, \leq_L) and $([0, 1]^d, \leq_L)$ with $d \geq 2$. In this case, \mathbb{R}^d is a lattice and $[0, 1]^d$ is a complete lattice.

2.2 Mathematical Morphology on Complete Lattices

In a complete lattice, four elementary morphological operators are defined in the following way:

Definition 2.12 (Dilation operator). Let (\mathbb{L}_1, \leq_1) and (\mathbb{L}_2, \leq_2) be two complete lattices. A dilation from (\mathbb{L}_1, \leq_1) to (\mathbb{L}_2, \leq_2) is an operator $\delta : \mathbb{L}_1 \rightarrow \mathbb{L}_2$ that commutes with the supremum:

$$\delta \left(\bigvee_{i \in I} x_i \right) = \bigvee_{i \in I} \delta(x_i), \quad \forall (x_i)_{i \in I} \subset \mathbb{L}_1.$$

Definition 2.13 (Erosion operator). Let (\mathbb{L}_1, \leq_1) and (\mathbb{L}_2, \leq_2) be two complete lattices. An erosion from (\mathbb{L}_1, \leq_1) to (\mathbb{L}_2, \leq_2) is an operator $\varepsilon : \mathbb{L}_1 \rightarrow \mathbb{L}_2$ that commutes with the infimum:

$$\varepsilon \left(\bigwedge_{i \in I} x_i \right) = \bigwedge_{i \in I} \varepsilon(x_i), \quad \forall (x_i)_{i \in I} \subset \mathbb{L}_1.$$

Definition 2.14 (Anti-dilation operator). Let (\mathbb{L}_1, \leq_1) and (\mathbb{L}_2, \leq_2) be two complete lattices. An anti-dilation from (\mathbb{L}_1, \leq_1) to (\mathbb{L}_2, \leq_2) is an operator $\bar{\delta} : \mathbb{L}_1 \rightarrow \mathbb{L}_2$ if

$$\bar{\delta} \left(\bigvee_{i \in I} x_i \right) = \bigwedge_{i \in I} \bar{\delta}(x_i), \quad \forall (x_i)_{i \in I} \subset \mathbb{L}_1.$$

Definition 2.15 (Anti-erosion operator). Let (\mathbb{L}_1, \leq_1) and (\mathbb{L}_2, \leq_2) be two complete lattices. An anti-erosion from (\mathbb{L}_1, \leq_1) to (\mathbb{L}_2, \leq_2) is an operator $\bar{\varepsilon} : \mathbb{L}_1 \rightarrow \mathbb{L}_2$ if

$$\bar{\varepsilon} \left(\bigwedge_{i \in I} x_i \right) = \bigvee_{i \in I} \bar{\varepsilon}(x_i), \quad \forall (x_i)_{i \in I} \subset \mathbb{L}_1.$$

Remark 2.6. A dilation δ and an erosion ε are increasing operators, i.e., for all $x, y \in \mathbb{L}_1$, $x \leq_1 y$ implies $\delta(x) \leq_2 \delta(y)$ and $\varepsilon(x) \leq_2 \varepsilon(y)$. Indeed, if $x \leq_1 y$ then $\delta(x) \leq_2 \delta(x) \vee \delta(y) = \delta(x \vee y) = \delta(y)$ and $\varepsilon(x) = \varepsilon(x \wedge y) = \varepsilon(x) \wedge \varepsilon(y) \leq_2 \varepsilon(y)$.

A fundamental notion in this algebraic framework is the one of adjunction (Gierz *et al.*, 1980; Heijmans & Ronse, 1990; Velasco-Forero & Angulo, 2014).

Definition 2.16 (Adjunction). Let \mathbb{L} be a complete lattice and $\delta, \varepsilon : \mathbb{L} \rightarrow \mathbb{L}$ be operators. We say that (ε, δ) is an adjunction if for every $x, y \in \mathbb{L}$, we have

$$\delta(x) \leq y \iff x \leq \varepsilon(y). \quad (2.1)$$

In an adjunction (ε, δ) , ε is called the upper adjoint and δ is called the lower adjoint.

Remark 2.7. Note that (2.1) can be expressed in a dual form with \geq instead of \leq , i.e., we can write

$$\varepsilon(y) \geq x \iff y \geq \delta(x). \quad (2.2)$$

Therefore, according to Heijmans & Ronse (1990), δ and ε always play a dual role. In fact, (ε, δ) is an adjunction on (\mathbb{L}, \leq) if, and only if, (δ, ε) is an adjunction on the dual lattice $(\mathbb{L}^\partial, \geq)$.

If (ε, δ) is an adjunction, then δ is a dilation and ε is an erosion (Heijmans, 1994). Furthermore, for each dilation δ , there is only one erosion ε such that (ε, δ) is an adjunction. Similarly, for each erosion ε , there is only one dilation δ such that (ε, δ) is an adjunction (Gierz *et al.*, 1980; Heijmans & Ronse, 1990).

Remark 2.8. The concept of adjunction between dilation and erosion operators in mathematical morphology is closely related to the concept of Galois connection between posets (Atif *et al.*, 2013; Birkhoff, 1993; Heijmans & Ronse, 1990; Velasco-Forero & Angulo, 2014). Let (P, \leq_1) and (Q, \leq_2) be two posets. Let $\alpha : P \rightarrow Q$ and $\beta : Q \rightarrow P$ be two maps. Then (α, β) forms a Galois connection between (P, \leq_1) and (Q, \leq_2) if for every $x \in P$ and $y \in Q$, we have

$$x \leq_1 \beta(y) \iff y \leq_2 \alpha(x). \quad (2.3)$$

Dilation, erosion, anti-dilation, and anti-erosion are elementary morphological operators because they can be used to compose many other operators, such as opening, closing, and the morphological gradient (Banon & Barrera, 1993; Serra, 1986, 1988; Ronse, 1990; Heijmans & Ronse, 1991).

Definition 2.17 (Opening and closing operators). Let \mathbb{L} be a complete lattice, and let (ε, δ) be an adjunction. An operator $\gamma : \mathbb{L} \rightarrow \mathbb{L}$ defined by $\gamma = \delta \circ \varepsilon := \delta\varepsilon$ is called opening or, more precisely, algebraic opening. An operator $\phi : \mathbb{L} \rightarrow \mathbb{L}$ defined by $\phi = \varepsilon \circ \delta := \varepsilon\delta$ is called closing or, more specifically, algebraic closing.

The opening and closing operators are used, for example, in granulometry and noise reduction, as pointed out by Heijmans (1995) and Soille (1999).

To finish this section, we address morphological dilation and erosion operators defined through a structuring element S (Soille, 1999).

We regard the set of values \mathbb{V} as a complete lattice structure and the image \mathbf{I} as a mapping from a nonempty set of points D to the set of values \mathbb{V} , that is, $\mathbf{I} : D \rightarrow \mathbb{V}$. The set of all images $\mathbf{I} : D \rightarrow \mathbb{V}$ is denoted by $\mathcal{V} = \mathbb{V}^D$ and, in this work, we consider D to be finite with $N_D = \text{Card}(D)$ points. Furthermore, D is contained in \mathcal{E} , where $(\mathcal{E}, +)$ is an abelian group. For our purposes, we can take $\mathcal{E} = \mathbb{R}^2$ or $\mathcal{E} = \mathbb{Z}^2$ with the usual addition.

In the event that the set of values \mathbb{V} forms a complete lattice, the operators $\delta_S, \varepsilon_S : \mathcal{V} \rightarrow \mathcal{V}$ defined by the following equations, where $S \subseteq \mathcal{E}$ is a finite set, are a dilation and an erosion respectively:

$$\delta_S(\mathbf{I})(p) = \bigvee_{\substack{s \in S \\ p-s \in D}} \mathbf{I}(p-s) \quad \text{and} \quad \varepsilon_S(\mathbf{I})(p) = \bigwedge_{\substack{s \in S \\ p+s \in D}} \mathbf{I}(p+s), \quad \text{for all } p \in D. \quad (2.4)$$

In other words, a dilation operator acts on an image \mathbf{I} of \mathcal{V} and transforms it into an image \mathbf{J}_1 of \mathcal{V} . For each $p \in D$, the dilation is given by the supremum of $\mathbf{I}(p-s)$ for s in the structuring element S such that $p-s$ belongs to the domain of \mathbf{I} . Similarly, an erosion operator acts on an image \mathbf{I} of \mathcal{V} and transforms it into an image \mathbf{J}_2 of \mathcal{V} . Similarly, for each $p \in D$, the erosion is given by the infimum of $\mathbf{I}(p+s)$ for s in the structuring element S such that $p+s$ belongs to the domain of \mathbf{I} .

2.3 Multivariate Mathematical Morphology

A multivariate image \mathbf{I} is obtained when $\mathbb{V} \subset \overline{\mathbb{R}}^d$, with $d \geq 2$, i.e., $\mathbf{I} : D \rightarrow \mathbb{V} \subset \overline{\mathbb{R}}^d$. A color image is an example of a multivariate image (Valle *et al.*, 2022; Velasco-Forero & Angulo, 2014). In practice, we usually consider a color image \mathbf{I} mapping $x = (i, j) \in D$ to a vector $\mathbf{I}(x) \in [0, 1]^3$, where $\mathbb{V} = [0, 1]^3$ is the RGB space denoted by \mathcal{C}_{RGB} . For instance, if $\mathbf{I}(x_1) = (0, 0, 0)$, $\mathbf{I}(x_2) = (1, 1, 1)$, $\mathbf{I}(x_3) = (0, 0, 1)$, and $\mathbf{I}(x_4) = (0.005, 0, 0)$, then we have for the pixels $x_1, x_2, x_3, x_4 \in D$, the colors pure black, pure white, pure blue, and a color that resembles black, respectively.

Figure 2.1 shows an example of a color image. The image \mathbf{I} has a resolution of 481×321 . For each pixel $x \in D$, we assigned a color $\mathbf{I}(x) \in \mathcal{C}_{RGB}$. The color image \mathbf{I} shown in Figure 2.1 belongs to the Berkeley Segmentation Dataset (BSDS) available at <https://www2.eecs.berkeley.edu/Research/Projects/CS/vision/grouping/segbench/>.

The RGB color space is only one representation of a color space. We point out that there are several other color spaces in the literature, for example, the HSV space, HSL space, CIELab space, and so on (Hanbury & Serra, 2001b,a; Angulo & Serra, 2003; Valle & Valente, 2016).

For instance, the HSV color model is denoted by \mathcal{C}_{HSV} , and the HSL color model is denoted by \mathcal{C}_{HSL} . The HSV color model represents a color using three components (h, s, v) where h means hue, s means saturation, and v means value, and the HSL color model represent



Figure 2.1 – Illustrative example of a color image $I : D \rightarrow \mathcal{C}_{RGB}$.

a color using three components (h, s, l) , where the value v of the third component in \mathcal{C}_{HSV} is replaced by l that means lightness. It is observed that the hue component represents the type of color like red, blue, and green and is usually represented as an angle around a color wheel. Saturation controls the intensity of the color, with 0 saturation resulting in a grayscale color and maximum saturation representing the purest form of the color. Lightness controls the brightness, where 0 represents black, 1 represents white, and 0.5 corresponds to the original color. The HSL color space facilitates color transformations like hue rotations and saturation adjustments, which are essential in image processing tasks such as color correction and enhancement.

Furthermore, we have some variants of color spaces as the variant space of HSL color space, known as the m -HSL color space or m -HCL color space. The m -HCL is an extension of the traditional HSL model. It offers a unique geometric representation with a cone-like shape having two tips (vertices) located at $(0, 0, 1)$ and $(0, 0, -1)$. The circular base of this cone intersects the origin and is parallel to the xy -plane. This geometric representation allows for a more comprehensive and effective representation of colors. In the m -HCL color space, chroma (c) replaces saturation, which is calculated as the difference between the maximum and minimum RGB color channel values. Additionally, luminance (l) is modified to $\tilde{l} = 2l - 1$. In Subsection 2.3.3, we will employ the m -HCL color space, as proposed by [Burgeth & Kleefeld \(2013\)](#), for the Loewner approach.

Multivariate erosions and dilations can be defined using (2.4) as long as the set \mathbb{V} is a complete lattice. The main challenge of multivariate mathematical morphology is to find an appropriate ordering for vectors. Although there are several studies with techniques for ordering multivariate data, they can be broadly grouped into several non-exclusive categories as outlined in the literature ([Aptoula & Lefèvre, 2007](#); [Barnett, 1976](#); [Hardie & Arce, 1991](#); [Velasco-Forero & Angulo, 2011](#)). The categories are:

Marginal ordering (M-ordering): The marginal ordering is obtained by comparing separately the components of the vectors. Precisely, the components u_1, u_2, \dots, u_d and v_1, v_2, \dots, v_d of the vectors $\mathbf{u}, \mathbf{v} \in \mathbb{V} \subset \overline{\mathbb{R}}^d$ are ordered independently (pointwise ordering), i.e., for all $\mathbf{u}, \mathbf{v} \in \mathbb{V}$, $\mathbf{u} \leq_M \mathbf{v} \iff u_i \leq v_i \ \forall i \in \{1, 2, \dots, d\}$. Note that this order is the partial order \leq_M given in Example 2.3.

Conditional ordering (C-ordering): In C-ordering or conditional ordering we build the ordered set of vectors by ordering of one or more components selected sequentially according to different conditions. The ordering of vectors is conditioned upon the particular marginal set of ranked components (Angulo, 2007).

An example of C-ordering is the lexicographical order \leq_L given in Example 2.4.

Partial ordering (P-ordering): The P-ordering or partial ordering is based on the partition of the vectors into groups, such that the groups can be distinguished with respect to rank or extremeness. It is important to point out that the word partial here is an abuse of terminology because there are total orders that belong to this group. Additionally, in a general way, these groups are not mutually exclusive, i.e., it is common for instance to have a P-ordering that is also an R-ordering.

Reduced ordering (R-ordering): According to Goutsias *et al.* (1995) and Aptoula & Lefèvre (2007), in an R-ordering or reduced ordering the vectors are ranked according to a surjective mapping h from the value set \mathbb{V} into a complete lattice \mathbb{L} as follows:

$$\forall \mathbf{u}, \mathbf{v} \in \mathbb{V}, \ \mathbf{u} \leq_h \mathbf{v} \iff h(\mathbf{u}) \leq_{\mathbb{L}} h(\mathbf{v}). \quad (2.5)$$

Goutsias *et al.* (1995) has proposed the use of reduced orderings for the development of efficient multivariate morphological operators. Precisely, combining (2.5) with lookup tables (LUTs), as suggested by Velasco-Forero & Angulo (2014), we are able to use morphological operators in grayscale to produce adequate multivariate morphological operators. Together with a LUT, a reduced ordering given by (2.5) becomes a total ordering on the set $V(\mathbf{I}) = \{\mathbf{I}(p) : p \in D\}$ of values of an image \mathbf{I} . Hence, we can define the h -dilation δ_S^h and the h -erosion ε_S^h of an image \mathbf{I} by a structuring element S by (2.4). Moreover, we can define the h -opening γ_S^h and h -closing ϕ_S^h operators of an image \mathbf{I} by a structuring element S as

$$\gamma_S^h(\mathbf{I}) = \delta_S^h(\varepsilon_S^h(\mathbf{I})) \quad \text{and} \quad \phi_S^h(\mathbf{I}) = \varepsilon_S^h(\delta_S^h(\mathbf{I})). \quad (2.6)$$

As an example, Figure 2.2 shows the dilation and the erosion of the image \mathbf{I} in Figure 2.1 obtained through the lexicographical order given by Example 2.4. The structuring element S is a square of size 9×9 . Observe that the dilated image $\delta_S^L(\mathbf{I})$ is clearer than the image \mathbf{I} and the eroded image $\varepsilon_S^L(\mathbf{I})$ is darker than the image \mathbf{I} .

Furthermore, according to Velasco-Forero & Angulo (2014), there are different multivariate orderings implemented by h -mapping based reduced ordering. For instance, there

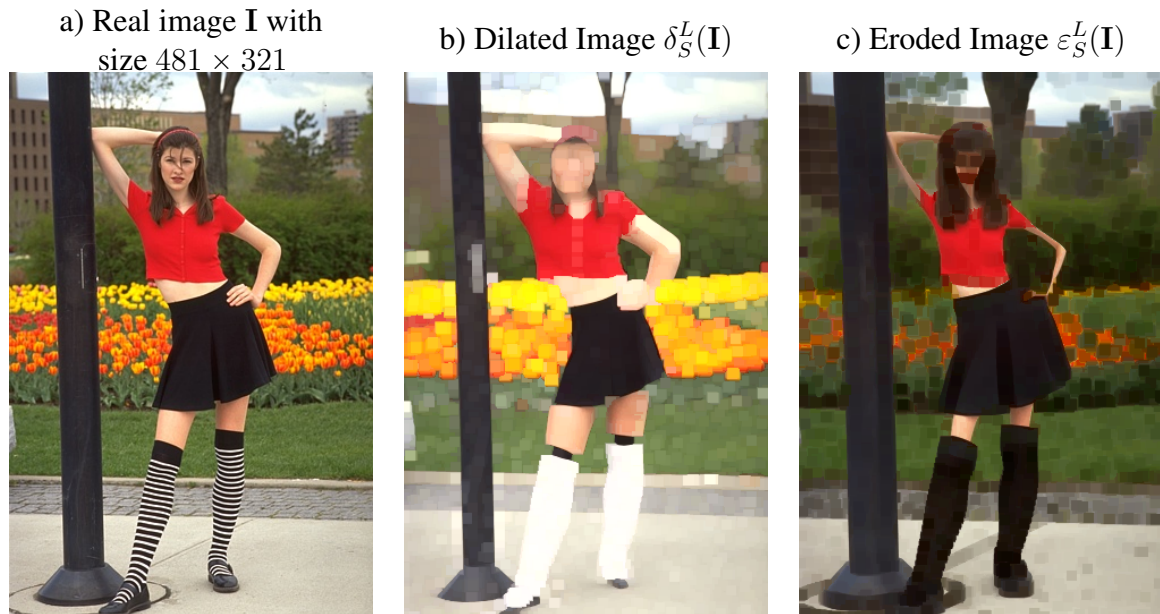


Figure 2.2 – Illustrative example of images obtained by morphological operators. Figure a) shows the color image I . Figure b) shows the dilated image using the h -lexicographical order and Figure c) shows the eroded image using the h -lexicographical order.

are the supervised morphological approaches and the unsupervised morphological approaches. In a supervised morphological approach, the algorithm is provided with labeled training data and uses this information to learn how to rank the image values. An example are morphological operators based on support vector machine (SVM). In an unsupervised morphological approach, the algorithm does not use any labeled data and instead relies on the intrinsic properties of the data itself to determine the ordering. An example is the morphological approach based on the statistical projection depth function.

2.3.1 Supervised Morphological Approach Based on Support Vector Machine

The supervised approach is obtained with an R-ordering where the mapping h is defined using a supervised learning. The goal of supervised learning is to find a mapping from input data to the corresponding output labels or values. The training data is labeled, meaning that it includes both the input data and the corresponding output labels or values. The supervised morphological approach involves training a model to recognize patterns in labeled training data, which can be used to create mappings that order the input data.

There are several types of supervised approaches, such as linear regression, logistic regression, decision trees, support vector machine (SVM), and neural networks. For instance, [Velasco-Forero & Angulo \(2011\)](#) used the support vector machine (SVM) to calculate h -supervised ordering as follows.

A support vector machine (SVM) is a powerful machine-learning method with a

variety of applications. SVMs are frequently used for classification and regression tasks. They work by finding the best boundary or hyperplane that separates the different classes in the training data. The best boundary is the one that maximizes the margin of separation, which is the distance between the boundary and the closest data points from each class. The data points closest to the boundary are called support vectors (Vapnik, 1998).

According to Cristianini & Shawe-Taylor (2000), the simplest problems for SVM are linearly separable problems.

Definition 2.18 (Linearly separable set). Let $T = \{(\mathbf{x}_1, y_1), (\mathbf{x}_2, y_2), \dots, (\mathbf{x}_n, y_n)\} \subset \mathbb{R}^d \times \{1, -1\}$ be a labeled training set, where y_i defines class label of the i -th sample. If there are $\mathbf{w} \in \mathbb{R}^d$, $b \in \mathbb{R}$, and a positive number C such that $y_i (\mathbf{w}^t \mathbf{x}_i + b) \geq C$, for all $i \in \{1, 2, \dots, n\}$, where $\mathbf{w}^t \mathbf{x}$ denotes the inner product of \mathbf{w} and \mathbf{x} , then the training set T is called linearly separable.

Let T be a linearly separable training set as in Definition 2.18. Our goal is to find a hyperplane that separates the different classes in the training data. In other words, our goal is to find a function $f : \mathbb{R}^d \rightarrow \{1, -1\}$ such that $f(\mathbf{x}) = \text{sgn}(h(\mathbf{x}))$ takes in input data and produces a prediction about the output label. The discrimination function h is learned from the labeled training data T . In this context, $h(\mathbf{x}) = \mathbf{w}^t \mathbf{x} + b$.

It should be noted that the equation $h(\mathbf{x}) = \mathbf{w}^t \mathbf{x} + b = 0$ separates \mathbb{R}^d into two regions that correspond to the labels of the two classes of y_i . However, usually there are infinitely hyperplanes that separate the training set T . Therefore, as noted by Vapnik (1998), the best hyperplane $\mathbf{w}^t \mathbf{x} + b = 0$ that separates the two classes is obtained when the maximum margin is achieved. In this case, we assume that

$$\mathbf{w}^t \mathbf{x}_i + b \geq 1 \quad \forall i \in \{1, \dots, n\} \text{ such that } y_i = 1 \quad (2.7)$$

and

$$\mathbf{w}^t \mathbf{x}_j + b \leq -1 \quad \forall j \in \{1, \dots, n\} \text{ such that } y_j = -1. \quad (2.8)$$

Let \mathcal{H} be the hyperplane that separates the two classes. The hyperplane equation is given by $\mathbf{w}^t \mathbf{x} + b = 0$. Given $\mathbf{x}_0 \in \mathbb{R}^d$, the distance between \mathbf{x}_0 and the hyperplane \mathcal{H} , denoted by $d(\mathbf{x}_0, \mathcal{H})$, is given by

$$d(\mathbf{x}_0, \mathcal{H}) = \frac{|\mathbf{w}^t \mathbf{x}_0 + b|}{\|\mathbf{w}\|}. \quad (2.9)$$

In fact, for any $\mathbf{x} \in \mathcal{H}$, we have $\mathbf{w}^t \mathbf{x} = -b$ and therefore

$$d(\mathbf{x}_0, \mathcal{H}) = \|\text{proj}_{\mathbf{w}}(\mathbf{x}_0 - \mathbf{x})\| = \left\| \frac{(\mathbf{x}_0 - \mathbf{x})^t \mathbf{w}}{\mathbf{w}^t \mathbf{w}} \mathbf{w} \right\| = |(\mathbf{x}_0 - \mathbf{x})^t \mathbf{w}| \frac{\|\mathbf{w}\|}{\|\mathbf{w}\|^2} = \frac{|\mathbf{w}^t \mathbf{x}_0 + b|}{\|\mathbf{w}\|}.$$

Let d_+ be the smallest distance between the separating hyperplane \mathcal{H} and the points of the positive class. Similarly, let d_- be the smallest distance between the hyperplane \mathcal{H} and the

points of the negative class. We can define the geometric margin of a separating hyperplane to be $d_+ + d_-$.

As in our context there are always support vectors \mathbf{x}_j and \mathbf{x}_k of the training set T that satisfy the equality in (2.7) and in (2.8), respectively. Precisely, we have

$$d(\mathbf{x}_j, \mathcal{H}) = d_+ = \frac{|\mathbf{w}^t \mathbf{x}_j + b|}{\|\mathbf{w}\|} = \frac{1}{\|\mathbf{w}\|}$$

and

$$d(\mathbf{x}_k, \mathcal{H}) = d_- = \frac{|\mathbf{w}^t \mathbf{x}_k + b|}{\|\mathbf{w}\|} = \frac{|-1|}{\|\mathbf{w}\|}.$$

Therefore, the margin is $d_+ + d_- = \frac{2}{\|\mathbf{w}\|}$.

Thus, the desired hyperplane is obtained by finding \mathbf{w} and b that solves the following optimization problem

$$\begin{cases} \text{maximize}_{\mathbf{w}, b} & \frac{2}{\|\mathbf{w}\|} \\ \text{subject to} & y_i (\mathbf{w}^t \mathbf{x}_i + b) \geq 1, \forall i \in \{1, 2, \dots, n\}. \end{cases} \quad (2.10)$$

Also, note that maximizing the objective function $\frac{2}{\|\mathbf{w}\|}$ is the same as minimizing the function $\frac{\|\mathbf{w}\|}{2}$. Furthermore, it is the same that minimizes $\frac{1}{2}\|\mathbf{w}\|^2$, which is more convenient to solve as it is a quadratic convex function subject to linear constraints.

Therefore, problem (2.10) is equivalent to solving the following convex optimization problem that is called the primal SVM problem:

$$\begin{cases} \text{minimize}_{\mathbf{w}, b} & \frac{1}{2}\|\mathbf{w}\|^2 \\ \text{subject to} & y_i (\mathbf{w}^t \mathbf{x}_i + b) \geq 1, \forall i \in \{1, 2, \dots, n\}. \end{cases} \quad (2.11)$$

To solve optimization problems with constraints like (2.11), mathematicians have developed various methods. The first optimality conditions for such problems were established by John (1948), followed by Kuhn & Tucker (1951). It was later discovered that the Kuhn-Tucker conditions had already been established by W. Karush in 1939 in his master's thesis, but this thesis was never published, although essential parts were reproduced by Kuhn (1976). Thus, the Kuhn-Tucker conditions came to be known as the Karush-Kuhn-Tucker (KKT) conditions.

The KKT conditions provide necessary conditions for the solution of the optimization problem with inequality constraints. In the case of the SVM problem (2.11), we can apply the KKT conditions to obtain the optimal values of the Lagrange multipliers. These optimal values allow us to determine the optimal values of the decision variables, including the separating hyperplane and the support vectors. By using the Lagrangian formulation and the KKT conditions,

we can solve the SVM problem in a computationally efficient way, even in the nonlinear case (Theodoridis & Koutroumbas, 2006).

The Lagrangian is obtained by

$$\mathcal{L}(\mathbf{w}, b, \lambda) = \frac{1}{2} \|\mathbf{w}\|^2 - \sum_{i=1}^n \lambda_i y_i (\mathbf{w}^t \mathbf{x}_i + b) + \sum_{i=1}^n \lambda_i, \quad (2.12)$$

where λ_i are called Lagrange multipliers. Additionally, the Lagrange multipliers are non-negative due to the KKT conditions (Bazaraa *et al.*, 2006; Fletcher, 1987; Bertsekas, 1995; Nash & Sofer, 1996).

Thus,

$$\begin{cases} \frac{\partial \mathcal{L}}{\partial \mathbf{w}} = \mathbf{w} - \sum_{i=1}^n \lambda_i y_i \mathbf{x}_i = 0 & \iff \mathbf{w} = \sum_{i=1}^n \lambda_i y_i \mathbf{x}_i, \\ \frac{\partial \mathcal{L}}{\partial b} = - \sum_{i=1}^n \lambda_i y_i = 0 & \iff \sum_{i=1}^n \lambda_i y_i = 0. \end{cases} \quad (2.13)$$

Putting (2.13) into (2.12), we have

$$\mathcal{L}(\lambda) = \sum_{i=1}^n \lambda_i - \frac{1}{2} \sum_{i=1}^n \sum_{j=1}^n \lambda_i \lambda_j y_i y_j \mathbf{x}_i^t \mathbf{x}_j. \quad (2.14)$$

It is possible to work with the dual problem because the optimization problem satisfies the conditions for strong duality, which implies that the optimal solutions of the primal and dual problems are equal. Additionally, solving the dual problem can lead to a simpler optimization problem with a smaller number of variables than the primal problem (Luenberger, 1984; Theodoridis & Koutroumbas, 2006).

The dual problem for SVM is reduced to

$$\begin{cases} \text{maximize}_{\lambda} & \sum_{i=1}^n \lambda_i - \frac{1}{2} \sum_{i=1}^n \sum_{j=1}^n \lambda_i \lambda_j y_i y_j \mathbf{x}_i^t \mathbf{x}_j \\ \text{subject to} & \sum_{i=1}^n \lambda_i y_i = 0, \\ & \lambda_i \geq 0, \forall i \in \{1, 2, \dots, n\}. \end{cases} \quad (2.15)$$

Due to dual form (2.15) we can express the original linear model as

$$h(\mathbf{x}) = \mathbf{w}^t \mathbf{x} + b = \sum_{i=1}^n \lambda_i y_i \mathbf{x}_i^t \mathbf{x} + b, \quad (2.16)$$

where λ_i are the Lagrangian coefficients. In other words, we can write (2.16) as a sum of Lagrangian coefficients multiplied by the inner product of the training points and the input vector.

Note that the linear model function in (2.16) was derived for a linearly separable training set T . However, in practice, it is possible that the training set is not linearly separable. In such cases, we can modify the SVM formulation introducing slack variables ξ_i that allow the constraint $y_i(\mathbf{w}^T \mathbf{x}_i + b) \geq 1$ in (2.11) to be relaxed to $y_i(\mathbf{w}^T \mathbf{x}_i + b) \geq 1 - \xi_i$. The objective function can then be modified to penalize the number and magnitude of the slack variables. This allows getting the following optimization problem

$$\begin{cases} \text{minimize}_{\mathbf{w}, v, \xi} & \frac{1}{2} \|\mathbf{w}\|^2 + C \sum_{i=1}^n \xi_i \\ \text{subject to} & y_i(\mathbf{w}^T \mathbf{x}_i + b) \geq 1 - \xi_i, \quad \forall i \in \{1, 2, \dots, n\}, \\ & \xi_i \geq 0, \quad \forall i \in \{1, 2, \dots, n\}, \end{cases} \quad (2.17)$$

where $C \geq 0$ is a hyperparameter that balances the trade-off between the size of the margin and the number of misclassifications (Haykin, 2009). Increasing C results in a smaller margin and fewer misclassifications, while decreasing C results in a larger margin but more misclassifications.

As (2.17) is a convex programming problem like (2.11), the same approach used previously can be employed to solve it. Thus, the Lagrangian is

$$\mathcal{L}(\mathbf{w}, b, \xi, \lambda, \mu) = \frac{1}{2} \|\mathbf{w}\|^2 + C \sum_{i=1}^n \xi_i - \sum_{i=1}^n \lambda_i (y_i(\mathbf{w}^T \mathbf{x}_i + b) - 1 + \xi_i) - \sum_{i=1}^n \mu_i \xi_i, \quad (2.18)$$

with $\lambda_i, \mu_i \geq 0$, for all $i \in \{1, 2, \dots, n\}$.

Then, we have

$$\begin{cases} \frac{\partial \mathcal{L}}{\partial \mathbf{w}} = \mathbf{w} - \sum_{i=1}^n \lambda_i y_i \mathbf{x}_i = 0 & \iff \mathbf{w} = \sum_{i=1}^n \lambda_i y_i \mathbf{x}_i, \\ \frac{\partial \mathcal{L}}{\partial b} = - \sum_{i=1}^n \lambda_i y_i = 0 & \iff \sum_{i=1}^n \lambda_i y_i = 0, \\ \frac{\partial \mathcal{L}}{\partial \xi_i} = C - \lambda_i - \mu_i = 0 & \iff \mu_i = C - \lambda_i, \forall i \in \{1, \dots, n\}. \end{cases} \quad (2.19)$$

Putting (2.19) into (2.18), we have

$$\begin{aligned} \mathcal{L}(\lambda) &= \frac{1}{2} \left(\sum_{i=1}^n \lambda_i y_i \mathbf{x}_i \right)^t \left(\sum_{i=1}^n \lambda_i y_i \mathbf{x}_i \right) + C \sum_{i=1}^n \xi_i - \sum_{i=1}^n \lambda_i y_i \left(\sum_{i=1}^n \lambda_i y_i \mathbf{x}_i \right)^t \mathbf{x}_i \\ &\quad - \sum_{i=1}^n \lambda_i y_i b + \sum_{i=1}^n \lambda_i - \sum_{i=1}^n \lambda_i \xi_i - \sum_{i=1}^n (C - \lambda_i) \xi_i \\ &= \frac{1}{2} \sum_{i=1}^n \sum_{j=1}^n \lambda_i \lambda_j y_i y_j \mathbf{x}_i^t \mathbf{x}_j + C \sum_{i=1}^n \xi_i - \sum_{i=1}^n \sum_{j=1}^n \lambda_i \lambda_j y_i y_j \mathbf{x}_i^t \mathbf{x}_j \\ &\quad - \left(\sum_{i=1}^n \lambda_i y_i \right) b + \sum_{i=1}^n \lambda_i - \sum_{i=1}^n \lambda_i \xi_i - \sum_{i=1}^n C \xi_i + \sum_{i=1}^n \lambda_i \xi_i \\ &= \sum_{i=1}^n \lambda_i - \frac{1}{2} \sum_{i=1}^n \sum_{j=1}^n \lambda_i \lambda_j y_i y_j \mathbf{x}_i^t \mathbf{x}_j. \end{aligned} \quad (2.20)$$

Notice that (2.20) is identical to (2.14) and it means that we can use a quadratic programming solver to solve the dual problem form. The dual problem for linear SVM in nonseparable cases is reduced to

$$\left\{ \begin{array}{l} \text{maximize}_{\lambda} \quad \sum_{i=1}^n \lambda_i - \frac{1}{2} \sum_{i=1}^n \sum_{j=1}^n \lambda_i \lambda_j y_i y_j \mathbf{x}_i^t \mathbf{x}_j \\ \text{subject to} \quad \sum_{i=1}^n \lambda_i y_i = 0, \\ \quad \quad \quad 0 \leq \lambda_i \leq C, \quad \forall i \in \{1, 2, \dots, n\}. \end{array} \right. \quad (2.21)$$

Therefore, the SVM classifier in both cases can be represented by (2.16). It is important to note that the solution is performed with the inner products $\mathbf{x}^t \mathbf{x}_i$ from the training set T . This property allowed Vladimir Vapnik to extend the SVM formulation by creating nonlinear classifiers in the original space through the use of nonlinear functions, which are known as kernel functions (Vapnik, 1998, 1999). This results in the model $h(\mathbf{x}) = \sum_{i=1}^n \lambda_i y_i \mathbf{K}(\mathbf{x}, \mathbf{x}_i) + b$, where \mathbf{K} is a kernel function.

Common Kernel Functions	
Gaussian RBF	$\mathbf{K}(\mathbf{x}, \mathbf{y}) = \exp\left(\frac{-\ \mathbf{x} - \mathbf{y}\ ^2}{k}\right)$
Sigmoidal	$\mathbf{K}(\mathbf{x}, \mathbf{y}) = \tanh(\alpha \langle \mathbf{x}, \mathbf{y} \rangle + b)$
Polynomial	$\mathbf{K}(\mathbf{x}, \mathbf{y}) = (\langle \mathbf{x}, \mathbf{y} \rangle + b)^n$
Inverse multiquadric	$\mathbf{K}(\mathbf{x}, \mathbf{y}) = \frac{1}{\sqrt{\ \mathbf{x} - \mathbf{y}\ ^2 + k^2}}$

Table 2.1 – Gaussian radial basis function (RBF) kernel with $k \in \mathbb{R}$, sigmoidal kernel with $\alpha, b \in \mathbb{R}$, polynomial kernel with $n \in \mathbb{N}, b \in \mathbb{R}$, and inverse multiquadric kernel with $k \in \mathbb{R}_+$ (Müller *et al.*, 2001).

Examples of common kernel functions are presented in Table 2.1.

Thus, we can use the Lagrangian dual formulation of the SVM using nonlinear functions to develop the supervised h_{SVM} order.

Precisely, let $F = \{\mathbf{f}_1, \mathbf{f}_2, \dots, \mathbf{f}_N\} \subset \mathbb{V}$ be a foreground value set and let $B = \{\mathbf{b}_1, \mathbf{b}_2, \dots, \mathbf{b}_M\} \subset \mathbb{V}$ be a background value set such that $B \cap F = \emptyset$. Our goal is to separate the values in F from those in B by assigning class labels $+1$ and -1 , respectively. To accomplish this, we define the labeled training set T as

$$T = \left(\bigcup_{i=1}^N \{(\mathbf{f}_i, +1)\} \right) \cup \left(\bigcup_{j=1}^M \{(\mathbf{b}_j, -1)\} \right) \subset \mathbb{V} \times \{1, -1\}. \quad (2.22)$$

In the same way that we obtained the equations (2.14) and (2.20), we have

$$\begin{aligned} \mathcal{L}(\lambda, \mu) &= \sum_{i=1}^N \lambda_i + \sum_{j=1}^M \mu_j - \frac{1}{2} \left(\sum_{i=1}^N \lambda_i \left(\sum_{\ell=1}^N \lambda_\ell \mathbf{f}_i^t \mathbf{f}_\ell \right) \right. \\ &\quad \left. + \sum_{j=1}^M \mu_j \left(\sum_{k=1}^M \mu_k \mathbf{b}_j^t \mathbf{b}_k \right) - \sum_{i=1}^N \lambda_i \left(\sum_{j=1}^M \mu_j \mathbf{f}_i^t \mathbf{b}_j \right) - \sum_{j=1}^M \mu_j \left(\sum_{i=1}^N \lambda_i \mathbf{b}_j^t \mathbf{f}_i \right) \right) \\ &= \sum_{i=1}^N \lambda_i + \sum_{j=1}^M \mu_j - \frac{1}{2} \left(\sum_{i=1}^N \sum_{\ell=1}^N \lambda_i \lambda_\ell \mathbf{f}_i^t \mathbf{f}_\ell + \sum_{j=1}^M \sum_{k=1}^M \mu_j \mu_k \mathbf{b}_j^t \mathbf{b}_k - 2 \sum_{i=1}^N \sum_{j=1}^M \lambda_i \mu_j \mathbf{f}_i^t \mathbf{b}_j \right). \end{aligned}$$

Therefore, the dual problem is identical to problem (2.21) and is given by

$$\left\{ \begin{array}{l} \underset{\lambda, \mu}{\text{maximize}} \quad \sum_{i=1}^N \lambda_i + \sum_{j=1}^M \mu_j - \frac{1}{2} \sum_{i=1}^N \sum_{\ell=1}^N \lambda_i \lambda_\ell \mathbf{K}(\mathbf{f}_i, \mathbf{f}_\ell) - \frac{1}{2} \sum_{j=1}^M \sum_{k=1}^M \mu_j \mu_k \mathbf{K}(\mathbf{b}_j, \mathbf{b}_k) \\ \quad + \sum_{i=1}^N \sum_{j=1}^M \lambda_i \mu_j \mathbf{K}(\mathbf{f}_i, \mathbf{b}_j) \\ \text{subject to} \quad \sum_{i=1}^N \lambda_i - \sum_{j=1}^M \mu_j = 0, \\ \quad 0 \leq \lambda_i, \mu_j \leq C, \quad \forall i \in \{1, 2, \dots, n\} \quad \forall j \in \{1, 2, \dots, m\}, \end{array} \right. \quad (2.23)$$

where C is a user-specified positive parameter that controls the tradeoff between the complexity of the machine and the number of nonseparable values, and \mathbf{K} is the kernel function $\mathbf{K} : \mathbb{V} \times \mathbb{V} \rightarrow \mathbb{R}$, which is given by $\mathbf{K}(\mathbf{x}, \mathbf{y}) = \langle \Phi(\mathbf{x}), \Phi(\mathbf{y}) \rangle$, where $\Phi : \mathbb{V} \rightarrow \mathcal{F}$ is a nonlinear mapping of \mathbb{V} into a potentially much higher dimensional feature space \mathcal{F} (Müller *et al.*, 2001).

Finally, omitting b because it is constant for all \mathbf{x} , our h -ordering based on SVM $h_{SVM} : \mathbb{V} \rightarrow \overline{\mathbb{R}}$ is obtained by

$$h_{SVM}(\mathbf{x}) = \sum_{\mathbf{f} \in F} \lambda_i \mathbf{K}(\mathbf{x}, \mathbf{f}) - \sum_{\mathbf{b} \in B} \mu_j \mathbf{K}(\mathbf{x}, \mathbf{b}), \quad \text{for all } \mathbf{x} \in \mathbb{V}, \quad (2.24)$$

where $\lambda_1, \dots, \lambda_N$ and μ_1, \dots, μ_M solve the quadratic optimization problem (2.23).

Figure 2.3 shows the image \mathbf{I} from Figure 2.1, the dilated image obtained by h -ordering (2.24) using the kernel Gaussian RBF, and the eroded image obtained by h -ordering (2.24) using the kernel Gaussian RBF.

The structuring element S is a 9×9 square. For dilation and erosion, we use for the background set the colors near the edge of the image and for the foreground set the colors in the center of the image. Precisely, we consider the central pixel of the image and four pixels in the corners of the image, i.e., one pixel in the upper left, one pixel in the upper right, another pixel in the lower left, and the last one pixel in the lower right. Then, segment the image segmentation, using the central pixel as a seed for the foreground set and the other four pixels near the edge as seeds for the background set. With the image segmentation performed, we consider 20 color values for our training set, being 10 colors for the foreground set and 10 colors

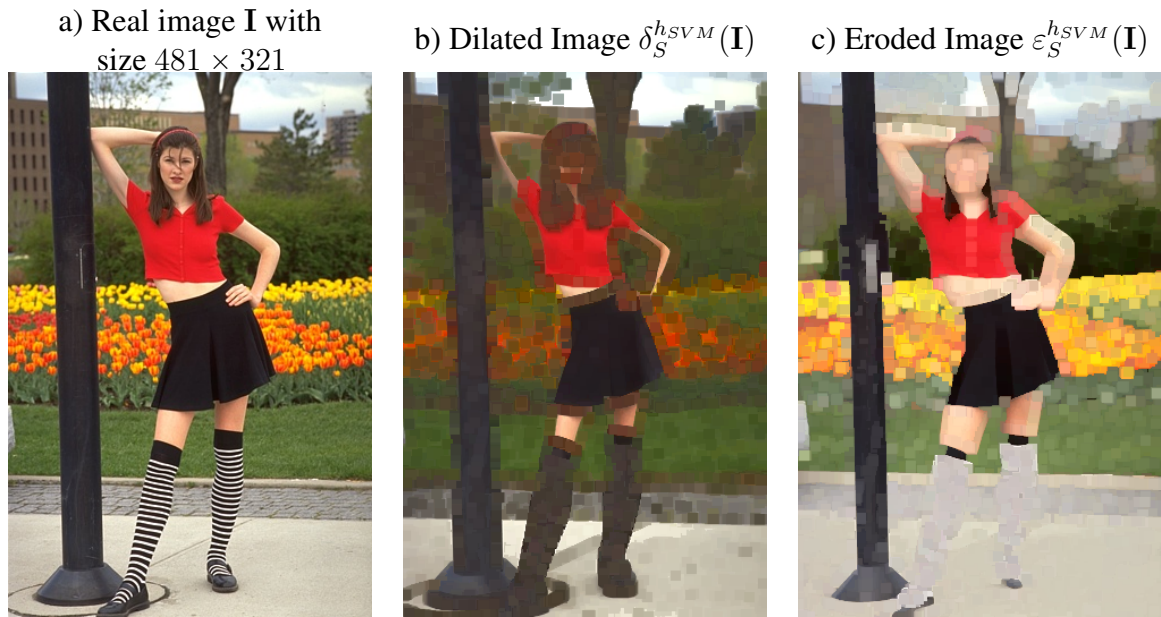


Figure 2.3 – Illustrative example of images obtained by h -ordering based on SVM. Figure a) shows the color image \mathbf{I} given in Figure 2.1. Figure b) shows the dilated image using (2.24) and Figure c) shows the eroded image using (2.24).



Figure 2.4 – Color palette used in the SVM approach.

for the background set. Figure 2.4 shows the color palettes of the foreground and background sets. Note that foreground colors are colors close to the center like green, black, and red colors. Additionally, notice that the background colors are close to the corners of the edges like light blue, gray, and white. Finally, notice that in the dilated image, we have obtained black socks since our foreground set had black colors. In the case of the eroded image, the socks of the woman turned white since our background set has colors close to the edge and consequently close to white.

2.3.2 Unsupervised Morphological Approach Based on Statistical Projection Depth

An unsupervised morphological approach involves the utilization of morphological operations on the raw data set, without any labeled data or prior information provided to the algorithm regarding the extraction of features or classification of the data. In this way, a set of unlabelled values is used to establish the mapping $h : \mathbb{V} \rightarrow \mathbb{L}$. The h -unsupervised ordering can be obtained by using the more representative projection in a statistical dimension

reduction technique. For instance, a linear approach such as principal component analysis (PCA) (Jolliffe, 2010), local principal component analysis (Local-PCA) (Kambhatla & Leen, 1997), or some nonlinear projections approach (Lézoray *et al.*, 2009). For our computational comparison proposals, we consider the unsupervised approach based on the statistical projection depth function (Donoho & Gasko, 1992; Velasco-Forero & Angulo, 2012).

According to Zuo & Serfling (2000), the development of statistical depth functions for multivariate data has been a focus in nonparametric data analysis and robust inference. The objective of a depth function is to offer a nonparametric and robust measure of the centrality of a point within a multivariate dataset. For a distribution \mathbf{P} in \mathbb{R}^d , a corresponding statistical depth function is any function $D(\mathbf{x}, \mathbf{P})$ that provides a \mathbf{P} -based center-outward ordering of points $\mathbf{x} \in \mathbb{R}^d$.

Formally, we have the following definition.

Definition 2.19 (Statistical depth function). Let \mathcal{F} be the class of distributions on the Borel sets of \mathbb{R}^d and let $F_{\mathbf{x}}$ be the distribution of a given random vector \mathbf{x} . A statistical depth function is a bounded, nonnegative mapping $D(\cdot; \cdot) : \mathbb{R}^d \times \mathcal{F} \rightarrow \mathbb{R}$ satisfying the following properties:

1. $D(\mathbf{A}\mathbf{x} + \mathbf{b}; F_{\mathbf{A}\mathbf{x} + \mathbf{b}}) = D(\mathbf{x}; F_{\mathbf{x}})$ for all $d \times d$ nonsingular matrix \mathbf{A} and all $\mathbf{x}, \mathbf{b} \in \mathbb{R}^d$.
(affine invariance)
2. $D(\theta; F) = \sup_{\mathbf{x} \in \mathbb{R}^d} D(\mathbf{x}; F)$ for all $F \in \mathcal{F}$ and $\theta \in \mathbb{R}^d$. (maximality at center)
3. $D(\mathbf{x}; F) \leq D(\theta + \alpha(\mathbf{x} - \theta); F)$ for all $F \in \mathcal{F}$, $\theta \in \mathbb{R}^d$, and $\alpha \in [0, 1]$. (monotonicity relative to deepest point)
4. $D(\mathbf{x}; F) \rightarrow 0$ as $\|\mathbf{x}\| \rightarrow \infty$, for each $F \in \mathcal{F}$. (vanishing at infinity)

We can say that invariance to affine transformation means that the depth of a point $\mathbf{x} \in \mathbb{R}^d$ should not depend on the underlying coordinate system or, in particular, on the scales of the underlying measurements. The maximality at center means that for a distribution having a uniquely defined “center”, the depth function should attain maximum value at this center. The monotonicity relative to deepest point means that a point $\mathbf{x} \in \mathbb{R}^d$ moves away from the “deepest point” along any fixed ray through the center, the depth at \mathbf{x} should decrease monotonically and the vanishing at infinity means that the depth of a point \mathbf{x} should approach zero as $\|\mathbf{x}\|$ approaches infinity (Zuo & Serfling, 2000).

In the sequel, we will define the projection depth function.

Definition 2.20 (Projection depth function). Let $\mathbf{X} = [\mathbf{x}_1, \dots, \mathbf{x}_n] \in \mathbb{R}^{d \times n}$ be a training sample. The projection depth function $h_{\mathcal{P}}^* : \mathbb{R}^d \rightarrow \mathbb{R}$ is defined by

$$h_{\mathcal{P}}^*(\mathbf{x}) = \sup_{\mathbf{u} \in \mathbb{S}^{d-1}} \frac{|\mathbf{u}^T \mathbf{x} - \text{MED}(\mathbf{u}^T \mathbf{X})|}{\text{MAD}(\mathbf{u}^T \mathbf{X})}, \quad \forall \mathbf{x} \in \mathbb{R}^d, \quad (2.25)$$

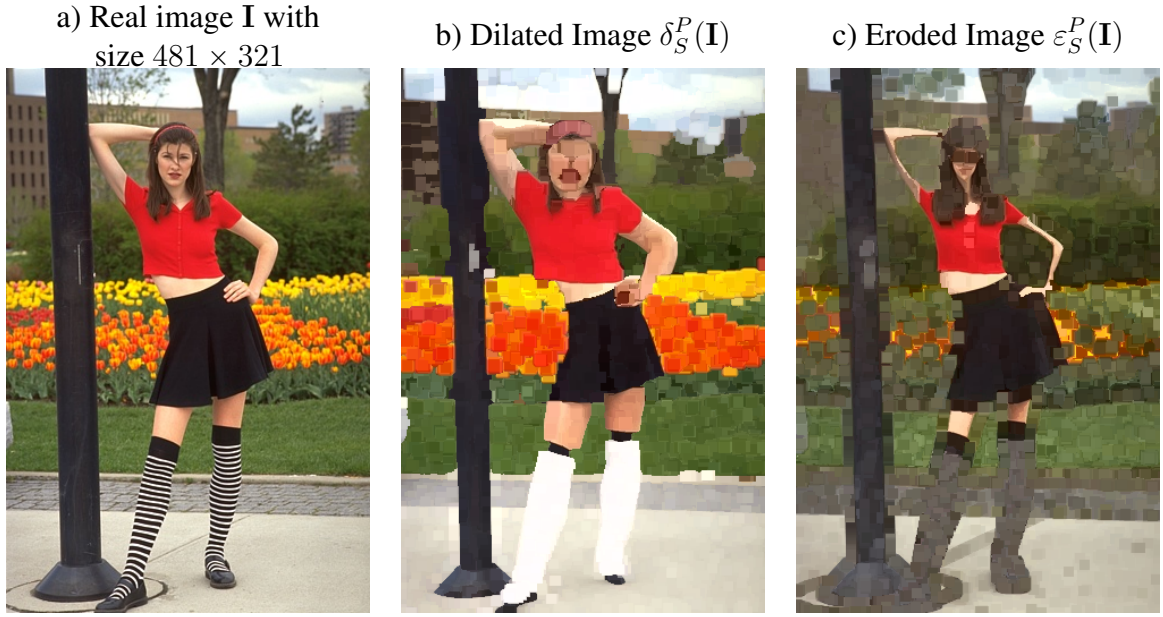


Figure 2.5 – Illustrative example of images obtained by h -ordering based on the projection depth function. Figure a) shows the color image \mathbf{I} given in Figure 2.1. Figure b) shows the dilated image using (2.27) and Figure c) shows the eroded image using (2.27).

where $\mathbb{S}^{d-1} = \{\mathbf{x} \in \mathbb{R}^d : \|\mathbf{x}\|_2 = 1\}$ is the d -dimensional hypersphere, $\text{MED} : \mathbb{R}^n \rightarrow \mathbb{R}$ is the median operator, and $\text{MAD} : \mathbb{R}^n \rightarrow \mathbb{R}$ is the median absolute deviation from the median operator.

Remark 2.9. The median absolute deviation from the median is given by

$$\text{MAD}(\mathbf{t}) = \text{MED}(|\mathbf{t} - \mathbf{1}_n \text{MED}(\mathbf{t})|), \quad (2.26)$$

where $\mathbf{1}_n \in \mathbb{R}^n$ denotes the vector of ones and the absolute value $|\cdot|$ is computed in a component-wise manner.

Actually, it is infeasible to compute h_P^* as it necessitates the examination of an infinite number of random projections. Thus, we approximate the depth projection function by replacing the supremum with the maximum on a finite set of elements in the hypersphere \mathbb{S}^{d-1} . Specifically, we estimate an approximate value of h_P^* by utilizing k random projections uniformly distributed in \mathbb{S}^{d-1} (Velasco-Forero & Angulo, 2012).

Therefore, the function $h_P : \mathbb{R}^d \rightarrow \mathbb{R}$ is given by

$$h_P(\mathbf{x}) = \max_{\mathbf{u} \in \mathbb{U}} \frac{|\mathbf{u}^T \mathbf{x} - \text{MED}(\mathbf{u}^T \mathbf{X})|}{\text{MAD}(\mathbf{u}^T \mathbf{X})}, \quad \forall \mathbf{x} \in \mathbb{R}^d, \quad (2.27)$$

where $\mathbb{U} = \{\mathbf{u}_1, \mathbf{u}_2, \dots, \mathbf{u}_k\} \subset \mathbb{S}^{d-1}$, where $\mathbf{u}_i \in \mathbb{R}^d$ and for each $i = 1, 2, \dots, k$, \mathbf{u}_i is a random vector that is distributed uniformly on the surface of the d -dimensional hypersphere of radius 1. In this case, h_P is an approximation of the theoretical depth projection function h_P^*

Finally, the projection depth morphological approach is defined by ranking the vector-values according to the h -ordering $h_P : \mathbb{V} \subset \mathbb{R}^d \rightarrow \mathbb{L} \subset \mathbb{R}$ given by (2.27) together with a lookup table.

Figure 2.5 shows the image \mathbf{I} from Figure 2.1, the dilated image, and the eroded image obtained by h -ordering h_P in (2.27). For both cases, we consider the parameter $k = 1000$. The choice of this parameter is regarding due to the stability in the value of h -ordering (2.27) for certain given images (Velasco-Forero & Angulo, 2012).

In Figure 2.5, we perceive that the dilated image $\delta_S^P(\mathbf{I})$ and eroded image $\varepsilon_S^P(\mathbf{I})$ exhibit significant irregularity, as anticipated. This observation aligns with our expectations, as expounded upon in Chapter 1 of this thesis, wherein it is noted that the projection depth order has a propensity to generate anomalies.

2.3.3 Loewner Order and its Corresponding Morphological Approach

In addition to the marginal approach, this thesis also examines a second multivariate morphological approach that is based on partial ordering. Specifically, the approach of color-morphology using the Loewner order, as proposed by Burgeth & Kleefeld (2014), is considered. The Loewner order has been demonstrated to be effective in the development of morphological techniques that utilize multivariate data, as referenced in Burgeth *et al.* (2019).

The Loewner order is a useful tool for multivariate morphological approach and image processing. It is a partial order defined on the set of symmetric matrices. The Loewner partial ordering compares two symmetric matrices \mathbf{A} and \mathbf{B} by determining if there exists a positive semidefinite matrix \mathbf{K} such that $\mathbf{K} = \mathbf{B} - \mathbf{A}$. If that is the case, we have $\mathbf{A} \leq_W \mathbf{B}$. In mathematical terms, we have the following definition

Definition 2.21 (Loewner order). Let \mathbf{A} and \mathbf{B} be symmetric matrices. The Loewner order is defined by

$$\mathbf{A} \leq_W \mathbf{B} \iff \mathbf{B} - \mathbf{A} \text{ is positive semidefinite.} \quad (2.28)$$

Remark 2.10. The Loewner order is not a total order. This can be demonstrated by considering the symmetric matrices $\mathbf{A} = \begin{pmatrix} 1 & 0 \\ 0 & 0 \end{pmatrix}$ and $\mathbf{B} = \begin{pmatrix} 0 & 0 \\ 0 & 1 \end{pmatrix}$. It can be observed that neither $\mathbf{A} \leq_W \mathbf{B}$ nor $\mathbf{B} \leq_W \mathbf{A}$ holds true. To further illustrate this, let $\mathbf{x} = \begin{pmatrix} a \\ b \end{pmatrix} \in \mathbb{R}^2$ be a vector. It can be seen that $\mathbf{x}^T(\mathbf{B} - \mathbf{A})\mathbf{x} = b^2 - a^2$. Taking $a = 2$ and $b = 1$, we have $\mathbf{x}^T(\mathbf{B} - \mathbf{A})\mathbf{x} < 0$. Similarly, for $a = 1$ and $b = 2$, we have $\mathbf{x}^T(\mathbf{A} - \mathbf{B})\mathbf{x} < 0$, thus further emphasizing that Loewner order is not a total order.

We consider a symmetric matrix field F as a mapping $F : \mathbb{V} \subset \mathbb{R}^d \rightarrow \text{Sym}(n)$ from a domain $\mathbb{V} \subset \mathbb{R}^d$ into the space $\text{Sym}(n)$ of real symmetric $n \times n$ -matrices with inner product

$\langle \mathbf{A}, \mathbf{B} \rangle = \text{trace}(\mathbf{A}\mathbf{B})$ and Frobenius-norm $\|\mathbf{A}\| = \sqrt{\langle \mathbf{A}, \mathbf{A} \rangle}$.

We now discuss the conversion between a color image \mathbf{I} and a matrix field F based on [Burgeth & Kleefeld \(2014\)](#).

First, we convert the RGB color space \mathcal{C}_{RGB} to the HSL color space \mathcal{C}_{HSL} . After that, we replace the saturation of HSL color space \mathcal{C}_{HSL} by the chroma c , which is computed by $c = \max\{r, g, b\} - \min\{r, g, b\}$, and modify the luminance l in the HSL color space by $\tilde{l} = 2l - 1$.

In total, we transform the RGB color space \mathcal{C}_{RGB} into a variant space of HSL color space \mathcal{C}_{HSL} that is called m -HCL color space, denoted by \mathcal{C}_{m-HSL} as we have seen in Section 2.3. The geometric representation of \mathcal{C}_{m-HSL} is a cone with two tips, centered at the point $(0, 0, 0)$, with its vertices at $(0, 0, 1)$ and $(0, 0, -1)$ and a circular base of radius one intersecting the origin and parallel to the xy -plane. The geometric representation is depicted in Figure 2.6.

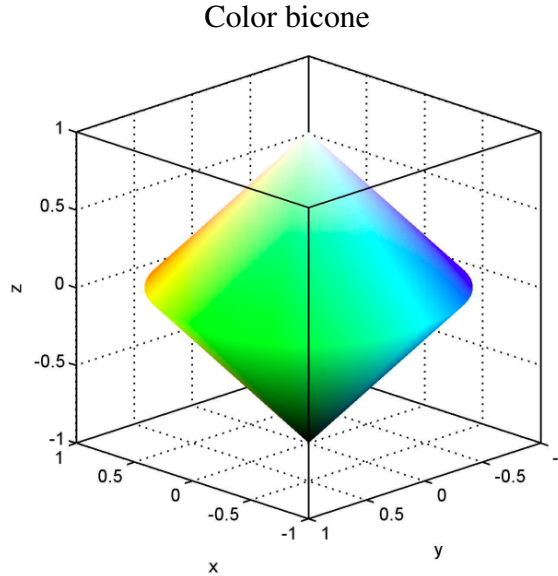


Figure 2.6 – Bicone for the m -HCL color space. Source: [Burgeth & Kleefeld \(2013\)](#).

Precisely, the coordinates of an arbitrary point $\mathbf{x} \in \mathcal{C}_{m-HSL}$ is $\mathbf{x} = (c \cos(2\pi h), c \sin(2\pi h), \tilde{l})$, which represents the coordinates of hue (h), chroma (c), and luminance (\tilde{l}).

Finally, we consider the following mapping $\Psi : \mathcal{C}_{m-HSL} \rightarrow \text{Sym}(2)$ given by

$$\Psi(c \cos(2\pi h), c \sin(2\pi h), \tilde{l}) = \mathbf{A}, \quad (2.29)$$

where $\mathbf{A} = ([a, b], [b, c]) := \begin{pmatrix} a & b \\ b & c \end{pmatrix}$, with $a = \frac{1}{\sqrt{2}}(\tilde{l} - c \sin(2\pi h))$, $b = \frac{1}{\sqrt{2}}c \cos(2\pi h)$, and $c = \frac{1}{\sqrt{2}}(\tilde{l} + c \sin(2\pi h))$ such that

$$-\frac{1}{\sqrt{2}}\mathbf{I} \leq_W \mathbf{A} \leq_W \frac{1}{\sqrt{2}}\mathbf{I},$$

where \mathbf{I} denotes the identity matrix.

Finally, the isomorphism correspondence between colors and symmetric 2×2 matrices makes possible the definition of the Loewner method for color morphology¹.

It is important to note that in this thesis, we are employing the morphological approach for colored images as proposed by authors [Burgeth & Kleefeld \(2013\)](#). As can be seen, their selection of m-CHL could be altered by another color space, which represents one of the potential avenues for future research as pursued by these authors.

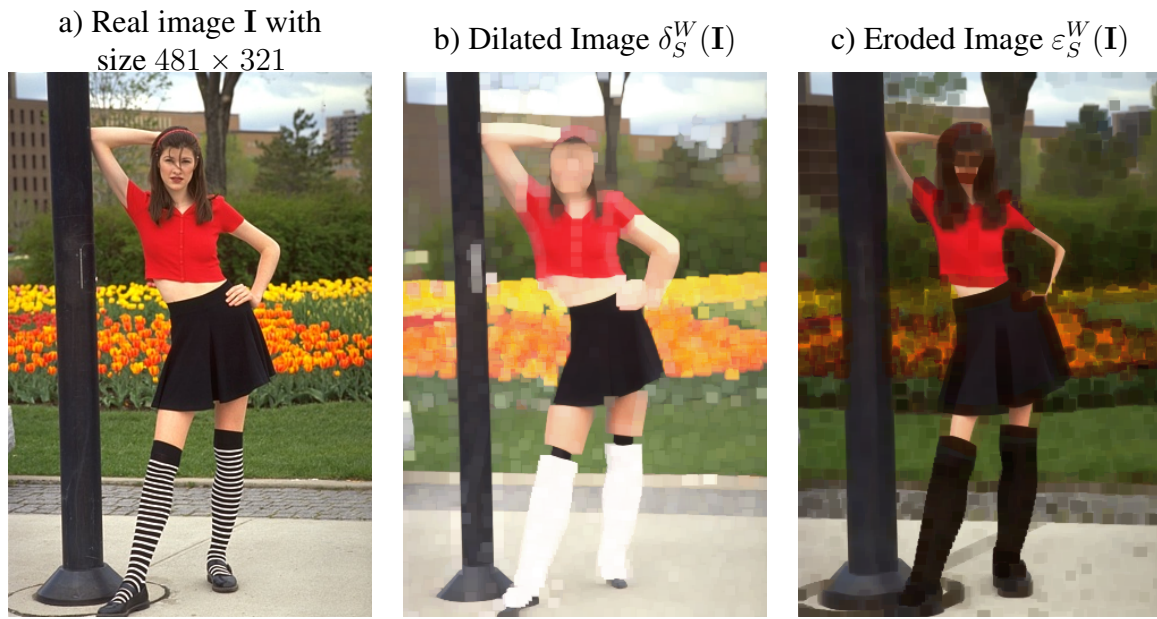


Figure 2.7 – Illustrative example of morphological operators using the Loewner approach. Figure a) shows the color image \mathbf{I} given in figure 2.1. Figure b) shows the dilated image δ_S^W and Figure c) shows the eroded image ε_S^W .

Some examples seen in [Burgeth & Kleefeld \(2014\)](#) are given below.

The color black $(0, 0, 0) \in \mathcal{C}_{RGB}$ is represented by the matrix $-\frac{1}{\sqrt{2}} \begin{pmatrix} 1 & 0 \\ 0 & 1 \end{pmatrix}$ and the color white $(1, 1, 1) \in \mathcal{C}_{RGB}$ is represented by the matrix $\frac{1}{\sqrt{2}} \begin{pmatrix} 1 & 0 \\ 0 & 1 \end{pmatrix}$.

Furthermore, the colors gray, red, green, and blue given respectively by $(0.5, 0.5, 0.5)$, $(1, 0, 0)$, $(0, 1, 0)$, $(0, 0, 1) \in \mathcal{C}_{RGB}$ are represented respectively by the null matrix $\begin{pmatrix} 0 & 0 \\ 0 & 0 \end{pmatrix}$, and

$$\begin{pmatrix} 0 & \frac{1}{\sqrt{2}} \\ \frac{1}{\sqrt{2}} & 0 \end{pmatrix}, \frac{1}{4} \begin{pmatrix} -\sqrt{6} & -\sqrt{2} \\ -\sqrt{2} & \sqrt{6} \end{pmatrix}, \text{ and } \frac{1}{4} \begin{pmatrix} \sqrt{6} & -\sqrt{2} \\ -\sqrt{2} & -\sqrt{6} \end{pmatrix}.$$

¹ The program code of the Loewner morphological approach is located at <https://www.math.tu-cottbus.de/INSTITUT/lsmwr/kleefeld/SourcePRL/>.

In Figure 2.7, we show the dilation and the erosion morphological operators based on the Loewner approach. We used a 9×9 square structuring element S . Observe that the dilated image has a predominance of the white color over the black color and the eroded image has a predominance of the black color over the white color.

2.4 The Challenges of False Colors and the Irregularity Issue

As we discussed in Section 2.3, in mathematical morphology, the concept of order relation is fundamental to the study of multivariate morphological operators. We know that when we have two real-valued functions f and g and take the supremum $f \vee g$ or the infimum $f \wedge g$, the result can be different from the two operands although the result for a fixed and arbitrary point x , we have that the supremum of $(f \vee g)(x)$ and $(f \wedge g)(x)$ is equal to either $f(x)$ or $g(x)$. For multidimensional cases, the situation is even worse. For example, if the functions f and g represent color vector images, and their supremum at point x may be neither $f(x)$ nor $g(x)$, then a false color is generated (Serra, 2009).

To explain in more detail, we already know that the marginal order given by Example 2.3 is defined by

$$\mathbf{x} \leq_M \mathbf{y} \iff x_1 \leq_{\mathbb{R}} y_1, x_2 \leq_{\mathbb{R}} y_2, \dots, \text{ and } x_m \leq_{\mathbb{R}} y_m, \quad (2.30)$$

for vectors $\mathbf{x} = (x_1, x_2, \dots, x_m) \in \mathbb{V}$ and $\mathbf{y} = (y_1, \dots, y_m) \in \mathbb{V}$, where $\leq_{\mathbb{R}}$ denotes the usual ordering in \mathbb{R} . The supremum and infimum operations are computed component-wise using marginal ordering. Precisely, given $\mathbf{X} \subseteq \mathbb{V}$, then

$$\bigvee \mathbf{X} = (\bigvee X_1, \dots, \bigvee X_m) \quad \text{and} \quad \bigwedge \mathbf{X} = (\bigwedge X_1, \dots, \bigwedge X_m). \quad (2.31)$$

Despite its simplicity, the marginal ordering given by (2.30) often leads to false colors (Serra, 2009). For example, consider the RGB color space \mathcal{C}_{RGB} . The marginal order yields

$$\bigvee \{(1, 0, 0), (0, 0, 1)\} = (1, 0, 1) \quad \text{and} \quad \bigwedge \{(1, 0, 0), (0, 0, 1)\} = (0, 0, 0). \quad (2.32)$$

In words, the supremum and the infimum of red and blue are magenta and black, respectively. Therefore, using the marginal ordering, the supremum and infimum operations may result in a color that does not belong to the set, resulting in the so-called false color.

For example, consider the image \mathbf{I} shown in Figure 2.1, and let $\mathbf{I}_1 : D \rightarrow \mathbb{V}$ be a toy image with size 9×9 defined by

$$\begin{cases} \mathbf{I}_1(i, j) = (0, 0, 1) & \text{if } (i, j) \in D \setminus \{(2, 2), (7, 7)\}, \\ \mathbf{I}_1(2, 2) = (1, 0, 0), \\ \mathbf{I}_1(7, 7) = (0, 1, 0). \end{cases}$$

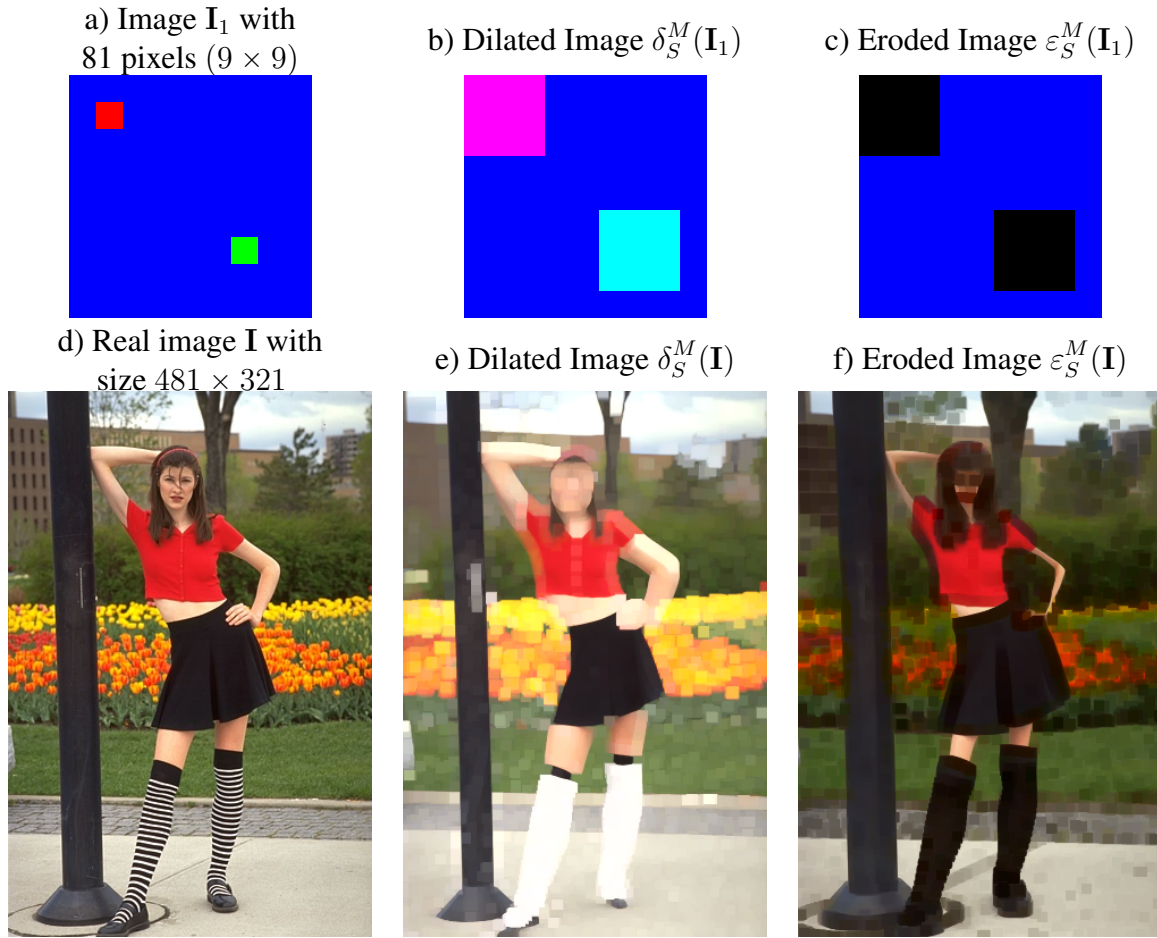


Figure 2.8 – Illustrative example of false colors. Figure a) shows image \mathbf{I}_1 , size 9×9 (81 pixels), with the colors blue, red and green. Figure b) shows the false color black on the dilated image $\delta_S^M(\mathbf{I}_1)$. Figure c) shows the false colors magenta and cyan on the eroded image $\varepsilon_S^M(\mathbf{I}_1)$. Figure d) shows the color image \mathbf{I} . Figure e) shows the dilated image $\delta_S^M(\mathbf{I})$, and Figure f) shows the eroded image $\varepsilon_S^M(\mathbf{I})$.

In Figure 2.8 we show the images \mathbf{I} , \mathbf{I}_1 , and their respective dilation and erosion with the marginal order given in Example 2.3. For toy image \mathbf{I}_1 we calculate the dilation $\delta_S^M(\mathbf{I}_1)$ and the erosion $\varepsilon_S^M(\mathbf{I}_1)$ using a 3×3 square as the structuring element (S). For image \mathbf{I} we calculate the dilation $\delta_S^M(\mathbf{I})$ and the erosion $\varepsilon_S^M(\mathbf{I})$ using a 9×9 square as the structuring element S .

Note that the dilated image $\delta_S^M(\mathbf{I}_1)$ has the false color black, and the eroded image $\varepsilon_S^M(\mathbf{I}_1)$ has the false colors magenta and cyan. The dilated image $\delta_S^M(\mathbf{I})$ has near the right arm of the woman a false color close to orange, and the eroded image $\varepsilon_S^M(\mathbf{I})$ has several false colors such as the boundary of her red shirt that are with a color close to brown.

Therefore, a challenge in multivariate mathematical morphology is the appearance of false values or, more specifically, the “false colors”, as highlighted by Serra (2009). As stated in our paper Valle *et al.* (2021), a morphological operator $\psi : \mathcal{V} \rightarrow \mathcal{V}$ creates false values when there are values in $\psi(\mathbf{I})$ that are not present in the original image \mathbf{I} . To be more formal, let $2^{\mathbb{V}}$ be the power set of \mathbb{V} and let $V : \mathcal{V} \rightarrow 2^{\mathbb{V}}$ be the mapping given by equation

$$V(\mathbf{I}) = \{\mathbf{I}(p) : p \in D\}, \quad \forall \mathbf{I} \in \mathcal{V}. \quad (2.33)$$

A morphological operator ψ introduces false colors if the set difference $V(\psi(\mathbf{I})) \setminus V(\mathbf{I})$ is not empty. Certain applications, such as the manipulation of satellite data or composite data in geographical information systems, can be hampered by the presence of “abnormal false values”.

Utilizing partial orders like the marginal or the Loewner orders, the dilation operator and the erosion operator given by (2.4) often results in false colors. Note in Figure 2.7 that the dilated image δ_S^W has a false color on the shirt of the woman. In the same way, in Figure 2.7, the eroded image ε_S^W has a false color on the hair of the woman.

To circumvent the issue of false values, a total order like the lexicographical order given by Example 2.4 and a reduced ordering with a lookup table can be used. With a total order, the supremum is an element of the set, which is equivalent to the maximum operation. Similarly, the infimum of a finite set is an element of the set, which is identical to the minimum operation. As a result, when D is finite, the elementary morphological operators given by (2.4) will only contain values of the input image \mathbf{I} .

According to Chevallier & Angulo (2016), a disadvantage of using a total order is that it might not be regular in a metric space. This means that the topology induced by a total order might not be consistent with the topology of a metric space. In another words, if $\mathbf{I} : D \rightarrow \mathcal{C}_{RGB}$ is a color image and \mathbf{J} is a morphological image obtained by a morphological operator applied on \mathbf{I} using a total order, then the challenges of false color appearance will be avoided, but unfortunately we will have the challenge to deal with small aliasing that might appear in the image \mathbf{J} . In this context, these aliasing are called irregularity challenges, or irregularity issue or simply as irregularity.

Precisely, Chevallier & Angulo (2016) demonstrated the following theorem:

Theorem 2.1. Let (X, d) be a metric space endowed with a total order \leq . Suppose there are three points $x, y, z \in X$ and a positive real number R such that $d(x, y) > R$, $d(x, z) > R$, $d(y, z) > R$ and that the complement $B^C(x, R)$, $B^C(y, R)$, $B^C(z, R)$ of each ball $B(x, R)$, $B(y, R)$, $B(z, R)$ is connected. Then, for all $r > 0$, there exist three points $a, b, c \in X$ such that

$$\begin{cases} a \leq b \leq c, \\ d(a, b) \geq R, \\ d(a, c) \leq r. \end{cases} \quad (2.34)$$

Particularly, let \mathbb{V} be a metric space endowed with a total order and a metric $d : \mathbb{V} \times \mathbb{V} \rightarrow [0, +\infty)$. Chevallier & Angulo (2016) proved that under mild conditions regarding the connectivity of \mathbb{V} , there exist $\mathbf{u}, \mathbf{v}, \mathbf{w} \in \mathbb{V}$ such that $\mathbf{u} \leq \mathbf{v} \leq \mathbf{w}$, but the distance between \mathbf{u} and \mathbf{w} is less than or equal to the distance between \mathbf{u} and \mathbf{v} . This suggests that despite \mathbf{u} being closer to \mathbf{w} than to \mathbf{v} , the inequalities $\mathbf{u} \leq \mathbf{v} \leq \mathbf{w}$ imply that \mathbf{u} is farther from \mathbf{w} than \mathbf{v} . It should be

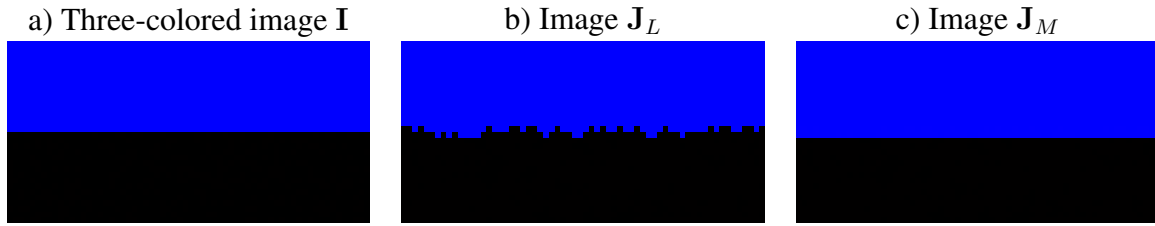


Figure 2.9 – Figure a) shows image \mathbf{I} consisting of three colors: pure black, black and pure blue. Figure b) shows the dilated image \mathbf{J}_L using lexicographic order. Figure c) shows the dilated image \mathbf{J}_M using marginal order.

noted that the morphological operators, as they are defined using extrema operators, do not take the metric of \mathbb{V} into account.

It is noticed in [Chevallier & Angulo \(2016\)](#) that it is a great challenge to define the problem of irregularity between a color image \mathbf{I} and its morphological image \mathbf{J} with a mathematical formalism and notation. However, the authors proposed an example to provide a visual interpretation of the irregularity that is similar to Figure 2.9.

Figure 2.9a) displays a toy image $\mathbf{I} : D \rightarrow \mathcal{C}_{RGB}$ with three RGB colors, specifically $\mathbf{u} = (0, 0, 0)$, $\mathbf{v} = (0, 0, 1)$, and $\mathbf{w} = (0.004, 0, 0)$. Note that \mathbf{u} and \mathbf{w} are visually black colors and therefore indistinguishable by human optical perception. Here we call \mathbf{u} a pure black color and \mathbf{w} simply a black color. Also, \mathbf{v} is a pure blue color. The toy image \mathbf{I} of size 32×64 is formed by two stripes of black including the pure black, black, and pure blue. The black stripe is generated by replacing the pure black colors \mathbf{u} by the black color \mathbf{w} with a probability of 30% and the blue stripe is generated by only the pure blue \mathbf{v} . Figure 2.9b) shows the dilated image $\mathbf{J}_L = \delta_S^L(\mathbf{I})$ with a cross-shaped structuring element S and the total lexicographical order \leq_L given in Example 2.4. Figure 2.9c) shows the dilated image $\mathbf{J}_M = \delta_S^M(\mathbf{I})$ with a cross-shaped structuring element S and the partial marginal order \leq_M given in Example 2.3. With the total order \leq_L , we have $\mathbf{u} \leq_L \mathbf{v} \leq_L \mathbf{w}$ and using the Euclidean metric $d(x, y) = \sqrt{\sum_{i=1}^3 (x_i - y_i)^2}$, we obtain $d(\mathbf{u}, \mathbf{v}) = 1$ and $d(\mathbf{u}, \mathbf{w}) = 0.004$, which agree with our vision perception. In this context, as $\mathbf{u} \leq_L \mathbf{v} \leq_L \mathbf{w}$ and $d(\mathbf{u}, \mathbf{w}) < d(\mathbf{u}, \mathbf{v})$, the image \mathbf{J}_L has irregularity because the pure blue \mathbf{v} advances over the pure black \mathbf{u} , however, the pure blue \mathbf{v} is covered by the black color \mathbf{w} . In contrast, the dilated image \mathbf{J}_M shown in Figure 2.9c) generated with the partial order \leq_M does not exhibit any visual irregularity.

Even though we understand that the irregularity issue is caused by a discrepancy between the topologies induced by the metric and the total ordering, there is no universally accepted method for quantifying this discrepancy that express with our visual perception. A quantitative measure would assist in selecting the appropriate ordering scheme for multivariate mathematical morphology. In this sense, the following chapter resents an irregularity measure for multivariate mathematical morphology.

MEASURING THE IRREGULARITY

This chapter suggests a quantitative measure for addressing the irregularity issue in multivariate mathematical morphology. Specifically, we present the *global irregularity index* introduced in [Valle et al. \(2021\)](#). This index provides insight into the irregular characteristics of images generated through morphological operators under total or partial orders. To contextualize our measure of irregularity, we briefly touch upon certain established concepts of image analysis, highlighting their relevance without delving into intricate details.

Before we continue, it is important to recognize a few important ideas that are commonly used when evaluating images. Measures such as fractal dimension and entropy offer insights into the complexity and textural diversity of images. For instance, notable methodologies include Minkowski's volumetric descriptors, developed by [Backes et al. \(2009\)](#), as applied, for example, in [Florindo et al. \(2013\)](#), alongside studies involving multifractal ([Harte, 2001](#)), multiscale fractal dimension ([Manoel et al., 2002](#)), and fractal descriptors ([Bruno et al., 2008](#)).

In the realm of entropy, notable studies like those conducted by Haralick in the 1970s ([Haralick et al., 1973](#)) and Ojala et al. in the 2000s ([Ojala et al., 2002](#)) consistently stress the importance of local patterns in recognizing textures. More recently, the distinctive role of non-additive entropy as a local texture descriptor has been explored in [Florindo et al. \(2016\)](#). Noteworthy efforts using non-additive entropy to enhance the performance of convolutional neural networks for texture description can also be observed, as seen in [Florindo & Metze \(2021\)](#). Additionally, non-additive entropies find application in facial recognition challenges ([Liao et al., 2006](#)), and texture recognition ([Florindo et al., 2016](#)).

Established metrics like the the Peak signal-to-noise ratio (PSNR) and the Structural Similarity Index (SSIM) are widely applied to assess image quality and likeness. For instance, the SSIM metric scrutinizes the structural resemblance between a pair of images, encompassing vital attributes such as luminance, contrast, and structure. Indeed, the SSIM was introduced by Wang and Bovik within the framework of the Universal Quality Index (UQI) ([Wang & Bovik, 2002](#)). Subsequently, adjustments were made to the UQI formulation by the authors to prevent division by zero, leading to the enhanced SSIM formulation as elucidated by [Wang et al. \(2004\)](#).

Although in this thesis, we do not delve into the specifics of the measures discussed above, such as fractal dimension, entropy, PSNR, and SSIM, it is important to acknowledge their

significance in the realm of image analysis and highlight the existence of studies involving these concepts. However, in this particular thesis, in the following section, we will outline our approach to quantify irregularity between two input images, \mathbf{I} and \mathbf{J} , obtained through morphological operators, utilizing the Wasserstein metric.

The Wasserstein metric is also known as the Kantorovich-Rubinstein distance or the Earth mover's distance (EMD). The name Kantorovich-Rubinstein distance comes from the fact that this distance was initially introduced by [Kantorovich \(1939\)](#), [Kantorovich & Rubinstein \(1942\)](#), and [Kantorovich \(1948\)](#), and it is based on the idea of finding the optimal transport plan between two probability distributions. The optimal transport plan minimizes the total cost of transporting mass from one probability distribution to another. The name Earth mover's distance (EMD) comes from the minimum amount of effort that must be done to transform one pile of earth into another pile of earth. Depending on the context, both names are still used as seen in [Rubner *et al.* \(2000\)](#) and in [Villani \(2003\)](#). After the paper [Vasershtein \(1969\)](#) of Russian mathematician Leonid Nisonovich Vaseršteĭn, it also started to be called Wasserstein metric. In the general case, the Wasserstein metric is used to compute distances between probability distributions.

We would like to highlight that unless stated otherwise, \mathbb{V} is considered to be a metric space in this thesis. Additionally, our proposed measure of irregularity only considers the metric space \mathbb{V} . As a result, it can be defined for morphological operators obtained by either a total or a partial order.

3.1 Irregularity Measure based on the Wasserstein Metric: The Global Irregularity Index

A first attempt to obtain an irregularity measure between the input image $\mathbf{I} \in \mathcal{V}$ and the output image $\mathbf{J} = \psi(\mathbf{I})$, where $\psi : \mathcal{V} \rightarrow \mathcal{V}$ is a morphological image operator like dilation, erosion, opening, or closing, is to calculate the sum of the distances $d(\mathbf{I}(x), \mathbf{J}(x))$ between the image values for each individual pixel $x \in D$. In this context, we refer to this sum as a sum of pixel-wise distances. In general, we can define a generalized sum of pixel-wise distances as follows:

Definition 3.1 (Generalized sum of pixel-wise distances). The generalized sum of pixel-wise distances of \mathbf{I} and \mathbf{J} is an operator $\mathcal{D}_p : \mathcal{V} \times \mathcal{V} \rightarrow [0, +\infty)$ given by

$$\mathcal{D}_p(\mathbf{I}, \mathbf{J}) = \left(\sum_{x \in D} d^p(\mathbf{I}(x), \mathbf{J}(x)) \right)^{\frac{1}{p}}, \quad p \geq 1. \quad (3.1)$$

Among the simplest measures that take into account both the positions of pixels and the metric d is the generalized sum of pixel-wise distances. Nonetheless, it is not appropriate

for measuring the irregularity. For instance, if Φ is a good irregularity measure then, for the images in Figure 2.9, we must definitely obtain $\Phi(\mathbf{I}, \mathbf{J}_M) \leq \Phi(\mathbf{I}, \mathbf{J}_L)$ since our visual perception clearly indicates that the image \mathbf{J}_L is much more irregular than the image \mathbf{J}_M . However, using the generalized sum of pixel-wise distances with $p = 1$ and the Euclidean metric, we have $\mathcal{D}_1(\mathbf{I}, \mathbf{J}_L) = 32.12$, $\mathcal{D}_1(\mathbf{I}, \mathbf{J}_M) = 66.04$, which implies that $\mathcal{D}_1(\mathbf{I}, \mathbf{J}_L) \leq \mathcal{D}_1(\mathbf{I}, \mathbf{J}_M)$. Consequently, a measure of irregularity can not be accurately determined by using the generalized sum of pixel-wise distances.

As it has been determined that \mathcal{D}_p is not a viable measure for irregularity issue, it is imperative to seek out other solutions. In this regard, we discuss the Wasserstein metric. First of all, Villani (2009) defines the Wasserstein metric of order p , for $p \geq 1$, between two probability measures μ, ν in a Polish metric space (χ, d) by the formula

$$\mathcal{W}_p(\mu, \nu) = \left(\inf_{\pi \in \Pi(\mu, \nu)} \int_{\chi \times \chi} d(x, y)^p d\pi(x, y) \right)^{\frac{1}{p}}. \quad (3.2)$$

In other words, the Wasserstein metric $\mathcal{W}_p(\mu, \nu)$ of order $p \geq 1$ is a way to measure the minimum cost of transferring between two probability measures μ and ν . It is defined on a Polish metric space (χ, d) , which is a complete separable metric space. Since χ is separable, the existence of an optimal transfer plane is a direct implication of Prokhorov's theorem (Prokhorov, 1956). In addition, the infimum in (3.2) is calculated over all transference plans π between μ and ν . i.e., the set $\Pi(\mu, \nu)$ of Borel probability measures on $\chi \times \chi$ with respective marginal distributions equal to μ and ν . When considering discrete probability measures μ and ν , the Wasserstein metric can be formulated as a linear programming problem, also known as a transportation problem.

The theory of optimal transport (OT) has a long history and has consequences in several different areas. Optimal transport was motivated by an engineering problem discussed in approximately 1781 with a paper by Gaspard Monge (Monge, 1781). After the years, Tolstoi in the 1920s, and Hitchcock, Kantorovich, and Koopmans in the 1940s established its significance to logistics and economics. By 1949, the optimal transport theory was solved by numerical problems using a linear programming framework. In the 1990s, optimal transport theory gained fame in computer vision with Brenier, and in recent years, the theory was applied in various problems in imaging sciences (such as color or texture processing), graphics (for shape manipulation), and machine learning (for regression, classification, and generative modeling) (Ambrosio, 2003; Peyré & Cuturi, 2019). Furthermore, according to Santambrogio (2015), the optimal transport theory leads to connections with partial differential equations, fluid mechanics, functional analysis, geometry, and probability theory. The impact of optimal transport on geometry was highlighted by two Field medals, as we can see in Figalli (2021) and in Villani (2003, 2009, 2021).

According to Peyré & Cuturi (2019), the purpose of a transportation problem is to minimize the cost associated with distributing items from n factories to m stores. According to the authors, the transportation problem has several variations and ramifications giving rise to

current research problems. To exemplify the main idea of this problem, we discuss it below as presented by [Luenberger \(1984\)](#).

There are n origins with the same commodity and m destinations. Each origin i contains an amount a_i and each destination j needs an amount b_j . Assuming that total supply equals total demand, i.e., $\sum_{i=1}^n a_i = \sum_{j=1}^m b_j$, and that the unit cost of getting a commodity from origin i to destination j is given by c_{ij} , we want to find the transportation between origins and destinations that satisfies all requirements and minimizes the total transportation cost.

In mathematical notation, the problem is to find the set of values x_{ij} for all $i \in \{1, 2, \dots, n\}$ and $j \in \{1, 2, \dots, m\}$ that solves the following linear programming problem

$$\left\{ \begin{array}{l} \text{minimize} \quad \sum_{i=1}^n \sum_{j=1}^m c_{ij} x_{ij} \\ \text{subject to} \quad \sum_{j=1}^m x_{ij} = a_i, \quad \text{for all } i = 1, \dots, n, \\ \quad \quad \quad \sum_{i=1}^n x_{ij} = b_j, \quad \text{for all } j = 1, \dots, m, \\ \quad \quad \quad x_{ij} \geq 0, \quad \text{for all } i = 1, \dots, n, \text{ and for all } j = 1, \dots, m. \end{array} \right. \quad (3.3)$$

The transportation problem is always well defined and always has an optimal solution. Furthermore, the values of x_{ij} can be considered real or integer, depending on the context of the problem. Within the scope of this thesis, the aim of the transportation problem is to minimize the cost of converting the input image \mathbf{I} into the output image \mathbf{J} , and the variable x_{ij} represents the number of pixels with value v_i in \mathbf{I} that are transformed into pixels with value u_j in \mathbf{J} .

Strictly, the cost c_{ij} of transforming \mathbf{I} into \mathbf{J} is defined by the metric d of \mathbb{V} . Precisely, let $V(\mathbf{I}) = \{v_1, \dots, v_n\}$ and $V(\mathbf{J}) = \{u_1, \dots, u_m\}$ be the sets of color values of \mathbf{I} and \mathbf{J} , respectively. The cost to transform a value v_i of \mathbf{I} into a value u_j of \mathbf{J} is defined by

$$c_{ij} = d^p(v_i, u_j), \quad \forall i = 1, \dots, n, \quad \forall j = 1, \dots, m. \quad (3.4)$$

Furthermore, the conditions $\sum_{j=1}^m x_{ij} = a_i, \forall i \in \{1, \dots, n\}$ and $\sum_{i=1}^n x_{ij} = b_j, \forall j \in \{1, \dots, m\}$ of (3.3) means that for image \mathbf{I} , the sum of the quantities transported for each color is equal to its available capacity, and for image \mathbf{J} , the sum of the quantities transported for each color is equal to its demand. Thus, in our context, we have

$$\sum_{j=1}^m x_{ij} = \text{Card}(\{\mathbf{x} : \mathbf{I}(\mathbf{x}) = v_i, \mathbf{x} \in D\}), \quad \forall i = 1, \dots, n, \quad (3.5)$$

and

$$\sum_{i=1}^n x_{ij} = \text{Card}(\{\mathbf{x} : \mathbf{J}(\mathbf{x}) = u_j, \mathbf{x} \in D\}), \quad \forall j = 1, \dots, m. \quad (3.6)$$

This condition leads to the following definition:

Definition 3.2 (Wasserstein metric). The Wasserstein metric, denoted by $\mathcal{W}_p : \mathcal{V} \times \mathcal{V} \rightarrow [0, \infty)$ is given by

$$\mathcal{W}_p(\mathbf{I}, \mathbf{J}) = \left(\sum_{i=1}^n \sum_{j=1}^m c_{ij} x_{ij} \right)^{1/p}, \quad p \geq 1, \quad (3.7)$$

where x_{ij} solves (3.3).

For an investigation into the suitability of the Wasserstein metric as an irregularity measure, we use $p = 1$, the Euclidean metric, and determine the values of $\mathcal{W}_1(\mathbf{I}, \mathbf{J}_L)$ and $\mathcal{W}_1(\mathbf{I}, \mathbf{J}_M)$, where \mathbf{I} , \mathbf{J}_L , and \mathbf{J}_M are the images depicted in Figure 2.9. We compare the obtained results in a way analogous we have done for calculating the generalized sum of pixel-wise distances. In this case, the results are $\mathcal{W}_1(\mathbf{I}, \mathbf{J}_L) = 4.18$ and $\mathcal{W}_1(\mathbf{I}, \mathbf{J}_M) = 65.93$ implying the inequality $\mathcal{W}_1(\mathbf{I}, \mathbf{J}_L) \leq \mathcal{W}_1(\mathbf{I}, \mathbf{J}_M)$. Unfortunately, like the generalized sum of pixel-wise distances \mathcal{D}_p , the Wasserstein metric \mathcal{W}_p does not provide a measure for the irregularity issue.

As seen in the above paragraph, \mathcal{D}_p and \mathcal{W}_p do not provide an irregularity measure. Specifically, \mathcal{D}_p computes the distances of individual pixel values between the images \mathbf{I} and \mathbf{J} , while \mathcal{W}_p is essentially the minimum cost required to transform image \mathbf{I} into \mathbf{J} . Nonetheless, the information of \mathcal{D}_p and \mathcal{W}_p is useful to propose a new irregularity measure for multivariate mathematical morphology, which we refer to as the global irregularity index.

In order to formally define the global irregularity index, note that the generalized sum of pixel-wise distances \mathcal{D}_p can also be interpreted as a measure of the cost of transforming an image \mathbf{I} into \mathbf{J} . In fact, \mathcal{D}_p given by (3.1) satisfies

$$\mathcal{D}_p(\mathbf{I}, \mathbf{J}) = \left(\sum_{i=1}^n \sum_{j=1}^m c_{ij} y_{ij} \right)^{\frac{1}{p}}, \quad p \geq 1, \quad (3.8)$$

where

$$y_{ij} = \text{Card}(\{\mathbf{x} : \mathbf{I}(\mathbf{x}) = v_i \text{ and } \mathbf{J}(\mathbf{x}) = u_j, \mathbf{x} \in D\}), \quad (3.9)$$

for all $i \in \{1, \dots, n\}$ and $j \in \{1, \dots, m\}$. Moreover, observe that $y_{ij} \geq 0$ and the identities

$$\sum_{j=1}^m y_{ij} = a_i \quad \text{and} \quad \sum_{i=1}^n y_{ij} = b_j, \quad (3.10)$$

where $a_i = \text{Card}(\{\mathbf{x} : \mathbf{I}(\mathbf{x}) = v_i\})$ and $b_j = \text{Card}(\{\mathbf{x} : \mathbf{J}(\mathbf{x}) = u_j\})$, hold for all $i = 1, \dots, n$ and $j = 1, \dots, m$.

Additionally, \mathcal{D}_p and \mathcal{W}_p have the same unit of measurement and as \mathcal{W}_p is the minimal cost, it follows that $\mathcal{W}_p(\mathbf{I}, \mathbf{J}) \leq \mathcal{D}_p(\mathbf{I}, \mathbf{J})$ for any images \mathbf{I} and $\mathbf{J} = \psi(\mathbf{I})$.

Based on these observations, we put forth a method for measuring irregularity by taking into account the relative difference between \mathcal{D}_p and \mathcal{W}_p . Specifically, we have the following definition:

Definition 3.3 (Global irregularity index). Let $\mathbf{I} \in \mathcal{V}$ be an image from a domain D to a range \mathbb{V} , and let $\mathbf{J} = \psi(\mathbf{I})$ be an image obtained by a morphological operator ψ . We define the global irregularity index as a mapping $\Phi_p^g : \mathcal{V} \times \mathcal{V} \rightarrow [0, 1]$ given by

$$\Phi_p^g(\mathbf{I}, \mathbf{J}) = \begin{cases} 0, & \text{if } \mathcal{D}_p(\mathbf{I}, \mathbf{J}) = 0, \\ \frac{\mathcal{D}_p(\mathbf{I}, \mathbf{J}) - \mathcal{W}_p(\mathbf{I}, \mathbf{J})}{\mathcal{D}_p(\mathbf{I}, \mathbf{J})}, & \text{otherwise.} \end{cases} \quad (3.11)$$

It is worth noting that the global irregularity index Φ_p^g is directly proportional to the extent of the discrepancy between $\mathcal{W}_p(\mathbf{I}, \mathbf{J})$ and $\mathcal{D}_p(\mathbf{I}, \mathbf{J})$. Likewise, we have

$$\Phi_p^g(\mathbf{I}, \mathbf{J}) = \begin{cases} 0, & \text{if } \mathcal{D}_p(\mathbf{I}, \mathbf{J}) = 0, \\ 1 - \frac{\mathcal{W}_p(\mathbf{I}, \mathbf{J})}{\mathcal{D}_p(\mathbf{I}, \mathbf{J})}, & \text{otherwise.} \end{cases} \quad (3.12)$$

A high $\Phi_p^g(\mathbf{I}, \mathbf{J})$ value indicates a high degree of irregularity between the images, while a low $\Phi_p^g(\mathbf{I}, \mathbf{J})$ value indicates a low degree of irregularity in the image. Furthermore, the values of $\Phi_p^g(\mathbf{I}, \mathbf{J})$ are between 0 and 1, i.e., $0 \leq \Phi_p^g(\mathbf{I}, \mathbf{J}) \leq 1$, which means that Φ_p^g is bounded and it is easy to note that $\Phi_p^g(\mathbf{I}, \mathbf{J}) = \Phi_p^g(\mathbf{J}, \mathbf{I})$, which means that Φ_p^g is symmetric. Moreover, $\Phi_p^g(\mathbf{I}, \mathbf{J})$ is dimensionless and the greater the irregularity of $\mathbf{J} = \psi(\mathbf{I})$, the larger the value of $\Phi_p^g(\mathbf{I}, \mathbf{J})$. For instance, when $p = 1$ and the Euclidean metric are chosen, the global irregularity index of the dilated images \mathbf{J}_L and \mathbf{J}_M shown in Figure 2.9b) and 2.9c) are $\Phi_1^g(\mathbf{I}, \mathbf{J}_L) = 70.23\%$ and $\Phi_1^g(\mathbf{I}, \mathbf{J}_M) = 0.19\%$, respectively. As expected, $\Phi_1^g(\mathbf{I}, \mathbf{J}_M) \leq \Phi_1^g(\mathbf{I}, \mathbf{J}_L)$.

Example 3.1. Consider the three-colored image \mathbf{I} and the dilated image \mathbf{J}_L shown in Figure 2.9. The operator's and the optimal transport plans are presented in the subsequent matrices:

$$Y = \begin{bmatrix} 156 & 18 & 541 \\ 0 & 1010 & 14 \\ 0 & 0 & 309 \end{bmatrix} \quad \text{and} \quad X = \begin{bmatrix} 156 & 4 & 550 \\ 0 & 1024 & 0 \\ 0 & 0 & 309 \end{bmatrix}. \quad (3.13)$$

Because $\mathbf{u} = (0, 0, 0)$, $\mathbf{v} = (0, 0, 1)$, and $\mathbf{w} = (0.004, 0, 0)$, we have

$$\mathcal{D}_1(\mathbf{I}, \mathbf{J}_L) = 18d(\mathbf{u}, \mathbf{v}) + 541d(\mathbf{u}, \mathbf{w}) + 14d(\mathbf{v}, \mathbf{w}) = 34.12, \quad (3.14)$$

$$\mathcal{W}_1(\mathbf{I}, \mathbf{J}_L) = 4d(\mathbf{u}, \mathbf{v}) + 555d(\mathbf{u}, \mathbf{w}) = 6.18, \quad (3.15)$$

and

$$\mathcal{D}_1(\mathbf{I}, \mathbf{J}_L) - \mathcal{W}_1(\mathbf{I}, \mathbf{J}_L) = 14(d(\mathbf{u}, \mathbf{v}) + d(\mathbf{v}, \mathbf{w}) - d(\mathbf{u}, \mathbf{w})) = 27.95, \quad (3.16)$$

From (3.16), we conclude that the cost of the operator's plan can be reduced by replacing 14 times the route $\mathbf{u} \rightarrow \mathbf{v} \rightarrow \mathbf{w}$ by $\mathbf{u} \rightarrow \mathbf{w}$ or, equivalently, by avoiding the cycle (\mathbf{u}, \mathbf{v}) , (\mathbf{v}, \mathbf{w}) , (\mathbf{w}, \mathbf{u}) . Moreover, note that the route $\mathbf{u} \rightarrow \mathbf{v} \rightarrow \mathbf{w}$ reflects the lexicographical inequalities

$\mathbf{u} \leq_L \mathbf{v} \leq_L \mathbf{w}$. Thus, the difference $\mathcal{D}_1(\mathbf{I}, \mathbf{J}_L) - \mathcal{W}_1(\mathbf{I}, \mathbf{J}_L)$ is proportional to the number of pixels with irregular values (14 in this example) as well as to the distance between the pixel values (in this example, the amount $d(\mathbf{u}, \mathbf{v}) + d(\mathbf{v}, \mathbf{w}) - d(\mathbf{u}, \mathbf{w})$). The global irregularity index is obtained by dividing the difference $\mathcal{D}_1(\mathbf{I}, \mathbf{J}_L) - \mathcal{W}_1(\mathbf{I}, \mathbf{J}_L)$ by $\mathcal{D}_1(\mathbf{I}, \mathbf{J}_L)$ as seen in (3.11), that is,

$$\Phi_1^g(\mathbf{I}, \mathbf{J}_L) = \frac{\mathcal{D}_1(\mathbf{I}, \mathbf{J}_L) - \mathcal{W}_1(\mathbf{I}, \mathbf{J}_L)}{\mathcal{D}_1(\mathbf{I}, \mathbf{J}_L)} = \frac{27.95}{34.12} = 0.819. \quad (3.17)$$

Example 3.2. One extremely important point to emphasize is that our global irregularity index $\Phi_p^g(\mathbf{I}, \mathbf{J})$ has some restrictions. The global irregularity index Φ_p^g does not assess, for instance, isometries, such as rotations, translations, and reflections. It is also inapplicable to images in which pixel values are merely rearranged, as demonstrated in Figure 3.1.

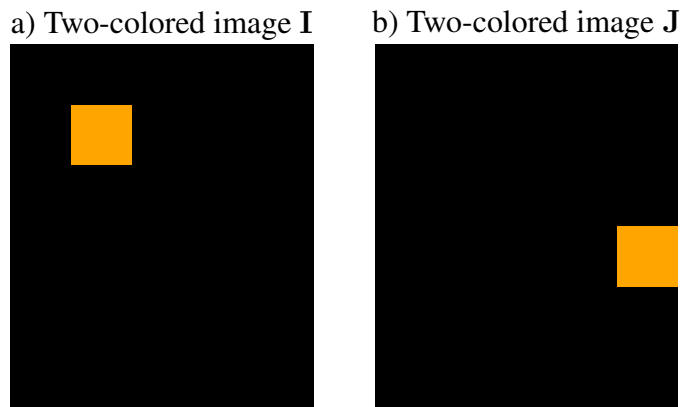


Figure 3.1 – Figure a) shows image \mathbf{I} with size 6×5 consisting of two colors: black and orange. Figure b) depicts the image \mathbf{J} , acquired through a permutation of color values in \mathbf{I} at positions $(2, 2)$ and $(4, 5)$.

Specifically, in Figure 3.1(a), we have a colored image \mathbf{I} of size 6×5 , where all color values are black except at $\mathbf{I}(2, 2)$, which is orange. In Figure 3.1(b), we present an image \mathbf{J} obtained by permuting color values at $(2, 2)$ and $(4, 5)$, resulting in the color black throughout \mathbf{J} except at $\mathbf{J}(4, 5)$, which remains orange. In this scenario, the images \mathbf{I} and \mathbf{J} share an identical color histogram, causing the Wasserstein metric $\mathcal{W}_p(\mathbf{I}, \mathbf{J})$ to be zero. Applying the global irregularity index given by (3.12) yields a result of 1.

Example 3.3. The graphical representation in Figure 3.2 illustrates the results of applying the dilation operator, denoted by $\mathbf{J}_L = \delta_S^L(\mathbf{I})$ and $\mathbf{J}_M = \delta_S^M(\mathbf{I})$, to toy images similar in nature to the example depicted in Figure 2.9. Remember that S denotes the structuring element which, in this case, was also adopted as a cross shape. More specifically, we initially considered the image \mathbf{I} of size 64×32 with two stripes of size 64×16 . The first stripe is formed by pure black color $\mathbf{u} = (0, 0, 0)$ and the second stripe is formed by pure blue color $\mathbf{v} = (0, 0, 1)$. Subsequently, we randomly replace \mathbf{u} by the black color $\mathbf{w} = (0.004, 0, 0)$ with probability $\pi \in [0, 1]$ in the first stripe. It is worth noting that the example in Figure 2.9 was performed with probability $\pi = 30\%$. In Figure 3.2, we show the dilated images \mathbf{J}_L of \mathbf{I} when the image \mathbf{I} was performed

at 0%, 25%, 50%, 75%, and 100%. Additionally, as the values of w were randomly chosen, we performed each simulation 500 times for each probability $\pi \in [0, 1]$. Therefore, we show in the top of the Figure 3.2 the percentage obtained from the average of the global irregularity index $\Phi_1^g(\mathbf{I}, \mathbf{J}_L)$ and $\Phi_1^g(\mathbf{I}, \mathbf{J}_M)$ by the probability π . In accordance with the methodology outlined in the example illustrated in Figure 2.9, $p = 1$ and the Euclidean metric were utilized.

The data presented in Figure 3.2 illustrates that the irregularity index for the lexicographical RGB ordering exhibits an upward trend until reaching a maximum value near $\pi = 30\%$. Thereafter, a downward trend is observed. Furthermore, the irregularity indexes are consistent with the visual irregularity observed in the sample images presented at the bottom of Figure 3.2. Conversely, the marginal approach yields minimal irregularity indexes.

This toy example supports our hypothesis that the global irregularity index $\Phi_1^g(\mathbf{I}, \mathbf{J})$ increases with the level of irregularity in the transformed image $\mathbf{J} = \psi(\mathbf{I})$. Also, the global irregularity index, when applied to images \mathbf{I} and \mathbf{J} involving a total ordering, is larger than the global irregularity index involving a partial ordering.

3.2 Computational Analysis of Tiny Color Images

In this section, we present the computational results obtained when implementing the proposed algorithm in Julia. All experiments were performed on a machine with the following specifications:

- Operating System: Windows 10 Home Single Language (version 22H2)
- Processor: 11th Gen Intel(R) Core(TM) i7-1165G7, 4.70 GHz, 4 cores
- Memory RAM: 16 GB 3200 MHz DDR4

Our computational experiments are realized with tiny color images¹. Specifically, we calculate the global irregularity index Φ_1^g of morphological operators applied to 100 color images from the CIFAR-10 dataset. The CIFAR-10 dataset includes 60,000 color images, each with a size of 32×32 pixels divided by ten classes (Krizhevsky, 2009).

The running time was calculated using Julia's `@time` function and represents the total CPU time spent by the algorithm to process the input. For small images of the CIFAR-10 dataset that are size of 32×32 , the average running time to calculate the global irregularity index Φ was 18.66 seconds.

We observed behavior consistent with the theoretical complexity of the algorithm, which according to Pitić (2020) is $\mathcal{O}(n^3 m^3 \log(nm))$, where n and m are less than or equal to

¹ The program code of the global irregularity index is located at <https://github.com/mevalle/Irregularity-Index>.

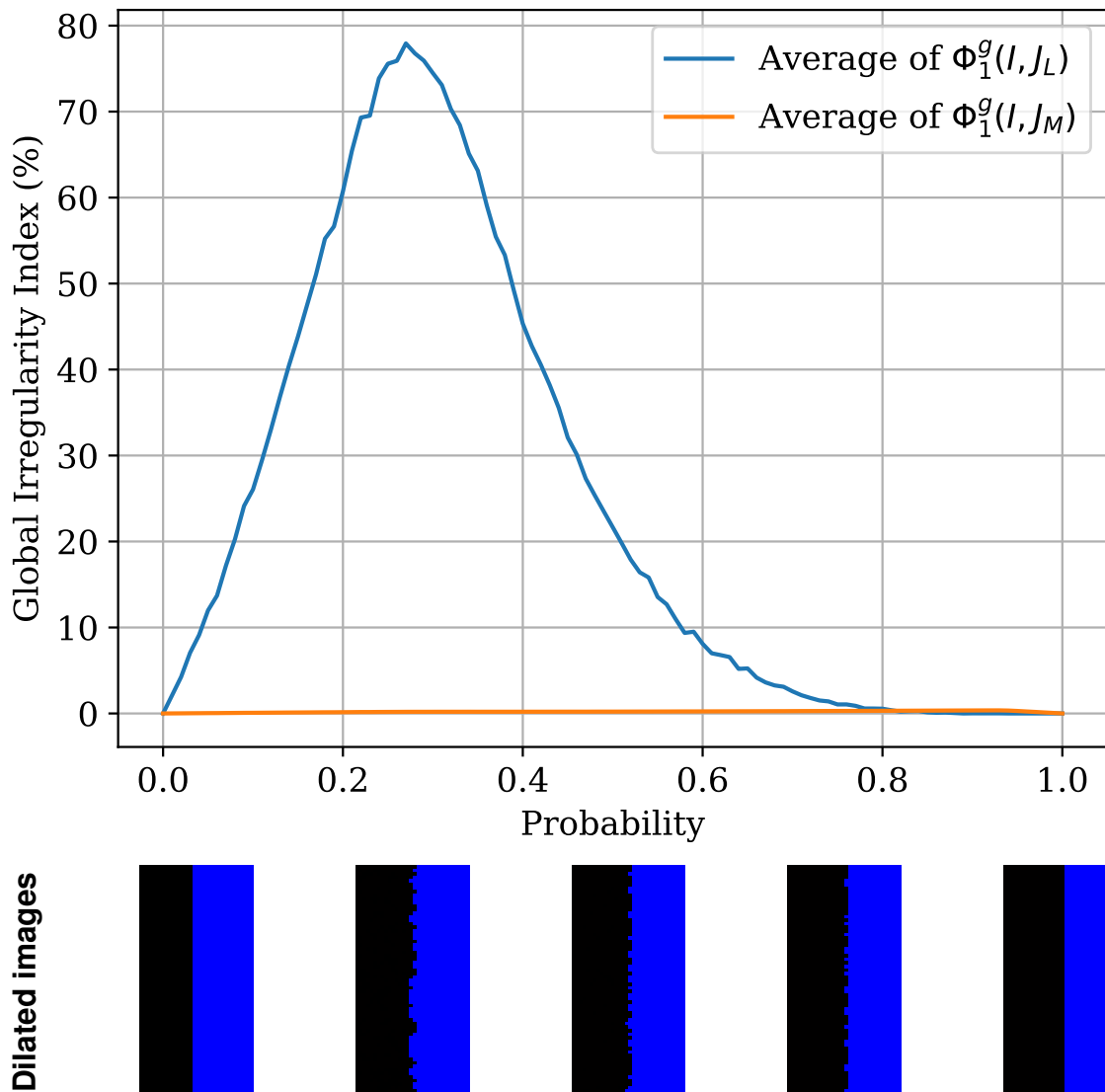


Figure 3.2 – **Top:** Global irregularity index calculated by the likelihood of substituting $\mathbf{u} = (0, 0, 0)$ with $\mathbf{w} = (0.005, 0, 0)$. **Bottom:** Images that have undergone dilation using values of π ranging from 0.0 to 1.0, incrementing by 0.25 each time, respectively.

32×32 . These results confirm the effectiveness of the proposed algorithm in terms of execution time and use of computational resources, validating its applicability in practical scenarios.

We used the Euclidean metric as the metric of the RGB value set. We consider the value of $p = 1$ for the calculation of the Wasserstein metric and also the generalized sum of pixel-wise distances. The use of $p = 1$ in the Wasserstein metric emphasizes linear movement and transport direct mass between the color distributions of the images \mathbf{I} and \mathbf{J} . A future possibility is to discuss and interpret results obtained for different values of p and different metrics on the RGB value set.

We have used dilation, erosion, opening, and closing with a 3×3 square structuring element S to calculate the quantitative measures. Definitely, we performed twenty-five dilations, erosions, openings, and closings on different images from the CIFAR-10 dataset.

























	Original img.	Marginal	Loewner	Lex. RGB	SVM-based	Proj. Depth
Dilation						
		0.93%	0.87%	1.37%	8.60%	5.38%
Erosion						
		0.93%	0.86%	1.36%	12.04%	45.27%
Opening						
		2.79%	2.83%	7.07%	34.84%	31.13%
Closing						
		2.61%	2.68%	6.33%	21.26%	74.53%

Figure 3.3 – The global irregularity index Φ_1^g that were computed for small color images using dilation, erosion, opening, and closing operators.

We used the morphological approaches that were discussed in Chapter 2. Specifically, we used two approaches based on partial orderings and three morphological approaches based on total orderings. Regarding partial orderings, we considered the marginal order as seen in Example 2.3 and an approach based on Loewner order as seen in Subsection 2.3.3. Because these two approaches are not based on total orderings, we expect they circumvent the irregularity issue. For the total orderings, we employed the lexicographical order in which the colors were arranged consecutively based on the red, green, and blue components. The lexicographical order was presented in Example 2.4. The last two approaches are the ones we discussed in Subsections 2.3.1 and 2.3.2 which are, respectively, the supervised approach based on SVM, with the radial basis function kernel (RBF kernel), and the unsupervised projection depth approach.

Figure 3.3 shows the output generated by morphological operators and the associated global irregularity index are presented. The images in the first column in Figure 3.3 are the original images. The following columns show the results of morphological operators defined using the marginal, Loewner, lexicographical RGB, supervised SVM-based, and projection depth approaches, respectively. The global irregularity index is shown below the images resulting from the morphological operators.

As expected, the marginal and the Loewner approaches yielded global irregularity indexes smaller than the lexicographical, SVM-based, and projection depth approaches. For the

cat in the first row, the dilation of the marginal and Loewner images are visually quite similar. The same statement is true for the marginal and Loewner approach for the frog, truck and car images for the erosion, opening and closing operators, respectively. We note that the global irregularity indexes for both approaches are almost equal, with 0.93% for the marginal dilation and 0.87% for the dilation based on the Loewner order. For erosion we have 0.93% for marginal and 0.86% for Loewner. For the opening we have 2.79% for the marginal and 2.83% for the Loewner. Finally, we have for the closing 2.61% for the marginal and 2.68% for the Loewner. Our findings reveal a consistent trend of higher global irregularity values for opening and closing operations compared to dilation and erosion. This trend aligns with theoretical expectations, as opening and closing operations involve additional steps that lead to increased irregularity through composition with dilation and erosion. Notably, the irregularity computed using the marginal order is observed to be lower than the Loewner order in certain instances, although this relationship is not universally consistent. Specifically, we observe exceptions in the images of the cat and the frog, where the Loewner order yields lower irregularity values.

The dilated image produced by the supervised SVM-based approach was determined to be the most irregular dilation with an irregularity percentage of 8.60%. This result is interesting because it was more irregular even than the value obtained from the unsupervised projection depth approach, in which the irregularity of the dilation of the cat is 5.38%. It is worth noting here that the projection depth approach was the morphological approach in which the irregularity values were significantly high. For this approach, the median was 45.22%. Additionally, note that the car in the closing for the projection depth has an irregularity of 74.53% and a typical value found in the projection depth approach is as the frog in the erosion with a value of 45.27%. Actually, the closing of the car obtained by the projection depth approach was the highest global irregularity index in this experiment. With regard to the other morphological approaches, the median of the global irregularity indices were 2.56%, 2.81%, 6.00%, and 22.98%, for the marginal, Loewner, lexicographical RGB, and SVM-based orders, respectively. The global irregularity index of the truck image's openings and the car image's closings are representative examples of what is produced by the marginal, Loewner, and lexicographical approaches.

The summary of this computational experiment can be found in the boxplot of Figure 3.4. As anticipated, the use of marginal and Loewner partial orderings resulted in lower global irregularity indexes, while the use of lexicographical RGB, SVM-based, and projection depth total orderings resulted in higher global irregularity indexes. Accordingly, the morphological approaches can be ranked using the global irregularity index as follows in an increasing manner: marginal, Loewner, lexicographical RGB, supervised SVM-based, and projection depth. We confirmed the ranking of the morphological approaches statistically using the Wilcoxon signed-rank test with a confidence level of 99% or, in simpler terms, we were able to determine that the ranking of the morphological approaches is statistically significant with a high degree of confidence. In summary, the use of total orderings in morphological operators resulted in greater global irregularity indexes compared to those obtained with partial orderings. This

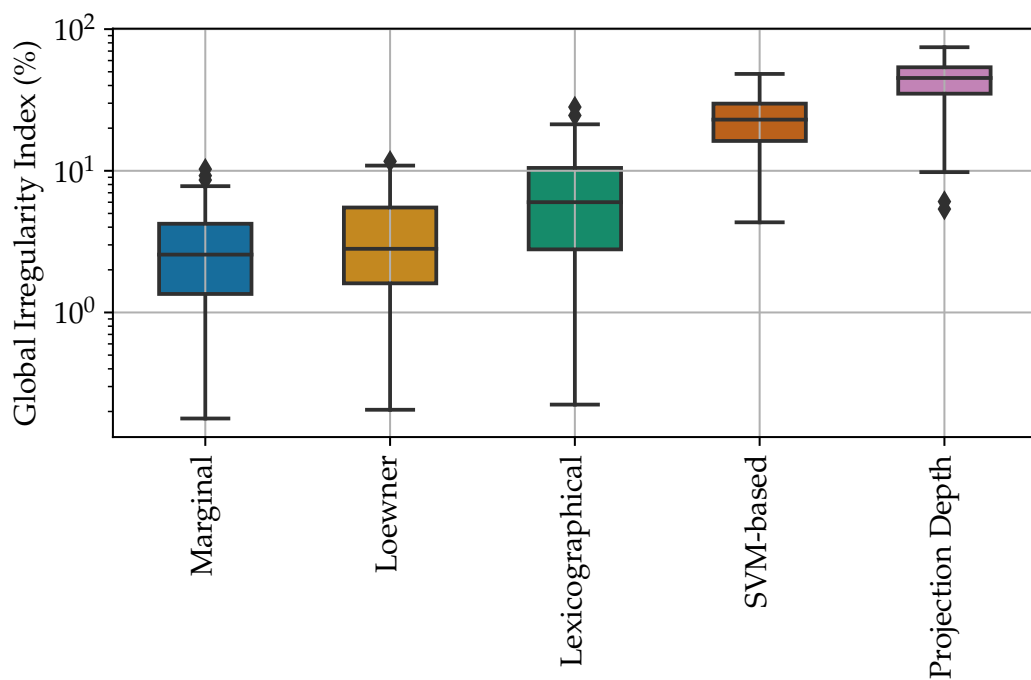


Figure 3.4 – Presentation of the global irregularity index distribution of 100 small color images for 5 morphological approaches.

conclusion supports the suitability of the global irregularity index outlined in (3.12) as a measure of irregularity.

It should be highlighted that the irregularity issue can not be accurately measured by either the generalized sum of pixel-wise distances or the Wasserstein metric. For instance, the values of these metrics between the original and eroded frog image produced by the marginal approach are 182.31 and 180.61, respectively, while the values between the original and the eroded frog image produced by the projection depth approach are 135.44 and 74.13, respectively. Despite the lower values of these metrics in the projection depth approach, it is clear that the resulting image is more irregular than the one produced by the marginal approach. In contrast, a greater degree of irregularity does not always correlate with a larger generalized sum of pixel-wise distances or a larger Wasserstein metric value. For instance, the generalized sum of pixel-wise distances and the Wasserstein metric between the original truck image and its opening via the marginal approach are 31.05 and 30.18, respectively. The same measures between the original truck image and its opening via the projection depth approach are 53.96 and 37.17. Despite this, the projection depth approach produced a more irregular image of the truck than the opening produced by the marginal approach.

CALCULATING THE IRREGULARITY MEASURE

In Chapter 3 we presented the global irregularity index for measuring the irregularity issue. In the mathematical formulation for the global irregularity index, we used the Wasserstein metric, in which we need to solve the optimization problem given by (3.3).

We have seen that the global irregularity index is consistent with our visual perception by means of the computational experiments detailed in Section 3.2. In other words, we have verified by computational experiments the validity of the proposed theory for toy images such as the one discussed in Example 3.3 and shown in Figure 3.2. Furthermore, we have discussed the validity of the global irregularity index for small images from the CIFAR-10 dataset, such as the one illustrated in Figure 3.3. It should be noted that, while the global irregularity index may be mathematically formulated, its calculation presents a significant challenge in the context of natural images. To be precise, the calculation of the global irregularity index necessitates the solution of a linear programming problem with a total of nm variables, where n and m denote the number of distinct pixel values in the images \mathbf{I} and \mathbf{J} , respectively. Consequently, calculating the global irregularity index is a computationally intensive task that increases in complexity as $\mathcal{O}(n^3m^3 \log(nm))$, as stated in Pitié (2020). In real-world situations, the dimension of the linear programming problem outlined in (3.3) is too large to be computationally feasible, making it impossible to calculate the global irregularity index in real-time.

Initially, Valle *et al.* (2021) proposed a way to calculate the Wasserstein metric and the generalized sum of pixel-wise distances locally and aggregate the values into a single quantitative index to circumvent the computational burden. We used windows $W_i \subset D$, for $i \in \{1, 2, \dots, k\}$, where D is the domain of an image \mathbf{I} , such that $W_i \cap W_j \neq \emptyset$ and $\cup_{i=1}^k W_i = D$ to obtain a measure of the irregularity of an image. For each local window W_i , $i = 1, \dots, k$, we solved a local optimization problem and computed an irregularity index bounded to the window W_i . The local irregularity index was calculated by means of a geometric mean of all the irregularity indices restricted to W_i (Valle *et al.*, 2021).

However, we realized that the geometric mean does not give a good measure for large images because the product involved in computing the geometric mean converges to zero

when we have many local windows W_i . We have given a solution for this problem and, in this chapter, we discuss the results that we have achieved.

4.1 The Local Irregularity Measure for Natural Images

Consider images $\mathbf{I}, \mathbf{J} \in \mathcal{V}$ and let $\mathcal{P} = \{W_1, W_2, \dots, W_k\}$ be a partition of the image domain D , that is, W_1, W_2, \dots, W_k are non-overlapping local windows ($W_i \cap W_j = \emptyset$ for all $i \neq j$) such that $\cup_{i=1}^k W_i = D$. Additionally, denote $\mathcal{W}_p(\mathbf{I}, \mathbf{J}|W_\ell)$ the Wasserstein metric computed restricting the images \mathbf{I} and \mathbf{J} to the local window W_ℓ . We define the local irregularity measure or index as follows:

Definition 4.1 (Local irregularity index). Let $\mathbf{I} \in \mathcal{V}$ be an image from a domain D to a range \mathbb{V} , and let $\mathbf{J} = \psi(\mathbf{I})$ be an image obtained by a morphological operator ψ . We define the local irregularity index by

$$\Phi_p^l(\mathbf{I}, \mathbf{J}) = 1 - \frac{\left(\sum_{\ell=1}^k (\mathcal{W}_p(\mathbf{I}, \mathbf{J}|W_\ell))^p \right)^{1/p}}{\mathcal{D}_p(\mathbf{I}, \mathbf{J})}, \quad p \geq 1. \quad (4.1)$$

The local irregularity index provides a lower bound to the global irregularity index, i.e., the inequality $\Phi_p^l(\mathbf{I}, \mathbf{J}) \leq \Phi_p^g(\mathbf{I}, \mathbf{J})$ holds true for all $\mathbf{I} \in \mathcal{V}$ and $\mathbf{J} = \psi(\mathbf{I})$.

The following intuitively explains this inequality. Considering a transport problem in Brazil, suppose the country is divided into k regions, with k being a natural number. Each region is a local window W_ℓ . In each region, we solve the linear transport problem given by (3.3), which in our context means that we obtain a Wasserstein metric restricted to each local window W_ℓ . In other words, we have for each region a transport cost and its respective optimal cost obtained by the Wasserstein metric. If we consider the solution of the linear transport problem throughout the Brazilian territory, we have the transport plan x_{ij} relative to the lowest transport cost c_{ij} that encompasses all possible transport combinations, including those performed in the k regions. This implies that for $\ell \in \{1, \dots, k\}$,

$$(\mathcal{W}_p(\mathbf{I}, \mathbf{J}|W_1))^p + \dots + (\mathcal{W}_p(\mathbf{I}, \mathbf{J}|W_k))^p \geq \mathcal{W}_p(\mathbf{I}, \mathbf{J})^p, \quad (4.2)$$

that is,

$$\left(\sum_{\ell=1}^k (\mathcal{W}_p(\mathbf{I}, \mathbf{J}|W_\ell))^p \right)^{1/p} \geq \mathcal{W}_p(\mathbf{I}, \mathbf{J}), \quad (4.3)$$

and for $\mathcal{D}_p(\mathbf{I}, \mathbf{J}) > 0$,

$$1 - \frac{\left(\sum_{\ell=1}^k (\mathcal{W}_p(\mathbf{I}, \mathbf{J}|W_\ell))^p \right)^{1/p}}{\mathcal{D}_p(\mathbf{I}, \mathbf{J})} \leq 1 - \frac{\mathcal{W}_p(\mathbf{I}, \mathbf{J})}{\mathcal{D}_p(\mathbf{I}, \mathbf{J})}. \quad (4.4)$$

If $\mathcal{D}_p(\mathbf{I}, \mathbf{J}) = 0$, then \mathbf{I} and \mathbf{J} are the same images and the local and global irregularity indices are zero. Therefore, for both cases we have $\Phi_p^l(\mathbf{I}, \mathbf{J}) \leq \Phi_p^g(\mathbf{I}, \mathbf{J})$.

More precisely, we have the following theorem:

Theorem 4.1. For any image $\mathbf{I} \in \mathcal{V}$ and $\mathbf{J} = \psi(\mathbf{I})$, we have $\Phi_p^l(\mathbf{I}, \mathbf{J}) \leq \Phi_p^g(\mathbf{I}, \mathbf{J})$.

Proof. First of all, denote respectively the number of pixel values of \mathbf{I} and \mathbf{J} restricted to the local window W_ℓ , for $\ell \in \{1, \dots, k\}$, $i \in \{1, \dots, n\}$, and $j \in \{1, \dots, m\}$ by

$$f_i^\ell = \text{Card}(\{\mathbf{x} \in W_\ell : \mathbf{I}(\mathbf{x}) = v_i\}) \quad \text{and} \quad g_j^\ell = \text{Card}(\{\mathbf{x} \in W_\ell : \mathbf{J}(\mathbf{x}) = u_j\}). \quad (4.5)$$

Note that $f_i^\ell = 0$ and $g_j^\ell = 0$ if the images \mathbf{I} and \mathbf{J} have no pixels with values v_i and u_j in the windows W_ℓ , respectively. Moreover, since $\{W_\ell : \ell = 1, \dots, k\}$ is a partition of the images domain D , the identities

$$\sum_{\ell=1}^k f_i^\ell = f_i \quad \text{and} \quad \sum_{\ell=1}^k g_j^\ell = g_j, \quad (4.6)$$

where $f_i = \text{Card}(\{\mathbf{x} : \mathbf{I}(\mathbf{x}) = v_i\})$ and $g_j = \text{Card}(\{\mathbf{x} : \mathbf{J}(\mathbf{x}) = u_j\})$, hold for all $i = 1, \dots, n$ and $j = 1, \dots, m$. Although in practice we compute $\mathcal{W}_p(\mathbf{I}, \mathbf{J}|W_\ell)$ using only the pixel values of \mathbf{I} and \mathbf{J} in the local window W_ℓ , the restricted Wasserstein metric satisfies

$$(\mathcal{W}_p(\mathbf{I}, \mathbf{J}|W_\ell))^p = \sum_{i=1}^n \sum_{j=1}^m c_{ij} x_{ij}^\ell, \quad (4.7)$$

where x_{ij}^ℓ solves the linear programming problem

$$\begin{cases} \text{minimize} & \sum_{i=1}^n \sum_{j=1}^m c_{ij} x_{ij}^\ell \\ \text{subject to} & \sum_{j=1}^m x_{ij}^\ell = f_i^\ell, \quad \sum_{i=1}^n x_{ij}^\ell = g_j^\ell, \quad \text{and} \quad x_{ij}^\ell \geq 0, \quad \forall i, \forall j. \end{cases} \quad (4.8)$$

Now, define the non-negative variables

$$z_{ij} = \sum_{\ell=1}^k x_{ij}^\ell, \quad \forall i = 1, \dots, n \text{ and } \forall j = 1, \dots, m. \quad (4.9)$$

From (4.6), we conclude that

$$\sum_{j=1}^m z_{ij} = \sum_{j=1}^m \sum_{\ell=1}^k x_{ij}^\ell = \sum_{\ell=1}^k f_i^\ell = f_i \quad \text{and} \quad \sum_{i=1}^n z_{ij} = \sum_{\ell=1}^k g_j^\ell = g_j. \quad (4.10)$$

Thus, the variables z_{ij} satisfies the constraints of the linear programming problem (3.3). Because $(\mathcal{W}_p(\mathbf{I}, \mathbf{J}))^p$ is the minimum value of (3.3), from (4.7) we conclude that

$$(\mathcal{W}_p(\mathbf{I}, \mathbf{J}))^p \leq \sum_{i=1}^n \sum_{j=1}^m c_{ij} z_{ij} = \sum_{\ell=1}^k \sum_{i=1}^n \sum_{j=1}^m c_{ij} x_{ij}^\ell = \sum_{\ell=1}^k (\mathcal{W}_p(\mathbf{I}, \mathbf{J}|W_\ell))^p, \quad (4.11)$$

which results the desired inequality

$$\Phi_p^g(\mathbf{I}, \mathbf{J}) = 1 - \frac{\mathcal{W}_p(\mathbf{I}, \mathbf{J})}{\mathcal{D}_p(\mathbf{I}, \mathbf{J})} \geq 1 - \frac{(\sum_{\ell=1}^k \mathcal{W}_p(\mathbf{I}, \mathbf{J}|W_\ell))^{\frac{1}{p}}}{\mathcal{D}_p(\mathbf{I}, \mathbf{J})} = \Phi_p^l(\mathbf{I}, \mathbf{J}), \quad (4.12)$$

for all $\mathbf{I} \in \mathcal{V}$ and $\mathbf{J} = \psi(\mathbf{I})$. ■

4.2 Computational Analysis of Natural Color Images

Similar to Section 3.2, let us conduct some computational experiments using natural color images. However, instead of calculating the global irregularity measure Φ_1^g for small color images from the CIFAR-10 dataset, we compute the local irregularity measure Φ_1^l for morphological operators applied on one hundred color images from the Berkeley segmentation dataset (BSDS)¹.

First of all, we use the Berkeley segmentation dataset because the images are bigger than the images on the CIFAR-10 dataset, with 481×321 and 321×481 pixels, and it is not feasible to obtain the global irregularity index for such images. According to [Martin *et al.* \(2001\)](#), they initially had the BSDS300 dataset, which contains 200 training images and 100 testing images. After that, they have updated the BSDS300 dataset by adding 200 new testing images obtaining the BSDS500 dataset. The BSDS300 and BSDS500 datasets have found wide acceptance as benchmarks for evaluating different segmentation algorithms. We can see that all the testing images encompass a wide variety of geographic features, objects, people, plants, and animals.

The local irregularity index has been computed using dilations, erosions, openings, and closings by a 9×9 square structuring element S . Precisely, we evaluated the local irregularity index on 25 dilations, 25 erosions, 25 openings, and 25 closings. Additionally, we considered five morphological approaches, namely, the marginal, Loewner, lexicographical RGB, supervised SVM-based, and the projection depth approaches. Note that these are the same morphological approaches we used in Chapter 3. Moreover, we used the Euclidean distance as the metric in the RGB color space with $p = 1$ and local windows of size 16×16 . The boxplot shown in Figure 4.1 summarizes the outcome of this computational experiment.

As seen in Figure 4.1, the methods utilizing partial orderings (marginal and Loewner) resulted in the lowest local irregularity indexes. Conversely, the approaches based on total orderings generated the highest irregularity indexes. Through the Wilcoxon signed-rank test with a confidence level of 99%, we established that the local irregularity indexes were ranked in ascending order like the global irregularity index by the marginal, Loewner, lexicographical RGB, supervised SVM-based, and the projection depth approaches.

Examples of images produced by morphological operators along with their corresponding local irregularity index can be found in Figures 4.2 to 4.5. Specifically, Figure 4.2 displays the original color image and the dilated images. The local irregularity index, computed using windows of size 16×16 , can be found above the dilated images. It is interesting to note that in all approaches, the white color overlaps with the black color in the dilation. Note that the black bands on the heads of the people diminish in the dilated images. Furthermore, as we expected,

¹ The program code of the local irregularity index is located at <https://github.com/mevalle/Irregularity-Index>.

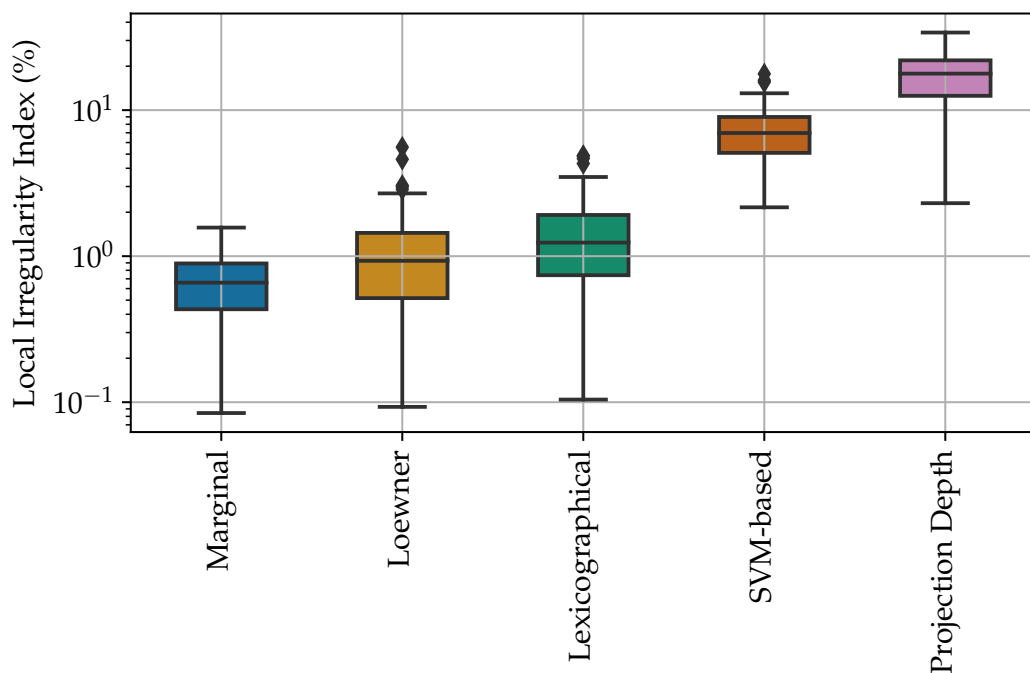


Figure 4.1 – Presentation of the local irregularity index distribution of 100 color images for 5 morphological approaches.

the SVM-based and projection depth approaches resulted in the highest local irregularity indexes. In contrast, the marginal and Loewner approaches generated the lowest local irregularity indexes. It is worth mentioning that the value of 2.31% is an outlier, which corresponds to the smallest local irregularity index produced by the projection depth approach on the one hundred natural color images in this computational experiment. It is noteworthy that the outcomes were similar to those determined in the global irregularity measure, and that for this displayed figure, we have the local irregularity value of the SVM approach higher than the projection depth approach with the value of 5.93%. This shows that the values can vary with the spectrum of the image. However, statistically, it is apparent that the projection depth approach often yields higher values than the other approaches.

Analogously, Figure 4.3 illustrates an original color image and the related eroded images. If we look at the results obtained in the marginal, Loewner and lexicographical approaches, it has no significant differences from one image to another. This also shows in our calculation of the local irregularity index, since local irregularity index is less than 1.00% in the three approaches. As observed, the SVM-based and projection depth approaches again yielded the most significant local irregularity indexes. Additionally, in contrast to the outlier irregularity value observed in the dilated image presented in Figure 4.2, the eroded image in Figure 4.3 is a typical image produced by the projection depth approach on the one hundred natural images considered in this experiment. Other typical images produced by the five morphological approaches are also shown in Figures 4.4 and 4.5. These figures show an original image and the corresponding openings and closings, respectively. Precisely, Figure 4.4 shows a fleet of boats on a sea, and it



Figure 4.2 – Dilated image and local irregularity index using 5 approaches.

can be seen that the local irregularity indices of the marginal and Loewner approaches remain close. The local irregularity index in lexicographical approach is 4.31%, but it is still lower than the indices produced by the SVM and projection depth based approaches. Figure 4.5 shows a girl sitting with a basket and once again we have that the marginal and Loewner approaches have the lowest local irregularity indices, with values of 0.76% and 0.98%, respectively. Finally, we emphasize that the total order that comes closest to the indices obtained from the partial orders was the lexicographic order with a local irregularity index of 1.78%.

To wrap up this section, we want to highlight the striking resemblance between the boxplots in Figures 3.4 and 4.1. Both the global and local irregularity metrics effectively capture the visual irregularity caused by morphological operators, with only a slight difference in scale. Additionally, while the local irregularity measure provides a lower bound for the global

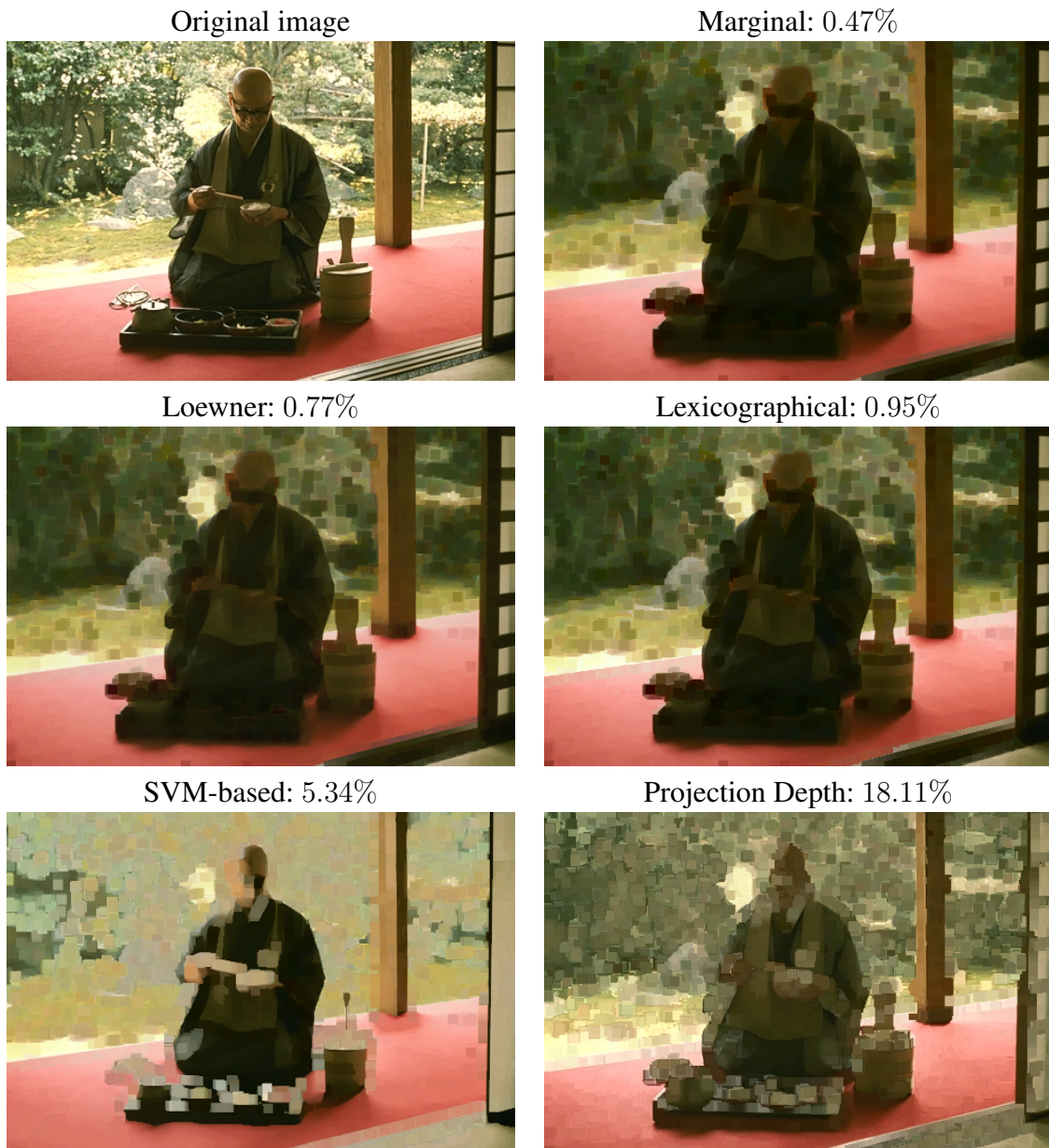


Figure 4.3 – Eroded image and local irregularity index using 5 approaches.

irregularity index, we recommend using it for assessing the irregularity issue of multivariate morphological operators.

4.3 Computing the Wasserstein Metric with Entropic Regularization

To calculate the local irregularity index, for each local window W_ℓ , we compute the Wasserstein metric $\mathcal{W}_p(\mathbf{I}, \mathbf{J} | W_\ell)$. Due to the computational cost for computing the Wasserstein metric, it takes time to calculate the local irregularity index between two natural color images. Thus, it is natural to discuss whether there are computational methods that enable a shorter time

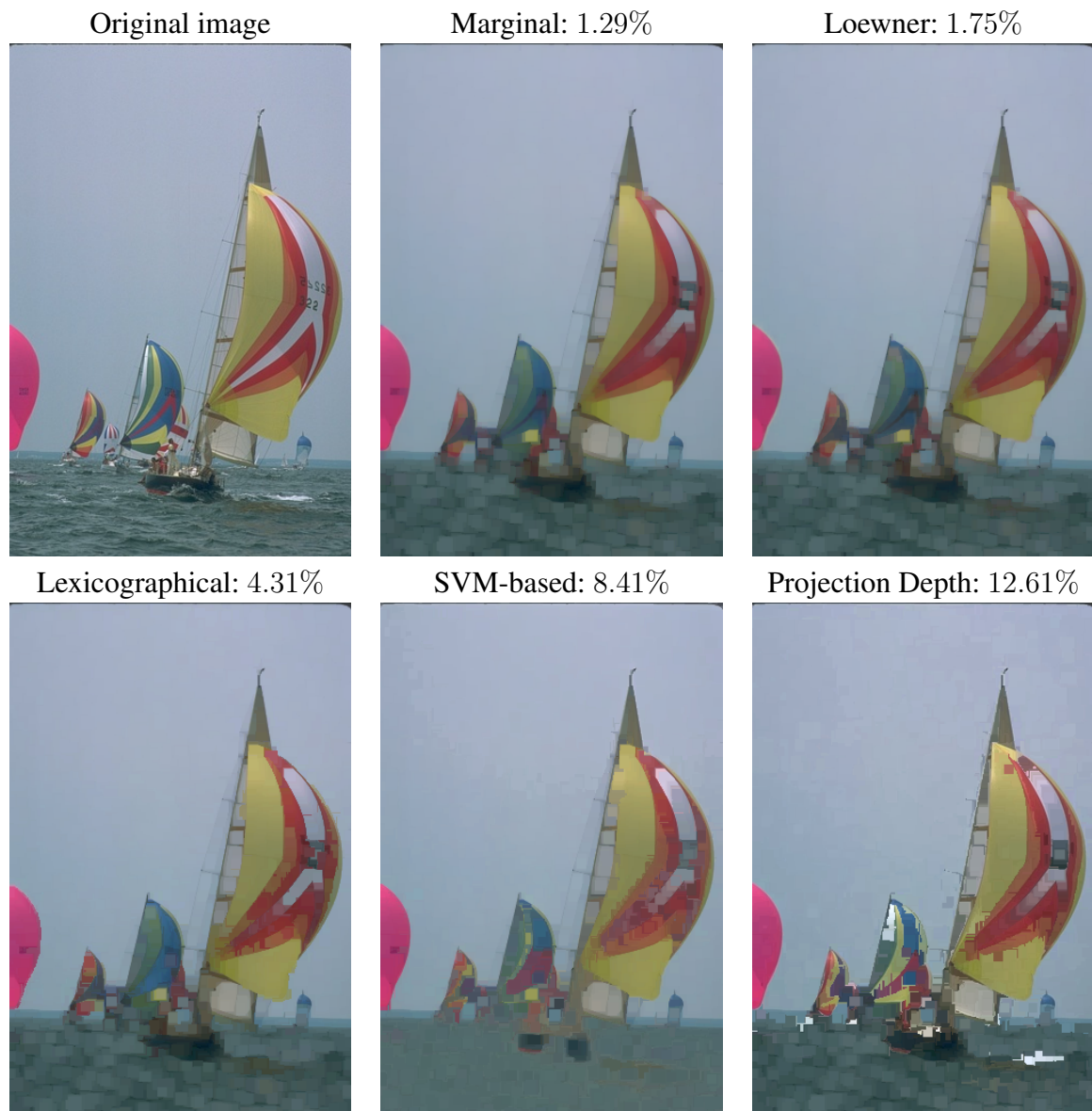


Figure 4.4 – Opened image and local irregularity index using 5 approaches.

interval in the calculation of the irregularity.

Entropic regularization is a technique that has been widely studied and utilized for solving optimal transport problems, as it allows for stable and efficient solutions in terms of computation time. Sinkhorn methods, for instance, are a class of algorithms based on entropic regularization that have proven effective in solving this type of problem, due to their ability to quickly converge to optimal solutions.

The study of entropic regularization in transportation problem and linear programming began with [Schrödinger \(1931\)](#), continued with [Wilson \(1969\)](#), and [Cominetti & Martín \(1994\)](#). However, it became more widely known in the field of machine learning with the paper by [Cuturi \(2013\)](#). This paper showed the potential of Sinkhorn-Knopp algorithm or simply Sinkhorn algorithm in achieving significant computational speed-up in these problems. The Sinkhorn



Figure 4.5 – Closed image and local irregularity index using 5 approaches.

algorithm is a powerful method for solving entropic regularized transportation problems. It was first proposed by [Sinkhorn \(1964\)](#) and further developed by [Sinkhorn & Knopp \(1967\)](#).

Despite being studied for several decades, there is still a lot of ongoing research in entropic optimal transport, particularly in the areas of numerical methods, theoretical properties, and a wide range of applications. Entropic regularization has been applied in many fields such as probability theory, statistical physics, and various areas of engineering and pure mathematics. The wide range of applications makes it a versatile and powerful tool for solving complex optimization problems.

The general formulation of the optimal transport problem with the use of entropy is described as follow.

Given two probability measures μ and ν defined on Polish metric spaces X and Y ,

respectively, and a cost function $c : X \times Y \rightarrow \mathbb{R}$, the entropic regularized transport problem consists in finding the probability measures π in the set $\Pi(\mu, \nu)$ of Borel probability measures on $X \times Y$ that has marginals distributions μ and ν and minimizes the following objective function

$$\inf_{\pi \in \Pi(\mu, \nu)} \int_{X \times Y} c(x, y) d\pi(x, y) + \epsilon H(\pi | \mu \otimes \nu), \quad (4.13)$$

where ϵ is a positive regularization parameter and $H(\cdot | \mu \otimes \nu)$ denotes the relative entropy with respect to the product measure $\mu \otimes \nu$ (Peyré & Cuturi, 2019).

The entropy regularized method adds an entropic regularization penalty to the original problem. With this regularization we have several advantages. One is that the solution of the regularized problem converges to the solution of the transport problem at a lower computational cost.

In the discrete case, the entropic regularized transport problem can also be formulated by working with histograms or discrete probability distributions, in contrast to working with probability measures defined on metric spaces. In this case, π is a matrix of size $n \times m$, i.e., $\pi = \mathbf{X} = (x_{ij}) \in [0, 1]^{n \times m}$, μ and ν are probability vectors of size n and m , respectively, and c is a matrix of size $n \times m$. According to Peyré & Cuturi (2019), the discrete entropy of a coupling matrix \mathbf{X} is defined as

$$H(\mathbf{X}) = - \sum_{i=1}^n \sum_{j=1}^m x_{ij} (\log x_{ij} - 1). \quad (4.14)$$

It should be pointed out that the function H in (4.14) is 1-strongly concave, as its Hessian satisfies $\partial^2 H(\mathbf{X}) = -\text{diag}(1/x_{ij})$ and all elements in the matrix \mathbf{X} are less than or equal to 1. This indicates that the Hessian is negative definite, resulting in a 1-strongly concave function. Therefore, by using entropic regularization in the transport problem considering $-H$ as a regularizing function and $\epsilon > 0$ as the regularization term, we obtain an ϵ -strongly convex objective function, guaranteeing the existence of a unique optimal solution. In other words, we have the following convex optimization problem

$$\left\{ \begin{array}{l} \text{minimize} \quad \sum_{i=1}^n \sum_{j=1}^m c_{ij} x_{ij} + \epsilon \sum_{i=1}^n \sum_{j=1}^m x_{ij} (\log x_{ij} - 1) \\ \text{subject to} \quad \sum_{j=1}^m x_{ij} = a_i / N_D, \quad \text{for all } i = 1, \dots, n, \\ \quad \quad \quad \sum_{i=1}^n x_{ij} = b_j / N_D, \quad \text{for all } j = 1, \dots, m, \\ \quad \quad \quad x_{ij} \geq 0, \quad \text{for all } i = 1, \dots, n, \text{ and for all } j = 1, \dots, m, \end{array} \right. \quad (4.15)$$

with N_D denoting the quantity of pixels in the operated images.

It is worth mentioning that in order to obtain a significant entropic regularization, the variables x_{ij} must comply with the condition $\sum_{i=1}^n \sum_{j=1}^m x_{ij} = (1/N_D) \sum_{i=1}^n a_i = (1/N_D) \sum_{j=1}^m b_j = 1$.

The Wasserstein metric is then approximated by

$$\mathcal{W}_p^r(\mathbf{I}, \mathbf{J}) = \left(N_D \sum_{i=1}^n \sum_{j=1}^m c_{ij} x_{ij} \right)^{1/p}, \quad p \geq 1, \quad (4.16)$$

where x_{ij} solves (4.15). It is worth mentioning that the approximation \mathcal{W}_p^r is not taking into account the regularization term. As both (3.3) and (4.15) have the same constraints, the inequality $W_p(\mathbf{I}, \mathbf{J}) \leq \mathcal{W}_p^r(\mathbf{I}, \mathbf{J})$ holds for all images \mathbf{I} and $\mathbf{J} = \psi(\mathbf{I})$. Therefore, the irregularity index calculated by an entropic regularized method also produces a lower bound for the analytical irregularity index.

As verified in Peyré & Cuturi (2019), the optimal solution for the regularized optimal transport problem can be calculated using the Sinkhorn method, which is an iterative algorithm. This method relies only on matrix-vector multiplication operations, which makes it very efficient and suitable to run on graphics processing units (GPUs). This means that Sinkhorn's algorithm is able to obtain the optimal solution quickly, especially when dealing with large datasets, due to the parallel processing capability of GPUs. The process of Sinkhorn's algorithm comes from the fact that the solution of (4.15) is unique and has the form

$$x_{ij} = u_i \mathbf{K}_{ij} v_j, \quad \forall i = \{1, 2, \dots, n\} \text{ and } \forall j = \{1, 2, \dots, m\}, \quad (4.17)$$

for two unknown scaling variable $(\mathbf{u}, \mathbf{v}) \in \mathbb{R}_+^n \times \mathbb{R}_+^m$, where \mathbf{K}_{ij} is the Gibbs kernel for Sinkhorn and is defined by $\mathbf{K}_{ij} = \exp(-c_{ij}/\epsilon)$.

In fact, the solution to the convex optimization problem (4.15) can be solved in a similar manner as we did for the optimization problem (2.11) by taking the partial derivative of the Lagrangian with respect to x_{ij} and setting it equal to zero. In this case, the result is

$$\frac{\partial \mathcal{L}}{\partial x_{ij}}(\mathbf{X}, \alpha, \lambda) = c_{ij} + \epsilon \log x_{ij} - \alpha_i - \lambda_j = 0, \quad (4.18)$$

where α_i and λ_j are the Lagrange multipliers.

From (4.18), $\log x_{ij} = \frac{\alpha_i}{\epsilon} - \frac{c_{ij}}{\epsilon} + \frac{\lambda_j}{\epsilon}$, which in turn leads to

$$x_{ij} = \exp(\alpha_i/\epsilon) \exp(-c_{ij}/\epsilon) \exp(\lambda_j/\epsilon), \quad (4.19)$$

for all $i = \{1, 2, \dots, n\}$ and for all $j = \{1, 2, \dots, m\}$ as desired.

It should be noted that we can express the factorization of the optimal solution shown in Equation (4.17) as $\mathbf{X} = \text{diag}(\mathbf{u})\mathbf{K}\text{diag}(\mathbf{v})$, where $\text{diag}(\mathbf{u})$ and $\text{diag}(\mathbf{v})$ represents the $n \times n$ matrix with \mathbf{u} on the diagonal and zero otherwise and the $m \times m$ matrix with diagonal \mathbf{v} and zero otherwise, respectively. Therefore, we have

$$\text{diag}(\mathbf{u})\mathbf{K}\text{diag}(\mathbf{v})\mathbf{1}_m = \mathbf{a} \text{ and } \text{diag}(\mathbf{v})\mathbf{K}^t\text{diag}(\mathbf{u})\mathbf{1}_n = \mathbf{b}. \quad (4.20)$$

From (4.20) we have that $\mathbf{u} \odot (\mathbf{K}\mathbf{v}) = \mathbf{a}$ and $\mathbf{v} \odot (\mathbf{K}^t\mathbf{u}) = \mathbf{b}$, where \odot denote the Hadamard product, also known as the Schur product or element-wise product. A practical method

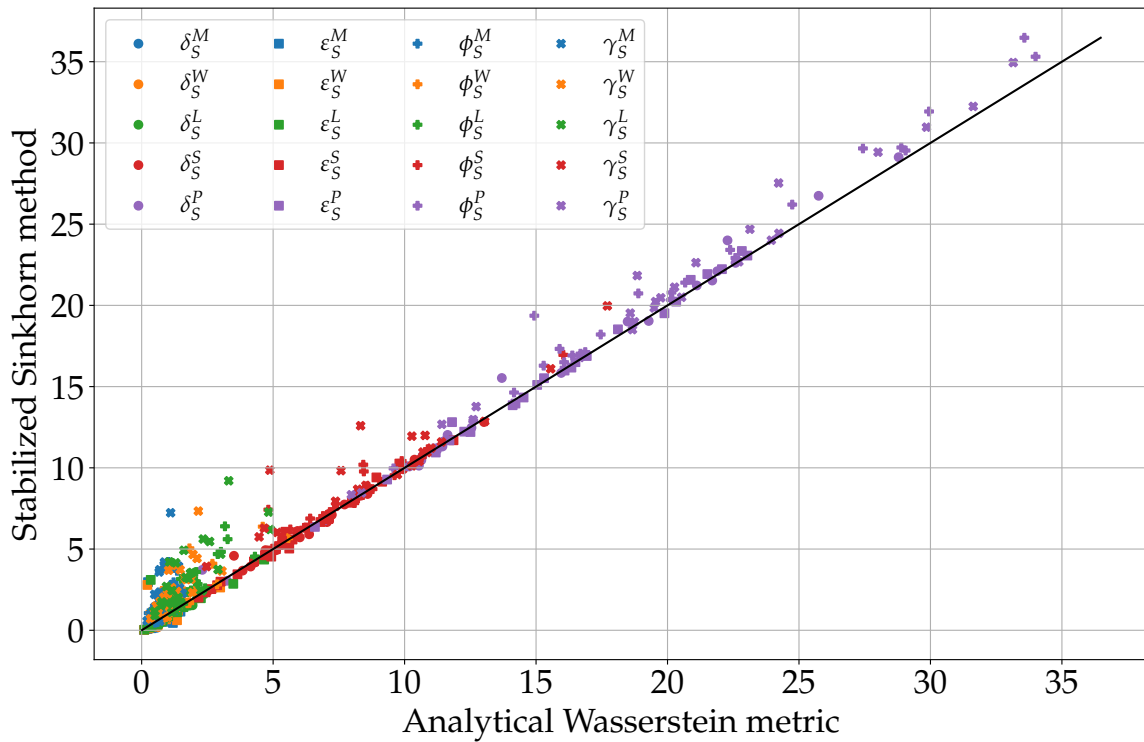


Figure 4.6 – Relation of local irregularity measure by the two methods.

for tackling these equations is through iterative solution. This process is known as Sinkhorn’s algorithm, with updates

$$\mathbf{u}^{k+1} = \frac{\mathbf{a}}{\mathbf{K}\mathbf{v}^k} \text{ and } \mathbf{v}^{k+1} = \frac{\mathbf{b}}{\mathbf{K}^t\mathbf{u}^{k+1}}, \quad (4.21)$$

using an arbitrary positive vector such as $\mathbf{v}^0 = \mathbf{1}_m$.

It should be emphasized that the division operator applied between two vectors in (4.21) is commonly referred to as element-wise division, and this issue is widely known in the numerical analysis field as the matrix scaling problem (Nemirovski & Rothblum, 1999).

Concluding, the Sinkhorn algorithm is very efficient for solving the problem (4.15). It is important to note that the algorithm converges to the analytical solution when ϵ tends to zero. Unfortunately, as the entropic term approaches zero, the convergence of the Sinkhorn method decreases. For small values of ϵ , the regularized optimization problem defined in (4.15) can be efficiently solved using stabilized versions of the Sinkhorn method, as outlined by Schmitzer (2019). These stabilized versions are implemented in popular optimal transport libraries like Python Optimal Transport² (POT) and Julia’s Optimal Transport³.

The scatter plot in Figure 4.6 presents a comparison of local irregularity measure utilizing both techniques discussed in this thesis, the analytical Wasserstein metric and the stabilized Sinkhorn method with regularization, which aims to approximate the Wasserstein

² <https://optimaltransport.github.io/>

³ <https://github.com/JuliaOptimalTransport/OptimalTransport.jl>

metric. The graph displays the irregularity index calculated using 16×16 local windows, $p = 1$, and the Euclidean metric, on a selection of the Berkeley segmentation dataset (BSDS).

Along the same lines as the previous experiments, we considered dilations (δ_S), erosions (ε_S), openings (γ_S), and closings (ϕ_S) by a 9×9 square structuring element S . Additionally, we considered the marginal, Loewner, lexicographical, SVM-based, and projection depth approaches. The five morphological approaches were identified by the superindexes M , W , L , S , and P , respectively.

The scatter plot in Figure 4.6 displays the local irregularity index, with the horizontal axis representing the analytical method and the vertical axis representing the stabilized Sinkhorn method. In this experiment, the regularization term ϵ was set to 10^{-3} .

The line $y = x$ is also illustrated in Figure 4.6. Points that are closer to this line indicate a better approximation of the analytical solution by the stabilized Sinkhorn method. The coefficient of determination of the 500 points is $R^2 = 0.98$, showing that the stabilized Sinkhorn method produced accurate estimations of the analytical local irregularity index when using local windows of size 16×16 .

In addition, the stabilized Sinkhorn method is computationally much more efficient than the analytical Wasserstein metric when calculating the local irregularity index. For this reason, we recommend using the Sinkhorn method or its variations to compute the local irregularity index. It is worth noting that alternative methods such as sliced approximations and Nesterov smoothing of the optimal transport problem can also be used to estimate the irregularity index (Pitié *et al.*, 2005; Nesterov, 2005).

4.4 Effect of Structuring Element and Window Size on the Irregularity Measure

We know that given an image \mathbf{I} , the image $\mathbf{J} = \psi(\mathbf{I})$ obtained via a morphological operator depends on the size of the structuring element S . Consequently, we can analyze whether the size of the structuring element has a relationship with the local irregularity index.

Furthermore, to calculate the local irregularity index, we use k local windows W_i with $i \in \{1, 2, \dots, k\}$. The number of local windows is related to their sizes. In this way, we can analyze whether the variation of the size of the local windows has a relationship with the local irregularity index.

Figure 4.7 illustrates the median of the local irregularity index as it relates to the size of the structuring element, computed using four different local window sizes. The area between the first and third quartiles is also illustrated. To obtain the results, we applied 25 dilations, erosions, openings, and closings using square structuring elements of sizes $3 \times 3, 5 \times 5, \dots, 25 \times 25$ using the marginal, lexicographical RGB, SVM-based, and projection depth approaches.

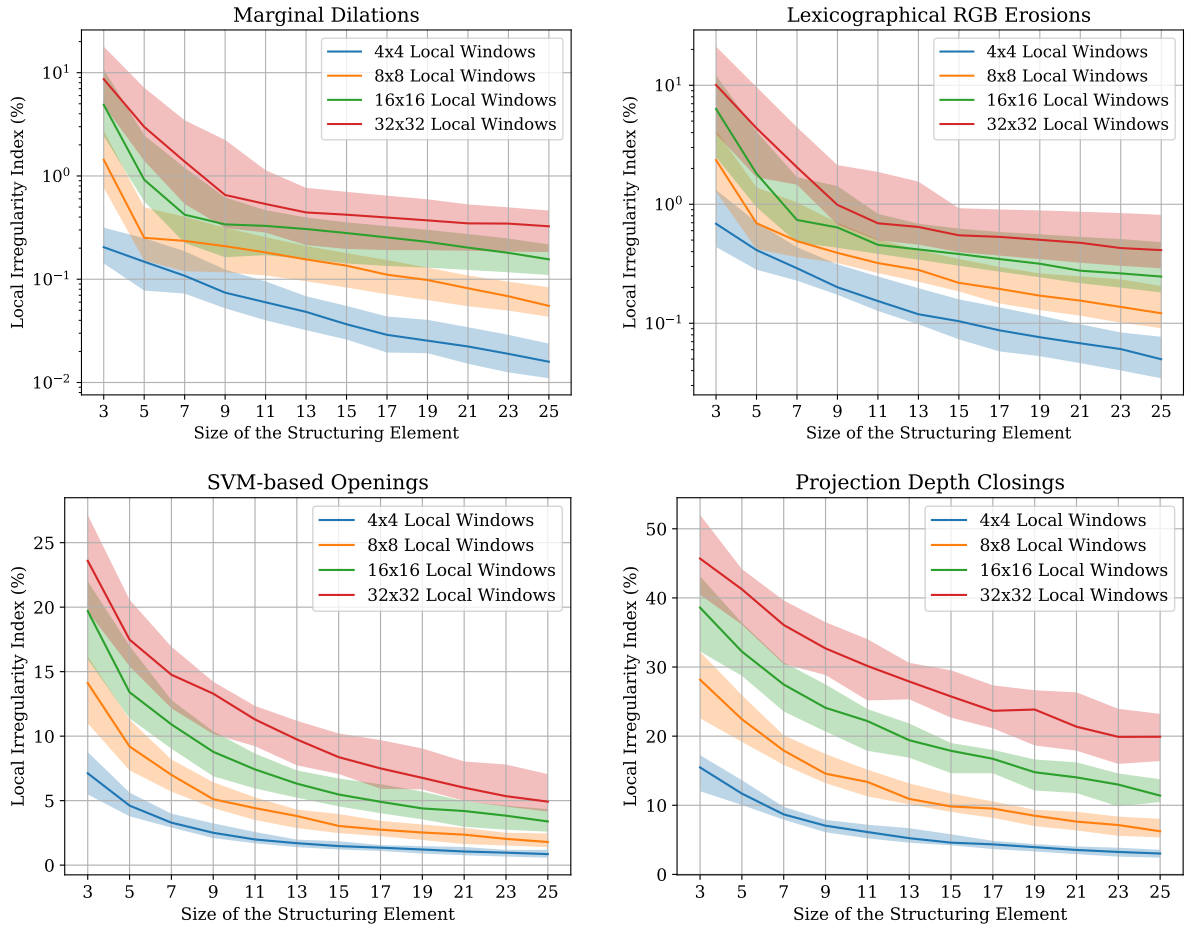


Figure 4.7 – Plot of the local irregularity measure based on the structuring element size. The shaded area represents the first and third quartiles.

Then, we calculated the local irregularity index utilizing the stabilized Sinkhorn method with a regularization term $\epsilon = 10^{-3}$ and local windows of sizes 4×4 , 8×8 , 16×16 , and 32×32 .

The local irregularity index seen in Figure 4.7 decreases as the size of the structuring element increases, regardless of the size of the local window used. Additionally, there is no discernible correlation between the size of the local window and the structuring element. It can be observed that the size of the local window does not need to be larger or smaller than the structuring element.

Furthermore, it can be observed that the local irregularity index increases with the size of the local windows. Despite the variations in the median of the local irregularity index, the range between the first and third quartiles overlaps for local windows of size 16×16 and 32×32 for certain approaches. This suggests that the local irregularity index should approach the global irregularity index as the size of the local windows increases. This is in accordance with Theorem 4.1, where we proved that the local irregularity index Φ_p^l is less than or equal to the global irregularity index Φ_p^g , that is, for all images $\mathbf{I}, \mathbf{J} = \psi(\mathbf{I}) \in \mathcal{V}$, we have $\Phi_p^l(\mathbf{I}, \mathbf{J}) \leq \Phi_p^g(\mathbf{I}, \mathbf{J})$. Ultimately, while there is a trade-off between computational cost and approximating the global irregularity index, using fixed local windows can provide a reliable method for comparing the

irregularity of different morphological operators or approaches.

4.5 Remarks of Execution Time

In this section, we briefly present the computational results obtained by implementing the local irregularity index algorithm proposed in this chapter in Julia language. All experiments were performed on a machine with the following specifications:

- Operating System: Windows 10 Home Single Language (version 22H2)
- Processor: 11th Gen Intel(R) Core(TM) i7-1165G7, 4.70 GHz, 4 cores
- Memory RAM: 16 GB 3200 MHz DDR4

Our computational experiments were performed with images of size 481×321 or 321×481 from the Berkeley dataset. The running time was calculated using Julia's `@time` function and represents the total CPU time spent by the algorithm to process the input.

To analyze the efficiency of the algorithm, we measured the average running time on different input sizes applied in different images. In our context, the input sizes refer to the considered local window size. In this scenario, we used local windows of sizes 4×4 , 8×8 , 16×16 , and 32×32 . The results are displayed in Table 4.1.

Method	Size of Local Window	Execution Time (seconds)
Analytical Wasserstein	4×4	11.56
Analytical Wasserstein	8×8	20.69
Analytical Wasserstein	16×16	124.38
Analytical Wasserstein	32×32	854.85
Stabilized Sinkhorn	4×4	0.95
Stabilized Sinkhorn	8×8	1.78
Stabilized Sinkhorn	16×16	12.19
Stabilized Sinkhorn	32×32	25.41

Table 4.1 – Runtime results for calculate the local irregularity index by analytical Wasserstein metric and stabilized Sinkhorn method.

As discussed in Chapter 3, we have the complexity $\mathcal{O}(n^3 m^3 \log(nm))$ (Pitié, 2020), which is in line with the theory and the results obtained. It is observed that, in the computational experiments carried out, the problem starts to become intractable in polynomial time for local windows larger than 64×64 .

Furthermore, we verified the computational efficiency of the stabilized Sinkhorn method against the analytical Wasserstein metric. This validates the use of the stabilized Sinkhorn method to calculate the irregularity measure in practical scenarios.

THE DIFFICULTY OF OBTAINING A TOTAL ORDER THAT MINIMIZES IRREGULARITY

In Chapters 3 and 4 we discussed ways to calculate the irregularity between an image $\mathbf{I} \in \mathcal{V}$ and an image $\mathbf{J} = \psi(\mathbf{I})$. Furthermore, we performed computational experiments to measure the irregularity between two images \mathbf{I} and $\mathbf{J} = \psi(\mathbf{I})$ involving partial and total orders.

The motivation behind writing this chapter arises from the necessity to explore the inherent difficulty in finding a total order \leq that minimizes the irregularity between two images \mathbf{I} and $\mathbf{J} = \psi(\mathbf{I})$. Although we have discussed the relationship between partial order and total order concerning irregularity computation in previous chapters, the problem of finding the total order that minimizes irregularity remains challenging and complex.

One of the fundamental reasons that make this problem complex is the vast number of possible total orders. In fact, the number of viable total orders is on the order of n factorial, where n represents the size of the element set in each image. Specifically, for an image with n elements, the number of possible total orders is $n!$. With an explosion of possibilities, implying an exponential task to find an order that minimizes the irregularity.

This complexity implies that as the number of elements in the image increases, the number of computations required to find the total order that minimizes irregularity grows rapidly and becomes impractical. To resolve this problem, it would be necessary to explore efficient strategies and approximate methods to deal with the high computational cost. It is essential to remember that this type of problem belongs to the category of NP-hard problems, which means that there are no known algorithms that can solve them in polynomial time.

Another point to consider is that, while there exists a total order that minimizes irregularity between the two images, there is no guarantee that this order is unique. In fact, there may be multiple total orders that satisfy this condition. For example, for an image \mathbf{I} , there could exist two different orders, \leq_1 and \leq_2 , such that the computation of irregularity between images \mathbf{I} and \mathbf{J}_1 and between \mathbf{I} and \mathbf{J}_2 obtained using these respective orders results in the same value. In this sense, there are motivations to discuss, in this chapter, the difficulty of obtaining a total order that indeed minimizes irregularity.

In particular, we start by discussing a total order based on the stochastic permutation ordering given by [Lézoray \(2017\)](#); [Lézoray \(2021\)](#). His approach yields a permutation P on the indices of the image \mathbf{I} in order to form a Hamiltonian path that attempts to minimize the distance between the image values of two consecutive points of this path. This approach is equivalent to obtaining a solution to the traveling salesman problem (TSP). Because of this, we have developed two other total orders based on the traveling salesman problem (TSP) approach and one approach involving Kohonen's self-organizing maps (SOM).

5.1 The Permutation Ordering

Considering a multivariate image $\mathbf{I} : D \rightarrow \mathbb{V}$, we denote by $T = [\mathbf{v}_1, \mathbf{v}_2, \dots, \mathbf{v}_n]$ the list of the values of the image \mathbf{I} . [Lézoray \(2017\)](#) proposed the stochastic permutation ordering as a process that enables the creation of a total order, subject to certain probabilistic constraints obtained by the permutation of the elements of T . In essence, the stochastic permutation ordering algorithm starts from a random image pixel and builds a Hamiltonian path. A Hamiltonian path is a path that visits each pixel of the image exactly once.

It is worth mentioning that graph theory presents convenient techniques to study Hamiltonian paths ([West, 2002](#); [Bondy & Murty, 2008](#)). In this way and in our context, we consider the domain D of the image \mathbf{I} as a graph $\mathcal{G} = (V, E)$ where vertices $V = \{v_1, \dots, v_n\}$ correspond to pixels and $E = V \times V$, with the edge $e_{ij} = (v_i, v_j) \in E$ connecting the vertex v_i with the vertex v_j . Thus, a multivariate image \mathbf{I} can be represented as a graph that associates vectors to vertices and is defined by the mapping $\mathbf{I} : \mathcal{G} \rightarrow \mathbb{V} \subset \mathbb{R}^d$, with $d > 1$. To each vertex $v_i \in \mathcal{G}$ is associated a vector $\mathbf{v}_i = \mathbf{I}(v_i)$.

To create a Hamiltonian path, we follow what was proposed by [Lézoray \(2017\)](#) in which he builds a stochastic Hamiltonian path. According to [Lézoray \(2017\)](#), we start with a random pixel $v_1 \in V$, and construct an indexed list $\mathcal{J} = \{v_1, v_2, \dots, v_n\}$. In turn, this list enables us to create a permutation $P = [\mathbf{v}_1, \mathbf{v}_2, \dots, \mathbf{v}_n]$ of the elements of T .

In order to achieve this, we employ the stochastic permutation construction algorithm proposed by [Lézoray \(2017\)](#):

It is important to note that a permutation P of the elements of T can be represented as $\mathbf{P}T$, where \mathbf{P} is a permutation matrix of size $n \times n$. Let σ be a permutation of the index set $I_n = \{1, 2, \dots, n\}$. If $\sigma(i) = j$, then $\mathbf{P}_{ij} = 1$ and $\mathbf{P}_{ij} = 0$ otherwise. The induced permutation is $\mathbf{P}T = [\mathbf{v}_{\sigma^{-1}(1)}, \mathbf{v}_{\sigma^{-1}(2)}, \dots, \mathbf{v}_{\sigma^{-1}(n)}]$ where $(\sigma^{-1} \circ \sigma)$ is the identity.

Furthermore, Algorithm 1 aims to obtain a smooth permutation that takes into account the spatial and spectral constraints of the image. The smoothness of a data set $T =$

Algorithm 1: Stochastic Permutation Construction on a Graph

Input: set of vectors $T = [\mathbf{v}_1, \dots, \mathbf{v}_n]$ and graph \mathcal{G}
Generate a random probability vector $\mathbf{p} = [p_1, p_2, \dots, p_n]$;
Randomly choose an index $j \in I_n = \{1, 2, \dots, n\}$;
Set $\sigma^{-1}(1) = j$;
Set $P = \{\mathbf{v}_{\sigma^{-1}(1)}\}$ and $\mathcal{J} = \{\sigma^{-1}(1)\}$;
for $i = 1$ **to** $n - 1$ **do**
 Let $N(v_{\sigma^{-1}(i)}) = \{k | (v_{\sigma^{-1}(i)}, v_k) \in E\} \setminus \mathcal{J}$;
 if $|N(v_{\sigma^{-1}(i)})| = 1$ **then**
 | $\sigma^{-1}(i + 1) = N(v_{\sigma^{-1}(i)})$;
 else
 if $|N(v_{\sigma^{-1}(i)})| \geq 2$ **then**
 | Find the first v_{j_1} and the second v_{j_2} nearest neighbors of $v_{\sigma^{-1}(i)}$ in $N(v_{\sigma^{-1}(i)})$;
 else
 if $|N(v_{\sigma^{-1}(i)})| = 0$ **then**
 | Find the first v_{j_1} and the second v_{j_2} nearest neighbors of $v_{\sigma^{-1}(i)}$ in $I_n \setminus \mathcal{J}$;
 end
 end
 $q_i = \frac{1}{1 + \exp\left(\frac{\|\mathbf{v}_{\sigma^{-1}(i)} - \mathbf{v}_{j_1}\| - \|\mathbf{v}_{\sigma^{-1}(i)} - \mathbf{v}_{j_2}\|}{\alpha}\right)}$
 If $(q_i < p_{\sigma^{-1}(i)})$ **then** $\sigma^{-1}(i + 1) = j_2$ **and** $\sigma^{-1}(i) = j_1$ **otherwise**
 end
 $P = P \cup \{\mathbf{v}_{\sigma^{-1}(i+1)}\}$;
 $\mathcal{J} = \mathcal{J} \cup \{\sigma^{-1}(i + 1)\}$;
end
Output: ordered set P and associated index list \mathcal{J}

$[\mathbf{v}_1, \mathbf{v}_2, \dots, \mathbf{v}_n]$ can be determined by the Total Variation (TV) of its elements, given by

$$\|T\|_{TV} = \sum_{k=2}^n \|\mathbf{v}_k - \mathbf{v}_{k-1}\| + \|\mathbf{v}_n - \mathbf{v}_1\|. \quad (5.1)$$

Therefore, we seek to find a permutation \mathbf{P} that minimizes (5.1). In conclusion, the optimal permutation can be determined by the solution of

$$\mathbf{P}^* = \arg \min_{\mathbf{P}} \|\mathbf{P}T\|_{TV}. \quad (5.2)$$

This allows us to define an h -order that we called the unsupervised order based on stochastic permutation ordering, which is derived from the h -SPO function defined below.

Definition 5.1 (h -SPO function). Let $\mathbf{I} : \mathcal{G} = (V, E) \rightarrow \mathbb{V}$ be an image with $\text{Card}(V) = n$. Let $P = [\mathbf{v}_1, \mathbf{v}_2, \dots, \mathbf{v}_n]$ be a path obtained by a stochastic permutation ordering on \mathcal{G} . The h -SPO function $h_{SPO} : P \rightarrow I_n$ is defined by

$$h_{SPO}(\mathbf{v}_i) = i, \quad \forall \mathbf{v}_i \in P. \quad (5.3)$$

It should be noted that minimizing (5.1) is equivalent to solving the traveling salesman problem (TSP). Hence, we can consider the h -SPO function as providing us with a Hamiltonian path that serves as a heuristic for solving the TSP.

The traveling salesman problem (TSP) is a well-known problem in computer science that involves finding the shortest possible route that visits a given set of points and returns to the starting point. The problem is called the traveling salesman problem because it can be viewed as a problem faced by a salesman who needs to visit a set of cities in order to make sales. In other words, the traveling salesman problem (TSP) is a technique for finding the shortest Hamiltonian path in a graph.

Karl Menger was an Austrian mathematician who introduced the idea of using graph theory to study the TSP (Menger, 1927). After, the TSP has been studied extensively since the 1950s, and many algorithms have been developed to solve it. The TSP is a classic example of an NP-hard problem, which means informally that it is difficult to solve exactly and that the time required to solve the problem increases exponentially as the number of points increases. Consequently, there are many different techniques that can be used to solve the TSP, including exact algorithms, approximation algorithms, and heuristics.

The brute force algorithm is a well-known TSP exact algorithm, which is presented for didactic purposes because it is impracticable to use for a large number of points. It involves checking all possible routes to find the shortest one. The approximation algorithms do not necessarily find the optimal solution, but they can provide a solution that is close to optimal in a reasonable amount of time. One example of an approximation algorithm is the Christofides algorithm, which guarantees to find a solution that is at most 1.5 times the length of the optimal tour (Christofides, 1976). The heuristics techniques use a set of rules or guidelines to quickly find a solution that is likely to be good, without necessarily finding the optimal solution. Examples of heuristics for the traveling salesman problem include the nearest insertion algorithm and the farthest insertion algorithm (Applegate *et al.*, 2011).

The TSP continues to be an active area of research, and new algorithms and approaches are constantly being developed to improve the performance and accuracy of solutions. The problem remains a challenging area of study, and it continues to have many practical applications in fields such as mathematics, computer science, and operation research.

In addition to the stochastic permutation ordering obtained through a greedy Hamiltonian path given by L  zoray (2017), there are other works on obtaining permutation orderings. For example, the authors Veganzones *et al.* (2015) proposed an order of permutation from a binary partition tree created in the image. Here, we present an order of permutation obtained by a Hamiltonian path that is constructed by solving the traveling salesman problem (TSP) that is called the h -TSP function.

Definition 5.2 (h -TSP function). Let $\mathbf{I} : \mathcal{G} = (V, E) \rightarrow \mathbb{V}$ be an image with $\text{Card}(V) = n$. Let

$P = [v_1, v_2, \dots, v_n]$ be a path obtained by solving the traveling salesman problem (TSP) on \mathcal{G} . The h -TSP function $h_{TSP} : P \rightarrow I_n$ is defined by

$$h_{TSP}(v_i) = i, \quad \forall v_i \in P. \quad (5.4)$$

An important consideration is that the list $P = [v_1, \dots, v_n]$ obtained in Definitions 5.1 and 5.2 has a cyclic property. This means that regardless of the starting point in P , whether it is v_1 or v_i , for any $i \in \{2, 3, \dots, n\}$, the sum of the path remains the same. In other words, P can be traversed in a cyclic manner, as it forms a closed loop, returning to the starting point after visiting all the vertices once. This cyclic property is a crucial feature of P , as it enables the path to be explored from any starting point, without affecting the final result.

Therefore, if $P = [v_1, \dots, v_n]$ with $v_1 \leq v_2 \leq \dots \leq v_n$, is a Hamiltonian path that solves the TSP problem, the path $P' = [v_i, v_{i+1}, \dots, v_n, v_1, v_2, \dots, v_{i-1}]$, for some $i \in \{2, 3, \dots, n\}$, with $v_i \leq' v_{i+1} \leq' \dots \leq' v_n \leq' v_1 \leq' \dots \leq' v_{i-1}$, also provides a Hamiltonian path that solves the TSP problem. However, it is observed that P and P' give us two distinct total orders and therefore imply different irregularities.

For example, in Figure 5.1 we show a toy image with 10×5 pixels with only 3 colors: pure black, pure blue, and gray corresponding in the RGB cube to the points $\mathbf{a} = (0, 0, 0)$, $\mathbf{b} = (0, 0, 1)$, and $\mathbf{c} = (0.27, 0.27, 0.27)$. The blue colors are in the last two columns of the image and the gray colors are in positions (3, 3) and (7, 3). The SPO image is the dilation by a cross structuring element equipped with stochastic permutation ordering. The two last images are the dilation by a cross structuring element with the TSP approach. The difference between the two images is that the TSP 1 image utilized a total order \leq obtained through the computer-generated Hamiltonian path construction for the TSP solution, while the TSP 2 image was obtained by a total order \leq' in which the Hamiltonian path used was the same as the previous one, but with a shift, i.e., a translation to address the cyclic problem. Furthermore, the direction in which we traverse the Hamiltonian path yields different orders. Specifically, the order obtained by traversing from left to right is dual to the order obtained by traversing from right to left, as seen in Definition 2.4. The global irregularities between the toy image and the SPO image, TSP 1 image, and TSP 2 image are 57.88%, 52.41%, and 9.12%, respectively.

Additionally, Figure 5.2 shows the color spectra of the path obtained using SPO, TSP 1, and TSP 2, arranged from left to right based on the total order criteria via Definitions 5.1 and 5.2. Figure 5.3 shows the Hamiltonian path on the graph \mathcal{G} of the toy image domain for both the stochastic permutation ordering and the ordering based on the traveling salesman problem (TSP). It is worth noting that the graph obtained by TSP 1 is identical to the graph obtained by TSP 2. The question is only which direction we traverse the Hamiltonian path and at which point we start on the path. For this smooth permutation, we consider a list that starts and ends in values v_1 and v_n such that $d(v_1, v_n) \geq d(v_i, v_{i+1})$ for every $i = 1, \dots, n - 1$. Furthermore, we take

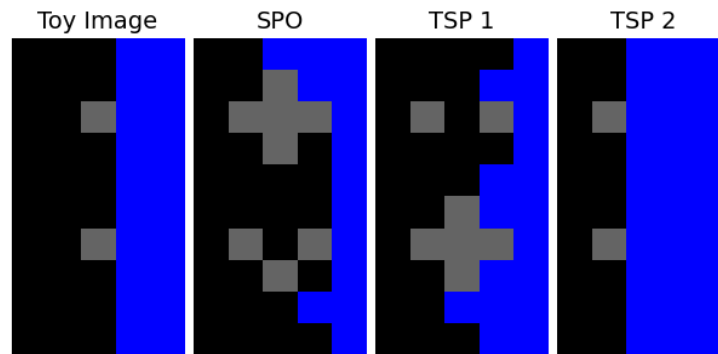


Figure 5.1 – Illustrative example of the dilated images obtained by the SPO and TSP orderings with a cross structuring element. In TSP 1, the Hamiltonian path of the optimal TSP solution is used. In TSP 2, the same path of TSP 1 is used with a translation to address the cyclic problem.

Color Spectrum obtained by the path P on \mathcal{G} in Definition 5.1



Color Spectrum obtained by the path P on \mathcal{G} in Definition 5.2



Color Spectrum obtained by the path P on \mathcal{G} in Definition 5.2 with a shift for solve the cyclic problem



Figure 5.2 – Color spectra obtained of the TSO, TSP 1, and TSP 2 images.

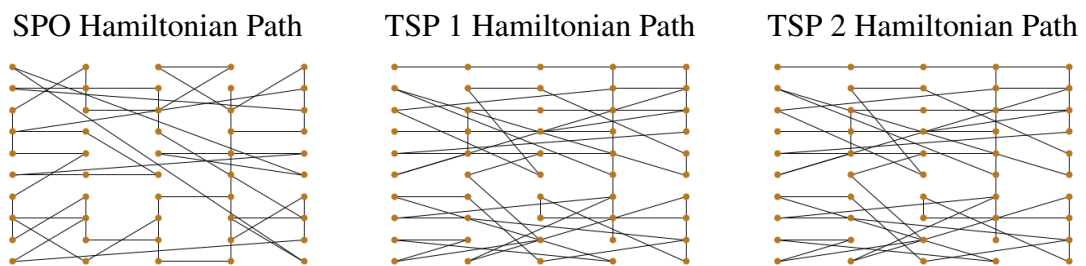


Figure 5.3 – The Hamiltonian paths constructed on graph \mathcal{G} of the toy image.

the first element such that $\|v_1\| \leq \|v_n\|$ ¹.

The dilated image obtained by the stochastic permutation ordering provided the greatest irregularity. This is due to the stochastic process of the algorithm, which traverses the graph \mathcal{G} , it is capable of being at a color value v_i , jumping to a color v_k , and then returning to another color that is close to or equal to v_i . The Hamiltonian path of SPO in Figure 5.3 obtained from the toy image, along with the color spectrum in Figure 5.2, exemplifies this situation. For example, it can be observed that the graph is traversed by some pixel v_i where $\mathbf{I}(v_i) = \mathbf{b}$,

¹ The program code of TSP approach is located at <https://github.com/samuelfsc/TSP-and-SOM-morphological-approach>.

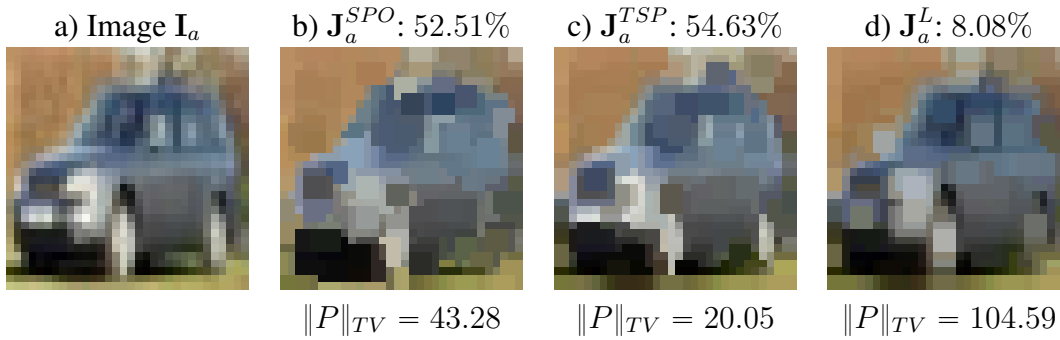


Figure 5.4 – Image \mathbf{I}_a and their morphological openings by stochastic permutation ordering, TSP ordering, and lexicographical ordering, respectively.

then it moves to some pixel v_k such that $\mathbf{I}(v_k) = \mathbf{a}$, and then returns to another some pixel v_j where $\mathbf{I}(v_j) = \mathbf{b}$. Such jump occurs with black and gray colors, as can be noticed in Figure 5.2. These jumps produce irregularity and therefore it is plausible that the total order obtained by the stochastic permutation ordering provides us with high irregularity.

However, we know that the stochastic permutation ordering is a heuristic for solving the TSP and therefore does not provide the optimal Hamiltonian path. In this case, we want to verify if the permutation \mathbf{P} that provides the shortest Hamiltonian path on the graph \mathcal{G} actually gives a lower irregularity. Unfortunately, it is impossible to compute the TSP exactly for the natural images and even the tiny images of the CIFAR-10 dataset. Therefore, it is necessary to use a heuristic approach to find an approximate solution to the problem. We employed two heuristics to solve the TSP problem: the nearest neighbor algorithm and the farthest heuristic. We chose these heuristics because they are both relatively simple to implement and provide good approximate solutions for the TSP in a short amount of time (Adrabiński & Syslo, 1983; Golden *et al.*, 1980; Lin & Kernighan, 1973; Gutin *et al.*, 2002). Subsequently, we utilized the Hamiltonian path that yielded the best result, namely, we selected the shortest path.

The nearest neighbor algorithm is one of the initial algorithms used to solve the traveling salesman problem approximately. In this problem, the salesman starts at a random city and then visits successively the nearest city until all cities have been visited. The algorithm quickly produces a short tour, but it is usually not optimal (Gutin *et al.*, 2002). The farthest insertion heuristic operates by first identifying two pixels, denoted as v_1 and v_2 , from an image such that the distance $d(\mathbf{I}(v_1), \mathbf{I}(v_2))$ is maximized. These two pixels are considered to be part of the graph \mathcal{G} and are connected. Subsequently, in a recursive manner, a new pixel, denoted as v_3 , is selected from all pixels not already included in the path, such that its distance to any pixel already included in the path is maximized. This new pixel is then inserted into the path in a way that minimizes the increase in the overall path distance.

Figure 5.4 shows the image \mathbf{I}_a with 1024 pixels from the CIFAR-10 dataset. We investigate the permutation approaches to determine whether minimizing the Hamiltonian path produces a total order that minimizes irregularity. For comparison purposes, we also present the

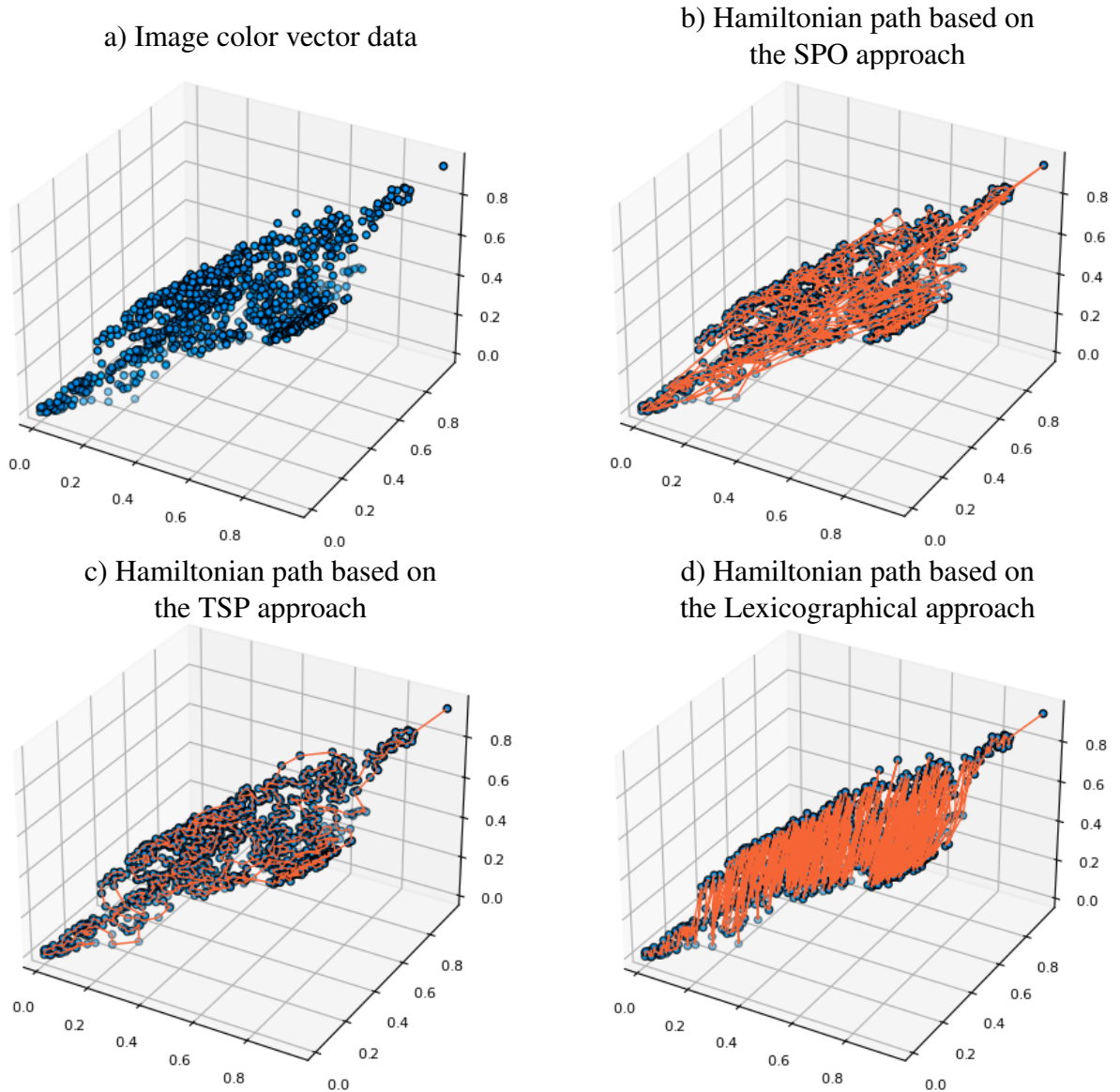


Figure 5.5 – Distribution of the input data obtained by the \mathbf{I}_a , and the respective Hamiltonian paths based on the SPO, TSP, and lexicographic orderings.

result obtained by lexicographical order. The image obtained through the opening operator with the use of the stochastic permutation order (SPO) has an irregularity $\phi_1^g(\mathbf{I}_a, \mathbf{J}_a^{SPO}) = 52.51\%$ and a Hamiltonian path length of 43.28. The order obtained by solving the TSP implies an image \mathbf{J}_a^{TSP} with an irregularity of $\phi_1^g(\mathbf{I}_a, \mathbf{J}_a^{TSP}) = 54.63\%$ and a Hamiltonian path length of 20.05. The irregularity obtained by the image \mathbf{J}_a^L of the lexicographical order is $\phi_1^g(\mathbf{I}_a, \mathbf{J}_a^L) = 8.08\%$ and the Hamiltonian path length is 104.59. Therefore, this example shows that obtaining the shortest path of the Total Variation does not necessarily imply minimizing irregularity. Note that the shortest path is that of the TSP order, however, it yielded the image with the greatest irregularity. The length of the Hamiltonian path of the lexicographical order is greater than those of the SPO and TSP orders, however, it is noticeable that the irregularity of the image obtained by the lexicographical order is lower than the others.

Figure 5.5 shows the Hamiltonian paths of each morphological approach used in the example of Figure 5.4. Figure 5.5a) displays the 1024 values of the colored image in the RGB cube, represented in blue scatter. Figure 5.5b) shows the Hamiltonian path based on the stochastic permutation ordering. It can be observed that the Hamiltonian path obtained by SPO resembles an optimal path. Figure 5.5c) shows the Hamiltonian path based on the TSP ordering. Finally, note that every total order \leq determines a permutation P on the elements of $T = [v_1, \dots, v_n]$, which provides a Hamiltonian path. In the case of the lexicographical ordering, the Hamiltonian path is represented in Figure 5.5d). It can be seen that in this case, the path follows the priority order of the red, green, and then blue components. Also, note that although the TSP ordering path is smaller than the lexicographical ordering path, the irregularity between \mathbf{I}_a and \mathbf{J}_a^{TSP} is greater than the irregularity between \mathbf{I}_a and \mathbf{J}_a^L .

Realizing the difficulty of obtaining a total order to minimize the irregularity, some total orders with optimization techniques can be proposed. For instance, genetic algorithms are a type of optimization technique that draws inspiration from natural evolution and can be used to solve complex optimization problems such as the TSP (Fraser, 1957; Holland, 1975; Brady, 1985). In a genetic algorithm, a population of potential solutions to a problem is evolved over multiple generations by applying the principles of natural selection. At each generation, the fitness of each individual in the population is evaluated using a fitness function. The fittest individuals are selected to create the next generation, using various genetic operators such as crossover and mutation. Crossover combines the genetic material of two individuals to create a new individual with traits from both parents. Mutation introduces random changes to the genetic material of an individual. Through the application of these genetic operators, the population is gradually evolved towards better and better solutions to the problem. This process continues for a predetermined number of generations, or until a satisfactory solution is found (Hassoun, 1995; Koza, 1992).

For our purpose, each individual in the population is a permutation order P , and our evaluation is based on the irregularity that this path provides. At the end of the generations, the algorithm can provide an individual P' that minimizes the irregularity. However, this genetic algorithm is computationally intensive, since it requires a large number of fitness evaluations that are computed by the irregularity index. Additionally, the proper selection of the crossover operation can be quite complicated by the large amount of the color values that are given in an image.

In the same way that genetic algorithms (GA) came from a biological inspiration, artificial neural networks (ANNs) also have their roots in biology. Like the human brain, an artificial neural network is composed of layers of nodes, called neurons, that connect to each other to process information (Rumelhart *et al.*, 1988; Ritter *et al.*, 1992). One important example of neural networks is Kohonen's self-organizing maps, also known as SOM, which can be used to visualize and classify high-dimensional data (Kohonen, 1982). This approach is discussed in

the next section because nowadays the neural networks for multivariate data represent an active research topic and this technique adapts the image value data to obtain a total order.

5.2 Self-Organizing Maps Approach

We present a morphological approach involving a type of artificial neural network known as Kohonen's self-organizing maps (SOM). An artificial neural network is a computational model inspired by a central nervous system, such as the human brain. This model is capable of performing pattern recognition and machine learning. It can be said that artificial neural networks are usually presented as systems of interconnected neurons, which can compute input data, simulating the behavior of biological neural networks. Neural networks have neurons and synaptic weights between neurons that are used to acquire and store knowledge. The knowledge is acquired by the network through a learning process. The procedure used to carry out the learning process is called a learning algorithm. The algorithm modifies the synaptic weights of the network in order to achieve a desired goal (Ritter *et al.*, 1992).

Figure 5.6 shows a simplified artificial neural network composed of interconnected neurons. The circles are neurons. Each neuron is characterized by its synaptic weights, bias, and the activation function. The first layer in a network is called the input layer, while the last one is called the output layer. All layers between the input layer and output layer are referred to as hidden layers. Information moves from the input layer to the hidden layers. The hidden layers do the processing and send the output to the next layer until the output layer.

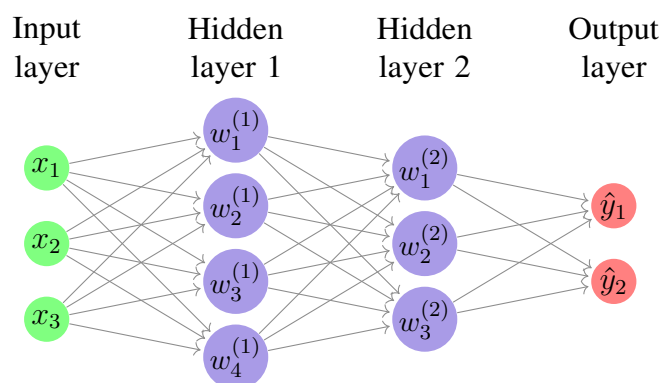


Figure 5.6 – Neural network diagram.

There are several architectures of artificial neural networks that are used to solve different types of problems. One of the first architectures used was the feedforward neural network with the use of the perceptron, originally proposed by Rosenblatt (1958), and later enhanced and studied by Minsky & Papert (1969). After that, the use of other types of neural networks such as recurrent neural networks, associative memory, and self-organizing networks have been proposed (Ritter *et al.*, 1992). For example, Kohonen (1982) proposed an unsupervised learning neural network. The algorithm is known as Kohonen's self-organizing map (SOM).

There are several modern architectures of artificial neural networks that have emerged since Kohonen's self-organizing map. One of the prominent architectures is the Convolutional Neural Network (CNN). CNNs are widely used for image recognition tasks due to their ability to automatically learn hierarchical features from raw pixel data. Introduced by [LeCun *et al.* \(1998\)](#), CNNs have revolutionized computer vision and have been instrumental in achieving state-of-the-art performance in various image-related applications.

Another significant development in neural network architectures is the Recurrent Neural Network (RNN). Unlike feedforward networks, RNNs have feedback connections that enable them to process sequential data, making them suitable for tasks like natural language processing, speech recognition, and time series analysis. One of the key breakthroughs in RNNs was the Long Short-Term Memory (LSTM) architecture, proposed by [Hochreiter & Schmidhuber \(1997\)](#). LSTMs address the vanishing gradient problem, allowing RNNs to retain and process long-range dependencies more effectively.

In recent years, Generative Adversarial Networks (GANs) have gained tremendous attention in the field of deep learning. Introduced by [Goodfellow *et al.* \(2014\)](#), GANs consist of two neural networks: a generator and a discriminator. The generator generates data samples, while the discriminator evaluates their authenticity. This adversarial setup enables GANs to generate realistic data, making them invaluable in tasks like image synthesis, data augmentation, and style transfer.

Additionally, Transformers have emerged as a groundbreaking architecture for natural language processing tasks. Proposed by [Vaswani *et al.* \(2017\)](#), Transformers have largely replaced traditional RNNs in tasks like machine translation, language modeling, and text generation. Their attention mechanism allows them to process input sequences in parallel, resulting in more efficient and scalable models for handling sequential data.

These are just a few examples of modern neural network architectures that have significantly advanced the capabilities of artificial intelligence. The continuous evolution and exploration of novel architectures continue to drive breakthroughs in various domains, making neural networks an indispensable tool in the age of information technology.

Among the neural network architectures, the Kohonen's self-organizing map (SOM) algorithm stands out as a remarkable approach to unsupervised learning. Guided by a series of distinct phases, SOM fosters competition, cooperation, and convergence among neurons to efficiently map input data onto a topologically organized space, enabling powerful data analysis and pattern recognition capabilities. In other words, first, we have a competition between the neurons in response to a given stimulus, with a discriminant function used to determine the winner. Moreover, we have a form of cooperation, in which the winning neuron stimulates the activity of its neighbors, with the spatial proximity of these neurons predetermined. Finally, we have the convergence phase which is the adjustment of the synaptic weights of the activated neurons.

The arrangement of neurons in a uni-dimensional or bi-dimensional network is indicative of the intrinsic statistical characteristics contained in the input patterns. Each neuron has a set of neighboring neurons, allowing the Kohonen network to perform a non-linear transformation that maps input patterns of arbitrary dimensions onto a discrete uni-dimensional or bi-dimensional map. This map forms through an adaptive process and is organized in a topologically ordered manner (Kohonen, 1982, 1990).

Consider an image $\mathbf{I} : D \rightarrow \mathbb{V} \subset \mathbb{R}^d$ and $T = [\mathbf{v}_1, \mathbf{v}_2, \dots, \mathbf{v}_n]$ as the list of values of the image \mathbf{I} . In the Kohonen network algorithm, we denote the input value vector for each instant t as

$$\mathbf{x}_i(t) = [x_{i1}(t), x_{i2}(t), \dots, x_{id}(t)]^t, \quad \text{for all } t = 0, 1, 2, \dots, t_{\max}, \quad (5.5)$$

where t_{\max} is the maximum number of learning steps.

Consider $W = [\mathbf{w}_1, \mathbf{w}_2, \dots, \mathbf{w}_m] \in \mathbb{R}^{d \times m}$ be the list of synaptic weights, where $m \leq \text{Card}\{T\}$. The weight vector of the k -th neuron in the network at instant t is denoted by

$$\mathbf{w}_k(t) = [w_{k1}(t), w_{k2}(t), \dots, w_{kd}(t)]^t. \quad (5.6)$$

Let $\mathbf{w}_k(0) = \mathbf{w}_k$, for all $k \in \{1, 2, \dots, m\}$ and update the vectors $\mathbf{w}_k(t)$ for each natural number t as follows:

First, randomly choose a value \mathbf{v}_i in T and find the best-matching or winning neuron for the input vector \mathbf{v}_i given by

$$j = j(\mathbf{v}_i) = \arg \min_{k=1:m} \|\mathbf{v}_i - \mathbf{w}_k\|. \quad (5.7)$$

Then, we adjust the synaptic weight vectors by the equation

$$\mathbf{w}_k(t+1) = \mathbf{w}_k(t) + \rho(t) \Phi_{k,j}(t) (\mathbf{v}_i - \mathbf{w}_k(t)), \quad t = 0, 1, 2, \dots, t_{\max}, \quad (5.8)$$

where ρ is a learning-rate parameter and $\Phi_{k,j}$ is a neighborhood function around the winning neuron j (Kohonen, 1982; Ritter *et al.*, 1992).

In (5.8), the learning-rate ρ is time varying. It should start at some initial value ρ_0 and then decrease gradually with increasing time t . One possibility is to define ρ as

$$\rho(t) = \rho_0 \left(\frac{\rho_f}{\rho_0} \right)^{\frac{t}{t_{\max}}}, \quad (5.9)$$

where ρ_f is the final value of the learning-rate, and t_{\max} is the maximum number of learning steps.

It is important to note that the neighborhood function $\Phi_{k,j}$ has to be a unimodal non-negative function depending only on the distance between the winning neuron j and the excited

neuron k , for all $k = 1, \dots, m$, where its highest value is at the point $j = k$ and approaching zero for large distances between j and k . One of the appropriate choices we can use is given by the Gaussian function

$$\Phi_{j,k}(t) = \exp\left(-\frac{|j-k|^2}{2\sigma^2(t)}\right), \quad (5.10)$$

where the variance σ^2 controls the width of the neighborhood. The variance is updated with learning step t by means of the equation

$$\sigma(t) = \sigma_0 \left(\frac{\sigma_f}{\sigma_0}\right)^{\frac{t}{t_{\max}}}, \quad (5.11)$$

where σ_0 is the initial value that starts with a rather large value, σ_f is the final value, and t_{\max} is the maximum number of learning steps.

At the end of the update, we obtain a set of synaptic vectors $W = \{\mathbf{w}_1, \mathbf{w}_2, \dots, \mathbf{w}_m\}$ that approximate the input vectors of the image list $T = [\mathbf{v}_1, \mathbf{v}_2, \dots, \mathbf{v}_n]$. With the set W , we can create a h -order h_{SOM} of the set T . For each value \mathbf{v}_i in the list T , the nearest neuron \mathbf{w}_j can be found using the metric d between \mathbf{v}_i and \mathbf{w}_j , and the input points can be sorted according to the order of the nearest neurons \mathbf{w}_j . Thus, we obtain the following definition:

Definition 5.3 (Self-organizing map function). Let $\mathbf{I} : D \rightarrow \mathbb{V} \subset \mathbb{R}^d$ be a multivariate image, let $T = [\mathbf{v}_1, \mathbf{v}_2, \dots, \mathbf{v}_n] \in \mathbb{R}^{d \times n}$ be the matrix values of the image \mathbf{I} , and let $W = [\mathbf{w}_1, \dots, \mathbf{w}_m] \in \mathbb{R}^{d \times m}$ be the matrix of synaptic weight vectors obtained after the training phase in t steps of the SOM algorithm. The self-organizing map function $h_{SOM} : V(\mathbf{I}) \rightarrow I_m$ is defined by

$$h_{SOM}(\mathbf{v}_i) = \arg \min_{j=1:m} \|\mathbf{v}_i - \mathbf{w}_j\|. \quad (5.12)$$

Finally, the self-organizing maps morphological approach is defined by ranking the vector-values according to the h -ordering $h_{SOM} : \mathbb{V} \subset \mathbb{R}^d \rightarrow I_m \subset \mathbb{R}$ given by (5.12) together with a lookup table.

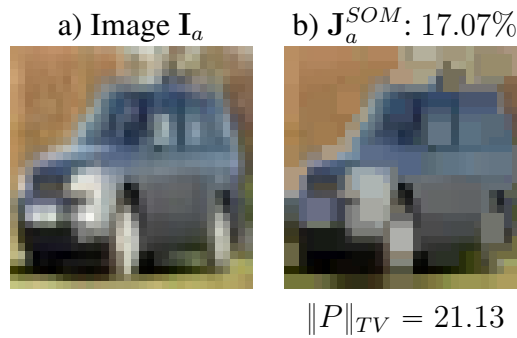


Figure 5.7 – Image \mathbf{I}_a and the opening \mathbf{J}_a^{SOM} .

The application of the self-organizing map function from Definition 5.3 to image \mathbf{I}_a depicted in Figure 5.4, resulted the opened image \mathbf{J}_a^{SOM} showed in Figure 5.7 with an irregularity value of 17.07%, which is smaller than that obtained by the \mathbf{J}_a^{TSP} and it is greater than the value

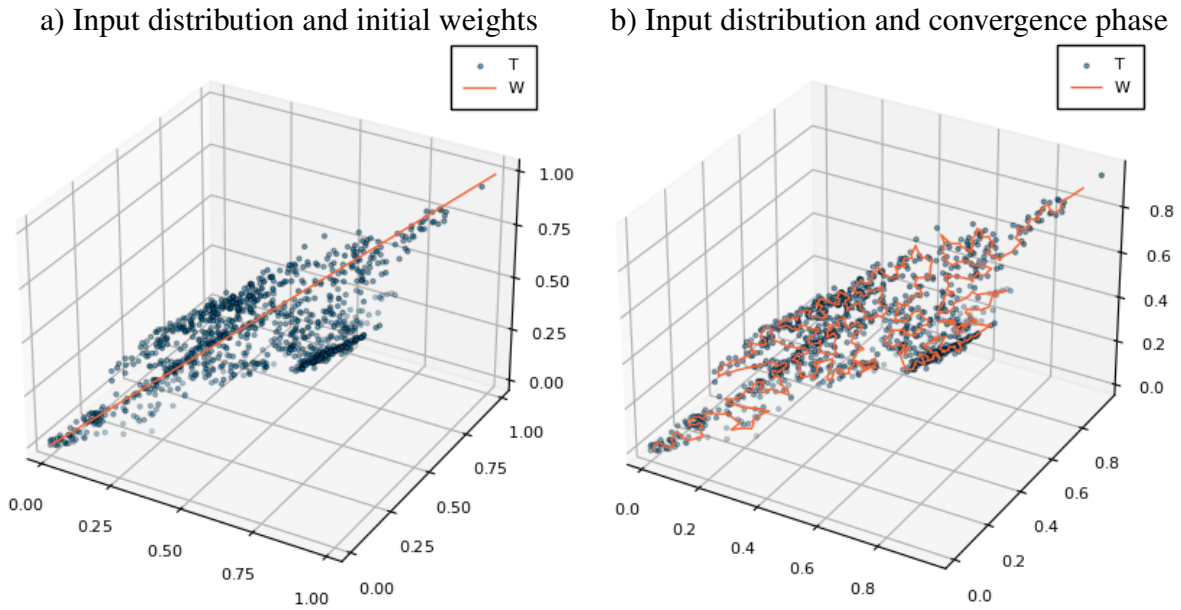
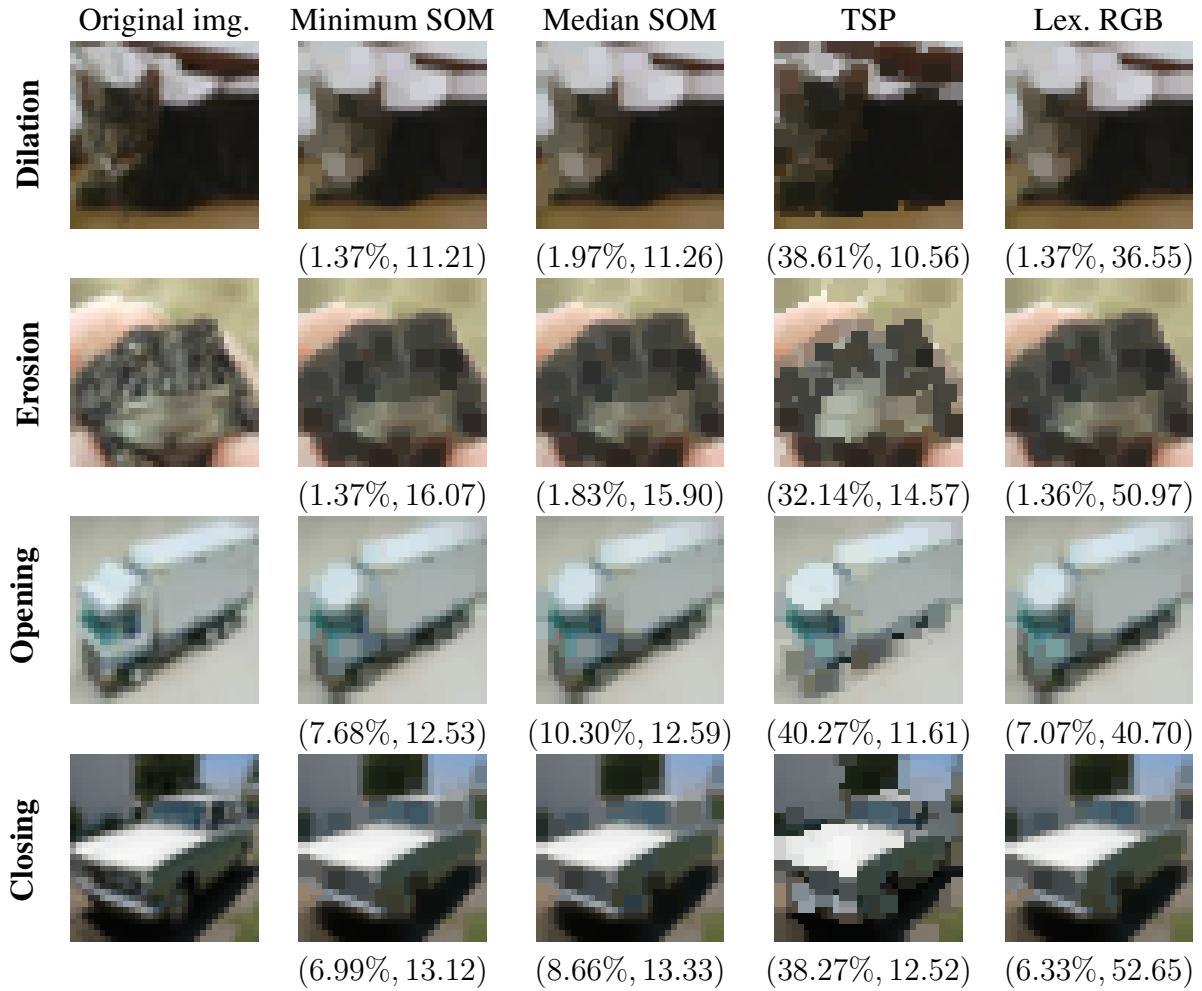


Figure 5.8 – Distribution of the input data obtained by \mathbf{I}_a , initial weights, and the condition of the neurons at the end of the learning phase.

obtained by the \mathbf{J}_a^L . In the SOM algorithm, we initialized a network with 1000 neurons, equally spaced along the diagonal of the cube \mathcal{C}_{RGB} with endpoints at $(0, 0, 0)$ and $(1, 1, 1)$. The network is trained with the three-dimensional input data obtained by the image \mathbf{I}_a .

Figure 5.8 illustrates in blue the distribution of color data from image \mathbf{I}_a and in orange the initial (a) and final (b) synaptic weights. It starts with an input distribution of $T = [v_1, v_2, \dots, v_{1024}]$ values used to train the feature map, and the initial values of the synaptic weights chosen equally spaced along the diagonal of the cube. The other stage shows the convergence phase of the SOM algorithm at the end of the last 10^5 iteration. The curve obtained by ordering of neurons resembles a Peano curve (Kohonen, 1990). These figures show the learning process of the SOM algorithm in which the set of neurons W is adapted in order to fill the color space \mathcal{C}_{RGB} as densely as possible providing a reasonably good approximation to the underlying topology of the three-dimensional input T . After the 100,000-th iteration, we observe that the statistical distribution of the neurons in the map approaches that of the input data. Like the results with the TSP algorithm, the total order obtained by the SOM algorithm did not minimize the irregularity. Moreover, it is observed that the sum of the Total Variation of the path obtained from the SOM approach is 21.13, which is very close to the value of 20.05 obtained by the TSP approach. These close values are consistent with the visual perception in the images of Figure 5.5c) and 5.8b).

In conclusion, obtaining an order via permutation that has a smoothing path to the spectral data of the image does not imply the minimization of the irregularity. In particular, we finish this chapter with Section 5.3 showing the results of some computational experiments of the TSP and SOM morphological approaches to show that in fact there is a difficulty in obtaining

Figure 5.9 – Global irregularity measure Φ_1^g of the TSP and SOM approaches.

a total order that minimizes the irregularity.

5.3 Simulations of the TSP and SOM Morphological Approaches

For the computer simulation, we used the first 100 images from the CIFAR-10 dataset. For comparison purposes, we calculated the global irregularity index and sum of the total variation distance of the Hamiltonian path between images obtained by the morphological approaches based on TSP, SOM, and lexicographical approaches. The SOM morphological approach obtains different results due to the stochastic nature of the SOM algorithm. Thus, for the 100 images of the CIFAR-10 dataset, we applied the SOM morphological approach 51 times for each image. An odd number of times were considered in order to ensure that the median of the global irregularity index corresponds to an image for visual purposes. Figure 5.9 depicts the result of these experiments in which we showed the image that provided the minimum and the median global irregularity index, respectively. We present the results of the irregularity and the sum of the Hamiltonian path in the form $(\Phi_1^g(\mathbf{I}, \mathbf{J}), \|P\|_{TV})$. We used the same images in Figure

3.3 for comparison with the other approaches which were used in this work.

In Figure 5.9, we show in the first line the dilated images of the SOM, TSP, and lexicographical approach. The minimum global irregularity index of the 51 images generated by the SOM algorithm is 1.37% coinciding with the global irregularity index of the lexicographical order. The median of the global irregularity index is 1.97%. In the second line we show the eroded images. The minimum value of the global irregularity index is 1.37% that is very close to the global irregularity index of the lexicographical order. The median of the global irregularity index is 1.83%. The results in the images obtained by opening are very similar to those obtained by erosion. We have the values 7.68% and 10.30% to the minimum and the median global irregularity values. In the first line we present the images obtained by the closing operator. The minimum global irregularity index is 6.99% and the median is 8.66%. The global irregularity values of the images obtained by the TSP order are the highest, corresponding to 38.61%, 32.14%, 40.27%, and 38.27%, for dilation, erosion, opening, and closing, respectively. It is worth noting that while the TSP approach exhibits higher irregularity values compared to the SOM and lexicographical approaches, it achieves the lowest possible sum of the Total Variation of Hamiltonian paths. Conversely, the lexicographical images show lower irregularity values, but their sum of Total Variation of Hamiltonian paths is higher than that of TSP and SOM approaches.

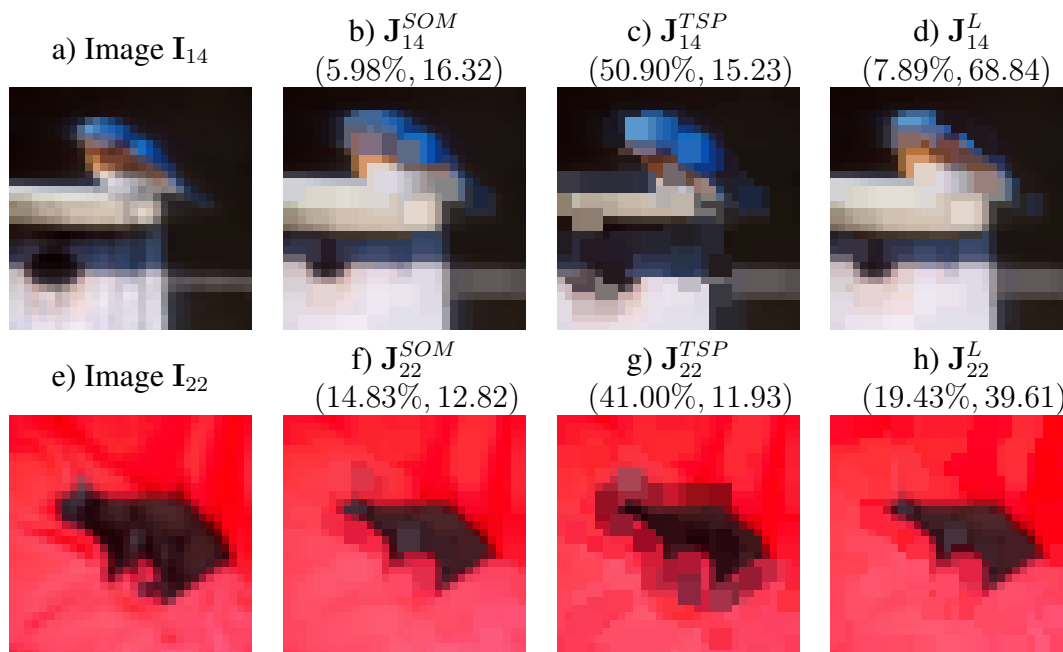


Figure 5.10 – Images I_{14} , I_{22} , and their dilations by SOM, TSP, and lexicographical approaches.

It is natural to question whether the lexicographical order always provides a lower irregularity. It turns out that the answer is negative. For instance, Figure 5.10 shows the images I_{14} and I_{22} along with their dilations using the SOM, TSP, and lexicographical approaches. It is worth noting that the images obtained by the TSP order had the shortest Hamiltonian path and the highest irregularity. However, the irregularities of the images obtained by the morphological

SOM approach are lower than those of the lexicographical images. Moreover, the length of Hamiltonian paths of the images obtained by SOM is lower than the length of Hamiltonian paths of the lexicographical order. Therefore, the irregularity depends on the total order used as well as the color spectrum of the image, which implies the difficulty of obtaining a total order that minimizes the irregularity.

Conclusions

This chapter offers a brief examination of the problem statement and research objective that guided this thesis, and presents the conclusions drawn from the research results reported in Chapters 3, 4, and 5, including discussions and recommendations for future research.

When we apply morphological operators to multivariate images using a total order, the images obtained by such operators can contain irregularities (Chevallier & Angulo, 2016). Thus, our research objective is to propose an irregularity measure for multivariate mathematical morphology. In particular, our irregularity measure must provide a percentage of how much an output multivariate image J obtained by a morphological operator has irregularity based on its input multivariate image I .

Therefore, in this thesis, we have introduced the global irregularity measure via the Wasserstein metric and verified through computational experiments for tiny color images that our measure provides an irregularity measure for multivariate mathematical morphology. Additionally, by using a partition of the input image domain that is a family of sets W_ℓ which we called simply by windows, and considering the Wasserstein metric restricted to each window W_ℓ , we have introduced the local irregularity index that can be used, for example, to evaluate the irregularity in natural color images. Our computational experiments with tiny color images have shown that there is a correlation between the local and global irregularity indices.

Furthermore, we have verified that the local irregularity index is a lower bound of the global irregularity measure. We have also observed in general that the irregularity index of the marginal and Loewner approaches are smaller than the total order approaches, further affirming our developed theory. Moreover, we have observed from computational experiments that the entropic regularized method using the stabilized Sinkhorn algorithm is indeed much more efficient in running time compared to the analytic solution of the Wasserstein metric, and the stabilized Sinkhorn method is a very good approximation to the irregularity measure obtained by the Wasserstein metric.

Additionally, we have investigated the relationship between the size of the structuring element and the local irregularity measure in natural color images. The results indicate that the local irregularity measure decreases with an increase in the size of the structuring element. In addition, we also have investigated the correlation between the size of the local window W_ℓ and the local irregularity measure and we have found that an increase in the local window W_ℓ leads to an increase in the irregularity index.

Lastly, we have examined the challenge of obtaining a total order that minimizes the irregularity issue. We discussed new multivariate morphological approaches based on stochastic permutation ordering (SPO), the traveling salesman problem (TSP), and Kohonen's self-

organizing maps (SOM). The approaches studied to demonstrate that the minimization of the Hamiltonian path does not necessarily imply the minimization of irregularity.

The results of this research have provided a new understanding of the field of mathematical morphology by introducing a new irregularity measure for multivariate mathematical morphology. This measure of irregularity is obtained through the Wasserstein metric, which requires the resolution of a linear programming problem. Furthermore, as outlined in [Valle *et al.* \(2021, 2022\)](#), our research was the pioneering work to propose the use of the Wasserstein metric to determine an irregularity measure in an output multivariate image obtained by a morphological operator, based on its input multivariate image. This highlights that our research also provides the perspective that the study of other areas of mathematics such as optimal transport, linear programming, and optimization problems can help us solve some problems in mathematical morphology, as these areas provide tools and techniques for dealing with resource allocation and decision-making problems, which are similar to some issues faced in mathematical morphology.

Future studies could expand on the work presented here by investigating new methods for multivariate morphological processing. This could include experimenting with the application of neural networks to morphological image processing, and comparing results with those obtained using the Wasserstein metric framework developed in this thesis. Another possibility would be to investigate a morphological approach to multivariate images based on genetic algorithms. In this situation, one can explore the potential of this optimization method to find a total order that minimizes the irregularity. Another potential area for study would be to explore ways to create an image \mathbf{J}^* with the same number of values as a multivariate morphological image \mathbf{J} obtained from an input image \mathbf{I} , such that when the global irregularity measure Φ_p^g is applied, it holds that $\Phi_p^g(\mathbf{I}, \mathbf{J}^*) \leq \Phi_p^g(\mathbf{I}, \mathbf{J})$. Finally, we could explore the possibility of a new local irregularity measure Ψ_p^l for the irregularity issue by examining alternative ways of partitioning the input image \mathbf{I} into windows W_k , beyond the approach used in this study. One possibility could be to use image segmentation methods to partition the domain of the input image \mathbf{I} into different color regions and examine the effects on the measure of irregularity and compare with the results obtained in this thesis.

Bibliography

- Adrabiński, Andrzej, & Syslo, Maciej M. 1983. Computational experiments with some approximation algorithms for the travelling salesman problem. *Applicationes Mathematicae*, **18**, 91–95.
- Ambrosio, L. 2003. *Optimal Transport Problems*. Berlin: Springer.
- Angulo, Jesús, & Serra, Jean Paul Frédéric. 2003. Mathematical Morphology in Color Spaces applied to the Analysis of Cartographic Images.
- Angulo, Jesús. 2007. Morphological colour operators in totally ordered lattices based on distances: Application to image filtering, enhancement and analysis. *Computer Vision and Image Understanding*, **107**(1–2), 56–73.
- Applegate, David L., Chvatal, Vasek, Bixby, Robert E., & Cook, William J. 2011. *The Traveling Salesman Problem: a Computational Study*. Princeton: Princeton University Press.
- Aptoula, Erchan, & Lefèvre, Sébastien. 2007. A Comparative Study on Multivariate Mathematical Morphology. *Pattern Recognition*, **40**(11), 2914–2929.
- Aptoula, Erchan, & Lefèvre, Sébastien. 2008. On Lexicographical Ordering in Multivariate Mathematical Morphology. *Pattern Recognition Letters*, **29**(2), 109–118.
- Atif, Jamal, Bloch, Isabelle, Distel, Felix, & Hudelot, Céline. 2013. Mathematical Morphology Operators over Concept Lattices. *Pages 28–43 of: Cellier, Peggy, Distel, Felix, & Ganter, Bernhard (eds), Proceedings of the 11th International Conference on Formal Concept Analysis (ICFCA'13)*. Lecture Notes in Computer Science, vol. 7880. Springer-Verlag.
- Backes, André Ricardo, Casanova, Dalcimar, & Bruno, Odemir Martinez. 2009. Plant leaf identification based on volumetric fractal dimension. *International Journal of Pattern Recognition and Artificial Intelligence*, **23**(6), 1145–1160.
- Banon, G J F, & Barrera, J. 1993. Decomposition of Mappings between Complete Lattices by Mathematical Morphology, Part 1. General Lattices. *Signal Processing*, **30**(3), 299–327.
- Barnett, V. 1976. The ordering of multivariate data. *Journal of Royal Statistical Society A*, **3**, 318–355.
- Bazaraa, Mokhtar S, Sherali, Hanif D, & Shetty, C M. 2006. *Nonlinear Programming: Theory and Algorithms*. 3 edn. Wiley-Interscience.
- Bertsekas, D P. 1995. *Nonlinear Programming*. Belmont, MA: Athena Scientific.

- Birkhoff, G. 1993. *Lattice Theory*. 3 edn. Providence: American Mathematical Society.
- Bondy, A., & Murty, U. S. R. 2008. *Graph Theory*. 3 edn. New York: Springer.
- Brady, R. M. 1985. Optimization strategies gleaned from biological evolution. *Nature*, **317**, 804–806.
- Braga-Neto, U., & Goutsias, J. 2004. Supremal multiscale signal analysis. *SIAM Journal of Mathematical Analysis*, **36**(1), 94–120.
- Bruno, Odemir Martinez, Plotze, Rodrigo de Oliveira, & Falvo, Mauricio. 2008. Fractal dimension applied to plant identification. *Information Sciences*, **178**(12), 2722–2733.
- Burgeth, Bernhard, & Kleefeld, Andreas. 2013. Morphology for Color Images via Loewner Order for Matrix Fields. *Pages 243–254 of: In: Hendriks, C.L.L., Borgefors, G., Strand, R. (eds) Mathematical Morphology and Its Applications to Signal and Image Processing. ISMM 2013. Lecture Notes in Computer Science*, vol. 7883. Heidelberg: Springer, Berlin, Heidelberg.
- Burgeth, Bernhard, & Kleefeld, Andreas. 2014. An approach to color-morphology based on Einstein addition and Loewner order. *Pattern Recognition Letters*, **47**(0), 29–39.
- Burgeth, Bernhard, Didas, Stephan, & Kleefeld, Andreas. 2019. A Unified Approach to the Processing of Hyperspectral Images. *Pages 202–214 of: Burgeth, Bernhard, Kleefeld, Andreas, Naegel, Benoît, Passat, Nicolas, & Perret, Benjamin (eds), Mathematical Morphology and Its Applications to Signal and Image Processing*. Cham: Springer International Publishing.
- Chevallier, Emmanuel, & Angulo, Jesús. 2016. The Irregularity Issue of Total Orders on Metric Spaces and Its Consequences for Mathematical Morphology. *Journal of Mathematical Imaging and Vision*, **54**(3), 344–357.
- Christofides, Nicos. 1976. Worst-case Analysis of a New Heuristic for the Travelling Salesman Problem. *Graduate School of Industrial Administration, CMU*, **10**(388), 1–10.
- Cominetti, R., & Martín, J. S. 1994. Asymptotic analysis of the exponential penalty trajectory in linear programming. *Mathematical Programming*, **67**, 169–187.
- Cristianini, N., & Shawe-Taylor, J. 2000. *An Introduction to Support Vector Machines and Other Kernel Based Learning Methods*. Cambridge, U.K.: Cambridge Univ. Press.
- Cuturi, Marco. 2013. Sinkhorn Distances: Lightspeed Computation of Optimal Transport. *Advances in Neural Information Processing Systems*, **26**, 2292–2300.
- Davey, B. A., & Priestley, H. A. 2002. *Introduction to Lattices and Order*. 2 edn. New York: Cambridge University Press.

- Donoho, D., & Gasko, M. 1992. Breakdown properties of location estimates based on halfspace depth and projected outlyingness. *Ann. Statist.*, **20**(4), 1803 – 1827.
- Figalli, Alessio. 2021. *General optimal transport theory*. <https://people.math.ethz.ch/~afigalli/General-optimal-transport-theory>.
- Fletcher, R. 1987. *Practical Methods of Optimization*. 2 edn. John Wiley.
- Florindo, João B., Sikora, Mariana S., Pereira, Ernesto C., & Bruno, Odemir M. 2013. Characterization of nanostructured material images using fractal descriptors. *Physica A: Statistical Mechanics and its Applications*, **392**(7), 1694–1701.
- Florindo, João B., Assirati, Lucas., & Bruno, Odemir Martinez. 2016. Locally enhancing fractal descriptors by using the non-additive entropy. *Pattern Recognition Letters*, **70**, 32–37.
- Florindo, João Batista, & Metze, Konradin. 2021. Using Non-Additive Entropy to Enhance Convolutional Neural Features for Texture Recognition. *Entropy*, **23**(7).
- Fraser, A. S. 1957. Simulation of Genetic Systems by Automatic Digital Computers. *Australian Journal of Biological Sciences*, **10**(4), 484–491.
- Gierz, Gerhard, Hofmann, Karl Heinrich, Keimel, Klaus, Lawson, Jimmie D., Mislove, Michael W., & Scott, Dana S. 1980. *A Compendium of Continuous Lattices*. 1 edn. Berlin: Springer-Verlag.
- Golden, Bruce, Bodin, Lawrence, Doyle, T, & Stewart Jr, W. 1980. Approximate traveling salesman algorithms. *Operations research*, **28**(3-part-ii), 694–711.
- González-Hidalgo, Manuel, Massanet, Sebastia, Mir, Arnau, & Ruiz-Aguilera, Daniel. 2015. On the choice of the pair conjunction–implication into the fuzzy morphological edge detector. *IEEE Transactions on Fuzzy Systems*, **23**(4), 872–884.
- Goodfellow, Ian, Pouget-Abadie, Jean, Mirza, Mehdi, Xu, Bing, Warde-Farley, David, Ozair, Sherjil, Courville, Aaron, & Bengio, Yoshua. 2014. Generative Adversarial Nets. *Pages 2672–2680 of: Advances in Neural Information Processing Systems*.
- Goutsias, John, Heijmans, Henk J A M, & Sivakumar, K. 1995. Morphological Operators for Image Sequences. *Computer vision and image understanding*, **62**, 326–346.
- Grätzer, George, & others. 2003. *General Lattice Theory*. 2 edn. Basel, Switzerland: Birkhäuser Verlag.
- Gutin, Gregory, Yeo, Anders, & Zverovich, Alexey. 2002. Traveling salesman should not be greedy: domination analysis of greedy-type heuristics for the TSP. *Discrete Applied Mathematics*, **117**, 81–86.

- Hanbury, Allan, & Serra, Jean. 2001a. Mathematical Morphology in the {HLS} Colour Space. *Pages 451–460 of: Proceedings of the 12th British Machine Vision Conference.*
- Hanbury, Allan, & Serra, Jean. 2001b. *Mathematical Morphology in the {L}*a*b* Colour Space.* Tech. rept. Centre de Morphologie Mathématique, École des Mines de Paris.
- Haralick, Robert M., Shanmugam, K., & Dinstein, Its'Hak. 1973. Textural Features for Image Classification. *IEEE Transactions on Systems, Man, and Cybernetics*, **3**(6), 610–621.
- Hardie, R. C., & Arce, G. R. 1991. Ranking in R_p and its use in multivariate image estimation. *IEEE Transactions Circuits Syst. Video Technology*, **1**(2), 197–209.
- Harte, David. 2001. *Multifractals: theory and applications.* CRC Press.
- Hassoun, M H. 1995. *Fundamentals of Artificial Neural Networks.* Cambridge, MA: MIT Press.
- Haykin, Simon. 2009. *Neural Networks and Learning Machines.* 3rd edn. Upper Saddle River, NJ: Prentice-Hall.
- Heijmans, H J A M. 1987. Mathematical Morphology: an algebraic approach. *CWI Newsletter*, **14**, 7–27.
- Heijmans, H J A M, & Ronse, C. 1990. The Algebraic Basis of Mathematical Morphology I. Dilations and Erosions. *Computer Vision, Graphics, and Image Processing*, **50**(3), 245–295.
- Heijmans, H J A M, & Ronse, C. 1991. The Algebraic Basis of Mathematical Morphology II. Openings and Closings. *Computer Vision, Graphics, and Image Processing*, **54**(1), 74–97.
- Heijmans, Henk J A M. 1995. Mathematical Morphology: A Modern Approach in Image Processing Based on Algebra and Geometry. *SIAM Review*, **37**(1), 1–36.
- Heijmans, H.J.A.M. 1991. Theoretical Aspects of Gray-Level Morphology. *IEEE Transactions on Pattern Analysis and Machine Intelligence*, **13**(6), 568–582.
- Heijmans, H.J.A.M. 1994. *Morphological Image Operators.* New York, NY: Academic Press.
- Hochreiter, Sepp, & Schmidhuber, Jürgen. 1997. Long Short-Term Memory. *Neural Computation*, **9**(8), 1735–1780.
- Holland, J. H. 1975. *Adaptation in Natural and Artificial Systems: An Introductory Analysis with Applications to Biology, Control, and Artificial Intelligence.* University of Michigan Press.
- John, Fritz. 1948. Extremum Problems with Inequalities as Subsidiary Conditions. *Studies and Essays: Courant Anniversary*, 187–204.
- Jolliffe, I. T. 2010. *Principal Component Analysis.* 2 edn. New York, USA: Springer-Verlag.

- Kambhatla, N., & Leen, T. 1997. Dimension reduction by local principal component analysis. *Neural Computation*, **9**(7), 1493 – 1516.
- Kantorovich, L. V. 1939. Mathematical Methods of Organizing and Planning Production. *Management Science*, **6**, 366–422.
- Kantorovich, L. V. 1948. On a problem of Monge. *Uspekhi Mat. Nauk.*, **3**, 225–226.
- Kantorovich, L. V., & Rubinstein, G. 1942. On mass transportation. *Dokl. Akad. Nauk.*, **37**, 227–229.
- Kohonen, T. 1982. Self-Organized Formation of Topologically Correct Feature Maps. *Biological Cybernetics*, **43**, 59–69.
- Kohonen, Teuvo. 1990. The Self-Organizing Maps. *Proceedings of the IEEE*, **78**(9), 1464–1480.
- Koza, John R. 1992. *Genetic Programming: On the Programming of Computers by Means of Natural Selection*. MIT Press.
- Krizhevsky, Alex. 2009. *Learning multiple layers of features from tiny images*. Tech. rept. University of Toronto.
- Kuhn, H. W., & Tucker, A. W. 1951. Nonlinear programming. *Pages 481–492 of: Proceedings of the Second Berkeley Symposium on Mathematical Statistics and Probability*. Berkeley and Los Angeles: University of California Press.
- Kuhn, Harold W. 1976. Nonlinear programming: a historical view. *Pages 1–26 of: Nonlinear Programming*. New York: American Mathematical Society.
- LeCun, Yann, Bottou, Léon, Bengio, Yoshua, & Haffner, Patrick. 1998. Gradient-based learning applied to document recognition. *Proceedings of the IEEE*, **86**(11), 2278–2324.
- Lézoray, Olivier. 2016. Complete lattice learning for multivariate mathematical morphology. *Journal of Visual Communication and Image Representation*, **35**, 220–235.
- Lézoray, Olivier. 2021. Mathematical morphology based on stochastic permutation orderings. *Mathematical Morphology - Theory and Applications*, **5**(1), 43–69.
- Liao, S., Fan, W., Chung, A.C., & Yeung, D.Y. 2006. Facial Expression Recognition using Advanced Local Binary Patterns, Tsallis Entropies and Global Appearance Features. *Pages 665–668 of: Proceedings of the 2006 International Conference on Image Processing*.
- Lin, S., & Kernighan, B. W. 1973. An Effective Heuristic Algorithm for the Traveling-Salesman Problem. *Operations Research*, **21**(2), 498–516.
- Luenberger, David G. 1984. *Linear and Nonlinear Programming*. 2 edn. Addison-Wesley.

- Lézoray, Olivier. 2017. Stochastic spectral-spatial permutation ordering combination for nonlocal morphological processing. *Pages 1–5 of: 2017 International Conference on Systems, Signals and Image Processing (IWSSIP)*.
- Lézoray, Olivier, Charrier, Christophe, & Elmoataz, Abderrahim. 2009. Learning complete lattices for manifold mathematical morphology. *Pages 1–4 of: Wilkinson, M, & Roerdink, J (eds), 9th International Symposium on Mathematical Morphology (ISMM 2009)*. The Netherlands: University of Groningen.
- Manoel, E. T. M., Costa, L. D. F., Streicher, J., & Muller, G.B. 2002. Multiscale fractal characterization of three-dimensional gene expression data. *Pages 269–274 of: Brazilian Symposium of Computer Graphic and Image Processing*, vol. 2002.
- Martin, D, Fowlkes, C, Tal, D, & Malik, J. 2001. A Database of Human Segmented Natural Images and its Application to Evaluating Segmentation Algorithms and Measuring Ecological Statistics. *Pages 416–423 of: Proceedings of the 8th International Conference on Computer Vision*, vol. 2.
- Matheron, G. 1975. *Random Sets and Integral Geometry*. New York, NY: John Wiley & Sons.
- Menger, Karl. 1927. Zur allgemeinen Kurventheorie. *Fundamenta Mathematicae*, **10**, 96–115.
- Minsky, M L, & Papert, S A. 1969. *Perceptrons: An Introduction to Computational Geometry*. Cambridge, MA: MIT Press.
- Monge, G. 1781. Mémoire sur la théorie des déblais et des remblais. *Histoire de l'Académie Royale de Sciences de Paris*, 666–704.
- Müller, Klaus-Robert, Mika, Sebastian, Rätsch, Gunnar, Tsuda, Koji, & Schölkopf, Bernhard. 2001. An Introduction to Kernel-Based Learning Algorithms. *IEEE Transactions on Neural Networks*, **12**, 181–201.
- Najman, Laurent, & Talbot, Hugues (eds). 2013. *Mathematical Morphology: From Theory to Applications*. Hoboken, NJ, USA: John Wiley & Sons, Inc.
- Nash, S. G., & Sofer, A. 1996. *Linear and Nonlinear Programming*. McGraw-Hill.
- Nemirovski, Arkadi, & Rothblum, Uriel. 1999. On complexity of matrix scaling. *Linear Algebra and its Applications*, **302–303**, 435–460.
- Nesterov, Y. 2005. Smooth minimization of non-smooth functions. *Mathematical Programming*, **103**, 127–152.
- Ojala, Timo, Pietikainen, Matti, & Maenpaa, Topi. 2002. Multiresolution gray-scale and rotation invariant texture classification with local binary patterns. *IEEE Transactions on pattern analysis and machine intelligence*, **24**(7), 971–987.

- Peyré, Gabriel, & Cuturi, Marco. 2019. Computational optimal transport. *Foundations and Trends in Machine Learning*, **11**(5-6), 1–257.
- Pitié, François. 2020. Advances in colour transfer. *IET Computer Vision*, **14**(6), 304–322.
- Pitié, François, Kokaram, Anil C., & Dahyot, Rozenn. 2005. N-dimensional probability density function transfer and its application to colour transfer. *Pages 1434–1439 of: Proceedings of the IEEE International Conference on Computer Vision*, vol. II.
- Prokhorov, Yu. V. 1956. Convergence of Random Processes and Limit Theorems in Probability Theory. *Theory of Probability and Its Applications*, **1**, 157–214.
- Ritter, Helge, Martinez, Thomas, & Schulten, Klaus. 1992. *Neural Computation and Self-Organizing Maps: An Introduction*. New York: Addison-Wesley.
- Rittner, Leticia, Campbell, Jennifer, Freitas, Pedro, Appenzeller, Simone, Pike, G Bruce, & Lotufo, Roberto. 2013. Analysis of Scalar Maps for the Segmentation of the Corpus Callosum in Diffusion Tensor Fields. *Journal of Mathematical Imaging and Vision*, **45**, 214–226.
- Ronse, C. 1990. Why Mathematical Morphology Needs Complete Lattices. *Signal Processing*, **21**(2), 129–154.
- Rosenblatt, F. 1958. The Perceptron: A Probabilistic Model for Information Storage and Organization in the Brain. *Psychological Review*, **65**, 386–408.
- Rubner, Yossi, Tomasi, Carlo, & Guibas, Leonidas J. 2000. Earth mover's distance as a metric for image retrieval. *International Journal of Computer Vision*, **40**(2), 99–121.
- Rumelhart, D E, Hinton, G E, & Williams, R J. 1988. *Learning Internal Representations by Error Propagation*. Parallel Distributed Processing. Cambridge, MA: MIT Press.
- Santambrogio, F. 2015. *Optimal Transport for Applied Mathematicians*. Switzerland: Springer.
- Schmitzer, Bernhard. 2019. Stabilized sparse scaling algorithms for entropy regularized transport problems. *SIAM Journal on Scientific Computing*, **41**(3), A1443–A1481.
- Schrödinger, Erwin. 1931. Über die Umkehrung der Naturgesetze. *Verlag der Akademie der Wissenschaften*, **12**(3), 3–10.
- Serra, J. 1982. *Image Analysis and Mathematical Morphology*. London: Academic Press.
- Serra, J. 1986. Introduction to Mathematical Morphology. *Computer Vision, Graphics, and Image Processing*, **35**, 283–305.
- Serra, J. 1988. *Image Analysis and Mathematical Morphology, Volume 2: Theoretical Advances*. New York: Academic Press.

- Serra, Jean. 2006. A Lattice Approach to Image Segmentation. *Journal of Mathematical Imaging and Vision*, **24**, 83–130.
- Serra, Jean. 2009. The “False Colour” Problem. *Pages 13–23 of: Wilkinson, Michael H F, & Roerdink, Jos B T M (eds), Mathematical Morphology and Its Application to Signal and Image Processing*. Lecture Notes in Computer Science, vol. 5720. Springer Berlin Heidelberg.
- Sinkhorn, Richard. 1964. A Relationship Between Arbitrary Positive Matrices and Doubly Stochastic Matrices. *The Annals of Mathematical Statistics*, **35**(2), 876–879.
- Sinkhorn, Richard, & Knopp, Paul. 1967. Concerning Nonnegative Matrices and Doubly Stochastic Matrices. *Pacific Journal of Mathematics*, **21**(2), 343–348.
- Soille, P. 1999. *Morphological Image Analysis*. Berlin: Springer Verlag.
- Soille, P, Vogt, J, & Colombo, R. 2003. Carving and adaptive drainage enforcement of grid digital elevation models. *Water Resources Research*, **39**(12), 1366.
- Theodoridis, Sergios, & Koutroumbas, Konstantinos. 2006. *Pattern recognition*. Elsevier.
- Valle, Marcos Eduardo, & Valente, Raul Ambrozio. 2016. Mathematical Morphology on the Spherical CIELab Quantale with an Application in Color Image Boundary Detection. *Journal of Mathematical Imaging and Vision*, 1–19.
- Valle, Marcos Eduardo, Francisco, Samuel, Granero, Marco Aurélio, & Velasco-Forero, Santiago. 2021. Measuring the Irregularity of Vector-Valued Morphological Operators Using Wasserstein Metric. *Pages 512–524 of: In: Lindblad J., Malmberg F., Sladoje N. (eds) Discrete Geometry and Mathematical Morphology. DGMM 2021. Lecture Notes in Computer Science*, vol. 12708. Springer, Cham.
- Valle, Marcos Eduardo, Francisco, Samuel, Granero, Marco Aurélio, & Velasco-Forero, Santiago. 2022. Irregularity Index for Vector-Valued Morphological Operators. *Journal of Mathematical Imaging and Vision, ICML 2013*, **64**(7), 754–770.
- Vapnik, Vladimir N. 1998. *Statistical Learning Theory*. New York, NY, USA: John Wiley and Sons.
- Vapnik, Vladimir N. 1999. *The Nature of Statistical Learning Theory*. 2 edn. Springer.
- Vasershtein, L. N. 1969. Markov Processes on a Countable Product of Spaces Describing Large Systems of Automata. *Probl. transmission of information*, **5**, 47–52.
- Vaswani, Ashish, Shazeer, Noam, Parmar, Niki, Uszkoreit, Jakob, Jones, Llion, Gomez, Aidan N., Kaiser, Łukasz, & Polosukhin, Illia. 2017. Attention is All You Need. *Pages 5998–6008 of: Advances in Neural Information Processing Systems*.

- Veganzones, M. Á., Dalla Mura, M., Tochon, G., & Chanussot, J. 2015. Binary Partition Trees-Based Spectral-Spatial Permutation Ordering. *Pages 434–445 of: In: Benediktsson, J., Chanussot, J., Najman, L., Talbot, H. (eds) Mathematical Morphology and Its Applications to Signal and Image Processing. ISMM 2015. Lecture Notes in Computer Science*, vol. 9082. Springer, Cham.
- Velasco-Forero, S, & Angulo, J. 2011. Supervised Ordering in R_p : Application to Morphological Processing of Hyperspectral Images. *IEEE Transactions on Image Processing*, **20**(11), 3301–3308.
- Velasco-Forero, S, & Angulo, J. 2012. Random Projection Depth for Multivariate Mathematical Morphology. *IEEE Journal of Selected Topics in Signal Processing*, **6**(7), 753–763.
- Velasco-Forero, Santiago, & Angulo, Jesus. 2014. Vector Ordering and Multispectral Morphological Image Processing. *Pages 223–239 of: Celebi, M Emre, & Smolka, Bogdan (eds), Advances in Low-Level Color Image Processing*. Dordrecht: Springer Netherlands.
- Villani, Cédric. 2003. *Topics in Optimal Transportation*. Providence, Rhode Island: American Mathematical Society.
- Villani, Cédric. 2009. *Optimal Transport: Old and New*. Berlin: Springer-Verlag.
- Villani, Cédric. 2021. *Presentation of my research*. <https://cedricvillani.org/for-mathematicians/presentation-of-my-research/>.
- Wang, Z., & Bovik, A. C. 2002. A Universal Image Quality Index. *IEEE Signal Processing Letters*, **9**(3), 81–84.
- Wang, Z, Bovik, A C, Sheikh, H R, & Simoncelli, E P. 2004. Image quality assessment: From error visibility to structural similarity. *IEEE Transactions on Image Processing*, **13**(4), 600–612.
- West, Douglas Brent. 2002. *Introduction to Graph Theory*. 2 edn. Singapore: Pearson Education.
- Wilson, A. G. 1969. The Use of Entropy Maximising Models, in the Theory of Trip Distribution, Mode Split and Route Split. *Journal of Transport Economics and Policy*, **3**(1), 108–126.
- Zuo, Y., & Serfling, R. 2000. General notions of statistical depth function. *Ann. Statist.*, **28**(2), 461 – 482.